Gas-fed Pulsed Plasma Thrusters:
Fundamentals, Characteristics and Scaling Laws

FINAL REPORT

PI: Prof. Edgar Choueiri

Graduate Students: John Ziemer and Thomas Markusic

Electric Propulsion and Plasma Dynamics Lab (EPPDyL)
Applied Physics Group
MAE Dept., Princeton University
Princeton NJ 08544
Phone: (609) 258 5220 Fax: (609) 258 6875
E-mail: choueiri@princeton.edu

In memory of Dr. Daniel Birx who contributed greatly to this work.

20010406 169

REPORT DOCUMENTATION PAGE

AFRL-SR-BL-TR-01-

0235

1. AGENCY USE ONLY (Leave blank)	2. REPORT DATE March 21, 2001	3. REPORT TYPE AND DATES COVERED Final Technical Report, Jan. 1, 1998 to Dec. 31, 2000

4. TITLE AND SUBTITLE

Gas-Fed Pulsed Plasma Thrusters: Fundamentals, Characteristics and Scaling Laws

5.   FUNDING NUMBERS
PE   61102F
PR   2308
SA   AC
GRANT #   F49620-98-1-0119

6.   AUTHOR(S)

Prof. Edgar Choueiri

7. PERFORMING ORGANIZATION NAME(S) AND ADDRESS(ES)

Princeton University
Dept. Mechanical & Aerospace Engrg.
Olden St.
Princeton, NJ 08544

8. PERFORMING ORGANIZATION REPORT NUMBER

9. SPONSORING / MONITORING AGENCY NAME(S) AND ADDRESS(ES)

AFOSR/NA
801 N. Randolph St., Room 732
Arlington, VA 22203-1977

10. SPONSORING / MONITORING AGENCY REPORT NUMBER

11. SUPPLEMENTARY NOTES

12a. DISTRIBUTION / AVAILABILITY STATEMENT

Approved for public release, distribution is unlimited

12b. DISTRIBUTION CODE

13. ABSTRACT (Maximum 200 Words)

This final report presents the results of a three-year theoretical and experimental investigation into the fundamentals of gas-fed pulsed plasma thrusters (GF-PPTs). The primary goals were to deepen the basic understanding of how the performance of these devices can be optimized and scaled down to low pulse energies for application as efficient high-specific electric thrusters on small spacecraft. This final report gives a detailed overview of previous research, discusses the electromagnetic nature of the acceleration process, the effects of capacitance, electrode geometry, inductance-per-unit length, and discharge initiation on performance, and presents theoretically derived and experimentally verified performance scaling laws.

14. SUBJECT TERMS

Gas-fed plasma thrusters, capacitance, electrode geometry, discharge initiation

15. NUMBER OF PAGES
166

16. PRICE CODE

17. SECURITY CLASSIFICATION OF REPORT Unclassified	18. SECURITY CLASSIFICATION OF THIS PAGE Unclassified	19. SECURITY CLASSIFICATION OF ABSTRACT Unclassified	20. LIMITATION OF ABSTRACT Unlimited

Contents

2

SYNOPSIS

This final report presents the results of a three-year theoretical and experimental investigation into the fundamentals of gas-fed pulsed plasma thrusters (GF-PPTs). The primary goals was to deepen the basic understanding of how the performance of these devices can be optimized and scaled down to low pulse energies for application as efficient high-specific electric thrusters on small spacecraft. The final report gives a detailed overview of previous research, discusses the electrtomagnetic nature of the acceleration process, the effects of capacitance, electrode geometry, inductance-per-unit length, and discharge initiation on performance and presents theoreticaly derived and experimentally verified performance scaling laws.

In Chapter 1 we present a detailed overview of GFPPT work from the late 1950's until the present year. The scope includes coaxial, parallel-plate, z-pinch and hybrid geometries using ambient fill or pulsed gas injection techniques with hydrogen, nitrogen, argon, and xenon propellants. This review is divided into three parts according to the place where the research was conducted, the overall subject matter, and then an overview and discussion.

In Chapter 2 we present a new gas-fed pulsed plasma thruster performance database and use it to investigate the electromagnetic nature of the acceleration process by identifying trends in the dependencies of the performance parameters on the mass bit, energy, and capacitance. It was previously observed[45] that performance measurements for PPTs operating at low mass bits (< 2 μg per pulse) can be influenced by contamination from diffusion pump oil. Consequently, facility renovations and a new impulse measurement protocol using liquid nitrogen cooled baffles to reduce diffusion pump oil backstreaming were implemented and are discussed. A portion of the database has been duplicated in a cryo-pumped facility at NASA-JPL to verify that the contamination effects have been removed. The intermittent simultaneous operation of the discharge initiation plugs, that was previously observed to degrade the performance, was solved with a new electric circuit and the resulting discharge symmetry verified using a fast-framing camera. The nature of the acceleration process is examined by comparing trends in the performance database with the theoretically expected scaling for electromagnetic acceleration. The performance was found to transition with decreasing mass bit (or increasing I_{sp}) from a mode (Mode I) where the efficiency and the impulse are respectively independent and dependent on the mass bit (and where the efficiency the thrust to power ratio are respectively independent and dependent on I_{sp}) to another mode (Mode II) where the converse statements hold. Furthermore, in mode II the efficiency is independent of energy level and both the efficiency and the thrust-to-power ratio scale with the square root of capacitance as expected in a predominantly *electromagnetic* accelerator.

In Chapter 3 the effects of capacitance, electrode geometry, and inductance-per-unit length on GFPPT performance are explored with efficiency and thrust-to-power measurements on thrusters with varying geometries. In a previous work we have shown that an electromagnetic model of acceleration leads to a

scaling of the performance with the square-root of capacitance and inductance-per-unit-length. We have also experimentally verified the scaling with the capacitance. In the present work we show that large values of capacitance can adversely effect the propellant utilization efficiency which in turn linearly effects the overall efficiency of a GFPPT. This leaves the inductance-per-unit-length as the promising performance scaling parameter. Although parallel-plate electrode geometries typically have higher values of inductance-per-unit-length, co-axial electrode geometries are shown to have higher measured performance at similar operating conditions. The lower than expected performance from parallel-plate thrusters is attributed to wall losses and non-axial current sheet acceleration profiles.

In **Chapter 4** we present the results from a new diagnostic tool for investigating the effects of ignition on the discharge symmetry in GFPPTs. Using a fast-framing camera, up to 16 individual pictures of a single GFPPT discharge can be captured at frequencies as high as 20 MHz. This high framing rate capability allows the discharge initiation and current sheet formation to be visualized with a large degree of temporal resolution. Varying the frame rate, number and size of pictures per discharge, as well as the trigger delay sent to the camera allowed multiple discharges at different stages to be visualized. Various configurations of GFPPT electrode geometry and discharge ignition systems were photographed in operation. It is shown that the large surface flash-over ignitors used in early GFPPT designs are unreliable in providing a constant, symmetric discharge initiation. Smaller semi-conductor spark gap ignitors used in later GFPPT designs have demonstrated more reliable ignition individually, however, asymmetries in the entire discharge still exist. The effect of a modification to the propellant feed system on the asymmetry of the discharge is also presented.

In **Chapter 5** the performance scaling of GFPPTs is investigated theoretically and experimentally. A characteristic velocity for GFPPTs that depends on the inductance-per-unit-length and the square root of the capacitance to initial inductance ratio has been identified. An analytical model of the discharge current predicts the efficiency to be proportional to the GFPPT performance scaling number, defined here as the ratio of the exhaust velocity to the GFPPT characteristic velocity. To test the validity of the predicted scaling relations, the performance of two rapid-pulse-rate GFPPT designs, PT5 (coaxial electrodes) and PT9 (parallel-plate electrodes), has been measured over 70 different operating conditions with argon propellant. The measurements demonstrate that the impulse bit scales linearly with the integral of the discharge current squared as expected for an electromagnetic accelerator. The measured performance scaling in both electrode geometries is shown to be in good agreement with theoretical predictions using the performance scaling number. Normalizing the exhaust velocity and the impulse-to-energy ratio by the GFPPT characteristic velocity collapses almost all the measured data onto single curves that represent the scaling relations for these GFPPTs.

In **Chapter 6** we present additional conclusions derived from our studies. First, we restate the need for the development of GFPPT performance scaling relations and outline the goals of this research work. Next, we summarize the

findings of our studies and suggest future GFPPT design considerations and research topics.

Chapter 1

Review of Previous Research

1.1 Introduction

This is an overview of GFPPT work from the late 1950's until the present year. The scope includes coaxial, parallel-plate, z-pinch and hybrid geometries using ambient fill or pulsed gas injection techniques with hydrogen, nitrogen, argon, and xenon propellants. The topic is generally limited to "pulsed" devices where the total operation time is less than any plasma or current stabilization time, that is, excluding any "quasi-steady" thrusters. Both capacitor and transmission line (lumped inductor-capacitor) energy sources are considered, however, purely inductive discharges are not due to the absence of electrode effects that may be very important in more prevalent GFPPT designs.

This review is divided into three parts according to the place where the research was conducted, the overall subject matter, and then an overview and discussion. In the first part, each section individually covers the work at General Dynamics, General Electric, Lockheed, Republic Aviation, NASA, and Princeton. In the second part, using a combination of repeated information from the previous part as well as new citations from other laboratories, the subjects of current sheet structure and stability (including canting), current sheet acceleration models, theoretical performance scaling, and experimental performance measurement. Both of these parts are designed to stand alone for the convenience of the reader although the first part is designed to provide a much more detailed coverage while the second part is more of a summary. Finally, in the last part, a brief overview of research from over the last half-century and a discussion on the current and future GFPPT research will be presented.

In general, this review tries to make use of peer-reviewed journal publications instead of non-reviewed conference papers or technical reports. Although sometimes these will be used to supplement the information contained in the journal articles, frequently the content is very similar. For each section, there will be a

summary of the research data and proposed theories presented in the reviewed articles as well as a separate discussion sub-section consisting of this author's relevant theories and opinions on the topic. Previous reviews of GFPPTs have followed a similar, although perhaps more compressed, format [1, 2, 3]. In this case, the author is trying to summarize more than simply the best or final results from each group, rather, the history, lineage, progress, and lessons learned along the way are also explained in detail. With this approach, both the reader who is interested in a detailed chronology or a simple summary should both be satisfied.

At this point, it should be noted that with the many ways to measure GF-PPT performance used in the literature including calorimetry, ballistic pendulums, streak and Kerr-cell photographs, electric probes, and thrust stands, only the thrust stand provides a direct measurement that has been accepted by the research community [2] and is not influenced by assumptions of sweeping efficiency, initial propellant density distribution, ionization fraction, etc. However, this technique along with all the others are susceptible to the influences of adsorbed gas and organic mono-layers on the electrode surfaces [4, 5] common to many vacuum facilities and pump-down procedures. Except where noted, the author will *only* use thrust stand data to *compare* performance (impulse, specific impulse, thrust-to-power ratio, efficiency) while elucidating the degree to which, if at all, the investigators took into account the possibility of this type of contamination in their observations.

Part I

Research by Laboratory

1.2 General Dynamics

D.E.T.F. Ashby, R. Dethlefsen, T.J. Gooding, B.R. Hayworth, A.V. Larson, L. Liebing, R.H. Lovberg, and L.C. Burkhardt (Los Alamos). **1962-1966**

Burkhardt and Lovberg began researching "plasma guns" (see Ref. [6]) as a high velocity source of plasma for fusion research in 1962 at Los Alamos [7]. Investigating a coaxial geometry, they used deuterium for propellant that was controlled and radially injected by a solenoid valve through ports approximately half-way down the center electrode. Fast ion-gauge pressure measurements showed that the propellant distribution was relatively gaussian around the injection ports (with all the propellant contained within the electrode volume) just before the discharge. The discharge was initiated when the pressure between the electrodes became high enough for a Paschen breakdown. The overall density and mass bit were controlled by the plenum pressure upstream of the solenoid valve. Depending on pressure, the breakdown occurred near the breach (low pressure with long times before paschen breakdown) or near the propellant ports (high pressure with almost immediate breakdown, frequently asymmetric) [8]. For this accelerator design, the center electrode was the cathode ($r_{outer} = 4.7$ cm, $r_{inner} = 2.5$ cm, radius ratio= 1.88) using a 15 μF capacitor bank charged to 16 kV (1.92 kJ) for each pulse. At a low-pressure test condition using about 40 μg of propellant, the peak current (110 kA) was reached in 0.7 μs suggesting about 100 nH of parasitic inductance and yielding a very oscillatory current waveform.

At these conditions, the sheet speed was observed to asymptote to 125 km/s indicating that the current sheet was permeable and not acting like a "snow-plow". An effective sweeping efficiency of 50% was estimated based on a predicted computer model of the acceleration process. The peak current and current density were observed to decrease monotonically with decreasing initial propellant density. Electric field probe data showed that the radial electric field was close to zero, which is to say that almost the entire capacitor potential was taken up by the expanding magnetic fields and back emf with almost no resistive voltage drop, only 80 V out of 16 kV. Other E-probe data showed that an *axial* electric field exists within the current sheet, along the direction of acceleration. The average value of the integrated axial field, 167 V, is just enough to predict ion velocities of 125 km/s if only half the ions were accelerated to that speed (consistent with a 50% sweeping efficiency). The axial field value was less near the outer electrode (anode), only 50 V, which is consistent with the $1/r^2$ Lorentz force profile, however, the current sheet itself was seen to be very planar from magnetic field data at different radii. The authors suggested this was either due to higher propellant densities near the center electrode or possibly because of increased ion current near the anode with more research being indicated. Lovberg conducted the same kind of measurements using nitrogen and argon in the same device at a later time and found similar, permeable, shock-like behavior [9].

In 1963 Lovberg joined General Dynamics and continued his work along with Gooding and Hayworth on GFPPTs for propulsion applications. They
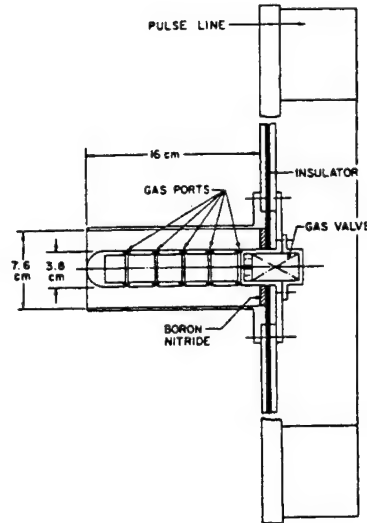
Figure 1.1: Schematic drawing of General Dynamics GFPPT. Taken from Ref. [11].

developed a similar GFPPT design using, again, radial propellant injection (this time, located closer to the backplate) and paschen breakdown initiation [8]. The thruster was slightly smaller with $r_{outer} = 3.8$ cm, $r_{inner} = 1.9$ cm, and radius ratio= 2 with a 5 μF capacitor bank charged between 10-20 kV (0.25-1.0 kJ) for each pulse. At low mass bits they once again reached 10^5 m/s sheet speeds, however spoking instabilities made measurements at higher mass bits difficult to interpret with streak photos. They suggested that when a GFPPT has a "slug-like" propellant distribution, as one would like for dynamic efficiency considerations, it is subject to spoking instabilities. Also, they suspected that their stainless-steel electrodes contributed to the spoking by forming residual "magnetic spots" where the current-spoke would always return. They tested this theory by rotating the center electrode and observing that the spoke attachment followed the rotation[1]

Subsequent thruster designs used more injection ports that were equally spaced down the center electrode to provide a more uniform propellant fill [11] (see Figure 1.1). General Dynamics also developed their own capacitor with distributed internal inductance to give more of a square-wave current pulse (200 kA peak). With a total capacitance of 22 μF charged to 6.3 kV (437 J) and using nitrogen for propellant, they measured sheet velocities of 10^5 m/s

---

[1]Author's note: this could have also been caused by the propellant distribution coming from the cathode propellant injection ports. If one injection port was favored over another yielding a slightly higher mass flow rate and pressure, the spoking instability might follow that injection port. This has been noticed in other GFPPTs more recently as well [10].

and 30% efficiency from a calorimeter. They also saw a significant improvement in performance by reducing the electrode length from 13 to 8 cm, largely attributed to decreased wall loses. The 30% efficiency point was taken with the shorter electrodes which were "tuned" so that the discharge reaches the end of the electrodes when the current crosses through zero. These measurements of sheet velocity suggested that the current sheet in this thruster *did* behave as a snowplow with close to a 100% sweeping efficiency. Faraday cups placed into the exhaust beams measured ion velocities consistent with the previous sheet speed measurements and calorimetry data [12]. The losses in this thruster were attributed to low dynamic efficiency and the inability to recover much, if any, thermal energy in the plasma as a significant fraction of it was thought lost through inelastic electron-ion collisions and the subsequent radiation [13].

In 1964 Lovberg began experiments investigating the current sheet structure including the use of Schlieren photography [14, 15]. In the first set of experiments [14], a parallel-plate geometry was studied for the ease of optical access. With a·height of 3.8 cm and a width of 8 cm, Lovberg believed that field fringing effects would be negligible due to the small aspect ratio of less than two. The accelerator was powered by a 3 μF capacitor charged to 16 kV (384 J) with about 64 nH of measured parasitic inductance. The accelerator exhausted into a small vacuum chamber with the entire volume prefilled to 0.3 Torr of hydrogen (26 μg in 6 cm long electrode volume, $n_0 = 10^{16}$ cm^{-3}). The speed of the first current sheet was measured using photographs at 80 km/s which agreed well with a snowplow model and 100% sweeping efficiency. The second sheet, coming from the second period of current oscillation, traveled at 110 km/s with barely any density gradient detectable by the Schlieren system suggesting that the first sheet had indeed swept up most of the gas between the electrodes.

The Schlieren photographs showed a very planar, thin (0.5 to 1 cm) current sheet with electron densities of 10^{17} cm^{-3} (about 10 times larger than the initial ambient fill) indicating that most of the propellant mass was compressed into a thin layer as a snowplow model would suggest. There were also strong density gradients observed in a very thin layer all along the cathode suggesting that a small part of the plasma was being left behind there. Lovberg speculated that the electrons are trapped in their gyro-orbits and cannot conduct sufficient current to the cathode. He believed that either the cathode would have to be emitting a large amount of electrons to make up for this lack of conduction or that the ions were conducting a bulk of the current near the cathode producing a larger, localized density. Finally, Lovberg noticed that the sheet began to "bifurcate" as the electrodes became more and more "discolored" from each pulse[2]. Cleaning the electrode corrected the problem, however, in tests with nitrogen, the bifurcation always existed with a thin, diagonal sheet leading the main sheet at the anode. He suggested this was "almost certainly related to the larger ion gyro-radius" of the molecules with no further explanation.

His second Schlieren experiment used a specially designed coaxial electrode

---

[2]Please see the following discussion subsection for a possible contamination concern of these measurements
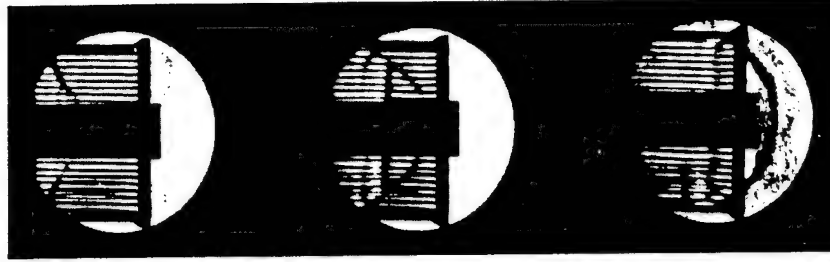
Figure 1.2: Schlieren photographs taken of discharge in slotted, coaxial accelerator using hydrogen propellant at 0.5, 0.7 and 1.0 μs (left to right) after initiation. These figures show positive polarity (center electrode is anode). Taken from Ref. [15].

set with a slotted outer electrode for optical access [15]. Again, the slightly larger thruster ($r_{outer} = 7.5$ cm, $r_{inner} = 2.5$ cm, radius ratio= 3) was backed with the same 3 μF capacitor charged to 16 kV (384 J) to produce a 10^5 A peak current oscillatory waveform. The ambient hydrogen density, however, was very high for this large electrode set giving about 250 μg within the discharge volume. Still, the current sheet reached the end of the electrodes in about 1 μs (6.5 cm long, 65,000 km/s on average) just as the current was crossing through zero.

For the coaxial thruster, the Schlieren photographs showed a very complex distribution of density with a parabolic shaped front centered on the center electrode (anode) followed closely by a ticker, planar front, as shown in Figure 1.2. Throughout the course of the discharge, the parabolic front moved out ahead of the planar front (120 km/s compared to 50 km/s) while the planar front's thickness increased. Although reversing polarity showed minimal effects (the parabolic front always moved out on the center electrode faster), when the center electrode was negatively charged (cathode) the planar front became much more diffuse. In both cases, the parabolic front moved much faster than expected ($> 2x$) from a snowplow model with the ambient mass density, although it did have the shape expected from the non-uniform Lorentz force. The parabolic front was also found to contain between 80-90% of the current with B-dot probes. Plasma densities were estimated to be about 10^{16} cm^{-3}, almost the same as ambient conditions. Once again, Lovberg reached the conclusion that the current sheet in this thruster was permeable and did not act like a perfect snowplow, rather like a strong shock-wave. Lovberg also saw large radial density gradients near the outer electrode (cathode) which could have been caused by either plasma leaking through the optical access slits or by plasma building up near the outer electrode (cathode) walls. Finally, shortening the center electrode had relatively no effect on the plasma front shape or speed with the pinch column beyond the shorter electrode forming a "virtual electrode" with strong radial density gradients.

Lovberg's final current sheet structure experiment used both a capacitor

driven discharge with parallel-plate electrodes, and an inductively driven theta-pinch that sought to eliminate the effects of electrodes altogether [16]. As the second apparatus showed very different behavior than conventional discharges with electrodes, those results will not be included here. Returning to the parallel-plate geometry for its more efficient snowplow behavior and one-dimensional nature, Lovberg used electric field and B-dot probes to infer current conduction through a generalized Ohm's law. Assuming the gas is already fully ionized and in the moving reference frame of the current sheet:

$$\vec{E} + \vec{v}_i \times \vec{B} - \frac{1}{n_e e} \left[\vec{j} \times \vec{B} - \nabla p_e \right] - \eta \vec{j} = 0, \tag{1.1}$$

which includes the Hall effect. Using a right-handed coordinate system with the z-axis in the direction of current sheet motion and the x-axis perpendicular to the electrode surfaces, the vector equation can be broken down into two equations,

$$E_z + v_{ix} B_y - \frac{1}{n_e e} \left[j_x B_y - \frac{\partial p_e}{\partial z} \right] = 0, \tag{1.2}$$

$$E_x - v_{sheet} B_y - \eta j_x = 0, \tag{1.3}$$

with the following assumptions: uniformity in the y-direction and current carried only in the x-direction. Neglecting ion current and assuming the pressure gradient is small,

$$n_e e E_z = j_x B_y. \tag{1.4}$$

This relation infers that the electron current creates an axial Hall electric field which subsequently accelerates the ions. Lovberg goes on to say that, in general, GFPPTs could be called "pulsed Hall accelerators". If the current sheet itself is the ionization source, then Lovberg postulates a slightly different story. Upon entering the sheet, a neutral atom is ionized and both particles begin to rotate about their gyro-centers in the strong magnetic field. Without collisions and assuming that the thruster geometry dimensions are much bigger than the ion gyro-radius, the separation of the ion and electron gyro-centers in the x-direction will cause a displacement current proportional to the rate at which the sheet picks up and ionizes more atoms. In this case, there is no polarization field (the gyro-centers do not separate in the axial direction), and both the ions and electrons effectively carry the current and feel a Lorentz force on ion cyclotron time scales. Near the electrodes, the finite gyro-radius effects dominate with a high voltage sheath required to bring in electrons near the anode, and an axial electric field developing near the cathode where the ions cannot complete a full gyro-orbit. Qualitatively, Lovberg found this to be the case using hydrogen, with strong density gradients near the cathode and about a 100 V sheath near the anode. Using Nitrogen, or any other higher molecular weight propellant, however, he found that "electrode effects" dominated the discharge pattern as the gyro-radius for the ions became on the same order as the thruster's electrode spacing.

The last two publications from General Dynamics included a summary of the work from 1963-1965 in a NASA contract report [17] and a final journal

paper which suggested that a longer, quasi-steady discharge would have a higher efficiency while still benefitting from the arbitrary low power consumption due to the pulsed nature of the device [18]. Without going into further details of the quasi-steady thruster development, and without repeating the information already provided above, the contract report brought out the following points that were not published elsewhere:

- Spoking and other discharge initiation instabilities went away when the dependence on gas pressure and corresponding paschen breakdown to control the initiation timing was removed with the addition of an gas-discharge switch.

- Efficiency of uniformly filled thrusters never exceeded 50% due to dynamic efficiency (calorimetry data).

- A steady-state thrust stand was develop and showed that with pulsed, non-uniform, gas injection the efficiency could be greater than 50%.

- Confirmed Guman's discovery (Ref. [4] of impulse decay with successive pulses and took thrust stand data accordingly, after at least 100 pulses.

- Used a limited number of different charging voltages and gas pressures to determine optimum operating conditions from thrust stand measurements using nitrogen and xenon (see next subsection for a summary of performance data.)

- Found that calorimetry data over-estimated the performance by a significant amount due to inclusion of plasma internal energy captured by calorimeter that is not recovered as thrust.

- The average axial velocity of ions in the exhaust was found to be *greater* than the average velocity calculated from thrust measurements by as much as a factor of two.

- Duplicated General Electric's A-7D thruster (see next section on work at GE) in geometry, capacitance level, propellant delivery, and discharge initiation scheme to find it delivered only about 1/3-1/2 the reported performance.

1.2.1 Summary of GD Performance Measurements

The measurements presented here were performed during the later stages of GFPPT development at General Dynamics [17] using a thrust stand (pulsed operation at 10 Hz gave effective "steady" measurement and average impulse bit) and an appropriately conditioned thruster to eliminate contamination effects. The capacitance was increased to a final value of 140 μF with a distributed inductance giving nearly a square current pulse. The geometry of this thruster was slightly different than that of Figure 1.1. The length of the center electrode was shorter (5.5 cm) with the same radius (1.9 cm) while the outer electrode

was about the same length (15.8 cm) but had a larger radius (6.25 cm). The new radius ratio was about 3.3. The propellant was injected radially at the breech with the discharge initiation timing controlled by a gas-discharge switch. Propellant utilization was measured to be just over 60% with nitrogen and a 350 μs delay. The mass bit was controlled by changing the feed pressure and the quantity was determined by integrating measured density profiles. Both nitrogen and xenon data were used in this study as shown in Tables 1.1 and 1.2 and Figures 1.3 and 1.4. In general, the efficiency varied from 6 to 56%, the specific impulse varied from 350 to 13,000 s, and the thrust-to-power ratio varied from 33.5 to 8.7 μN/W, respectively, depending mass bit and energy. As expected, the highest efficiencies corresponded to the highest energy and lowest mass bit values, however, the thrust-to-power ratio is *largest* at the *lowest* energy and highest mass bit values.

Thrust stand data was also obtained using a GFPPT very similar in design to General Electric's A-7D GFPPT with axial propellant flow (xenon) and a separate high-voltage discharge initiation system. GE's mass injection scheme was duplicated very closely to insure the same propellant utilization ($> 90\%$) and density profiles. While faraday cup measurements of ion velocity and exhaust beam divergence were very similar to those obtained at GE (see next section), thrust stand and performance measurement data disagreed with significantly lower values measured at General Dynamics [17]. Table 1.3 shows performance values at four energy levels. For this device, the efficiency is relatively constant at a fixed energy while the thrust-to-power ratio still shows a tendency to *decrease* with *increasing* energy and decreasing mass bit.

1.2.2 Discussion of Research at GD

The research at General Dynamics can be broken into two related subject areas: current sheet studies (mainly conducted by Lovberg) and performance studies.

Current Sheet Studies. In the current sheet studies, Lovberg used electric field and B-dot probes [7, 9] as well as Schlieren photography to investigate the nature of the current sheet and acceleration process in both parallel-plate [14] and coaxial [15] geometries using mainly hydrogen for propellant. One of the main questions he was trying to answer was if the current sheet behaved as a snowplow or a strong shock-wave.

In the parallel-plate geometry, he saw a very planar, thin current sheet that had an electron density ten times that of the ambient pre-pulse density. In addition, probe data on arrival time agreed well with the visual indications of the front. He concluded that the sheet *did* behave as a snowplow effectively sweeping up all the gas in front of it. He also found that there was a strong polarization field and speculated that the electrons were conducting all of the current, experiencing a Lorentz force which then slightly separated them from the ions. The polarization field that develops as a result of this separation was measured to be enough to explain the subsequent ion acceleration. Using gases

such as nitrogen and argon he saw the sheet "bifurcate" with the bulk of the current being carried on a canted sheet, anode leading cathode. He did not study this phenomenon in depth but suggested that it was a result of the higher molecular weight, and subsequent larger gyro-radii, of nitrogen and argon molecules. It should be noted at this point, however, that the absence of any canting in Lovberg's parallel-plate Schlieren experiments with hydrogen could have been due to surface effects on the electrodes. Lovberg did, in fact, notice the same "bifurcation" in hydrogen after many pulses. He blamed the appearance of this "unstable" behavior on dirty electrodes and cleaned them to find repeatable behavior. Other authors, however, have noticed that discharge behavior only becomes repeatable *after* many pulses due to adsorbed gases collected while the vacuum vessel is exposed to atmosphere and organic monolayers (pump-oil) deposited during pumping [4, 5]. These "contaminants" are blown off the electrode surfaces after a number of pulses, and "cleaning" them as Lovberg did to re-produce the planar sheet would have to include venting the vacuum vessel and going through another pump-down procedure. The extra gas emitted from the surface of the electrodes during a discharge could radically change the overall behavior of the current sheet, especially near the cathode. Still, Lovberg did see the canting using nitrogen and argon by, more than likely, using the same procedure as in those studies with hydrogen. To date, the effects of the electrode surface condition on current sheet canting are still unresolved.

In the coaxial geometry using hydrogen, nitrogen, and argon, he saw very different features depending on polarity. In some of his earliest papers, Ref. [7, 9], the center electrode was at cathode potential and the current sheet seemed to be planar from field probe measurements. With the sheet speed measured from probe data being about twice that expected from a snowplow model and the fact that the current sheet itself was not bowed due to the $1/r^2$ Lorentz force profile, he concluded that the sheet *did not* behave like a snowplow. Electric field data showed a similar polarization field to that seen in the parallel-plate geometry, however, it dropped off towards the anode. Although this might be expected with a non-uniform Lorentz profile, the polarization field was no longer strong enough for the ions to be accelerated to sheet speed near the anode. Lovberg postulated that that the current sheet was permeable and acted more like a strong shock-wave. In fact, what Lovberg might have been observing was a significant contribution from ion conduction along with a permeable sheet.

In the case of the reverse polarity and using the Schlieren technique with a slotted outer electrode (Ref. [15]), the current sheet was seen to separate into two layers. The leading sheet was seen to bow out along the center electrode as should be expected by the non-uniform Lorentz force in a coaxial accelerator. In the second, planar layer, he saw a much more diffuse region that did not conduct much current, possibly from a small amount of ion conduction to the cathode. Integrating the gradient information from the Schlieren photos showed that the electron density was about the same as the ambient conditions indicating that this again *did not* behave like a snowplow, rather like a strong shock. A possible explanation for this behavior was the possibility of ion conduction to the cathode which could leave a large number of recombined molecules near the

cathode moving only with thermal speed, much slower than the sheet speed. The presence of strong radial density gradients near the cathode seemed to agree with that theory, although Lovberg still did not rule out other possibilities corresponding to the electrons carrying all the current.

It is interesting to note that the current rise times are very similar in the two geometries Lovberg tested, however, the current rise per unit width (in the case of a coaxial geometry the average circumference must be used) is very different. To compare the two, consider *unwrapping* the coaxial geometry to make it like a parallel-plate thruster. The effective width is equal to the average circumference of the electrodes. From this comparison, it is easy to see that the effective width of the coaxial electrodes is much greater than the typical parallel-plate geometry. Distributing the same total current over the two geometries, the current density and inductance-per-unit length are much less in the coaxial thruster. Jahn has pointed out that thrusters with current rise rates per unit width of less than $10^{12} A/(m \cdot s)$ have empirically been shown to have less than 100% sweeping efficiency [1]. In the case of Lovberg's experiments, this criteria also holds true: the parallel-plate accelerator has a width of 8 cm and a current rise rate of 250e9 A/s giving about 3e12 A/ms while the coaxial geometry has an average width of 22.6 cm and a current rise rate of 160e9 A/s giving about 0.7e12 A/ms. In accordance with the rule of thumb, the parallel-plate thruster showed behavior like a snowplow while the coaxial geometry did not. In the other coaxial geometry tested at GD, a higher capacitance and smaller average radius electrodes reached current sire rates up to 1.4e12 A/ms [11]. Although the authors did not expressly try to match or exceed this criteria at the time, probe data confirmed that the current sheet was indeed acting like a snowplow in this later coaxial device.

The coaxial thruster tested by Lovberg showed some interesting features depending on polarity. Although Schlieren photos showed a front that seemed to expand depending on the Lorentz force regardless of polarity, electric probe data for the cathode-center configuration showed a very planar current conduction zone. It could be possible that in the negative polarity the non-uniform Lorentz force profile is balanced by some other effect that normally causes canting with the anode leading the cathode. Other researchers have also seen effects from changing the polarity of a coaxial geometry, however, this discussion will be left to Section 1.8 where all this information can be summarized together.

Performance Studies.   The performance studies are well summarized by the previous section and by Ref. al:GDSummary. First, it is important to notice that the instabilities and asymmetries caused by relying on the propellant density to gradually increase and induce a paschen breakdown were completely removed by the addition of a gas switch. There is no reason to think that either a uniform or slug-like initial propellant distribution is inherently more subject to spoking or other instability from a properly initiated discharge. Second, Results from the calorimeter predicted performance greater than what was measured on the thrust stand. By the author's own admittance, thrust stand data is

the only true performance indicator. In addition, GD saw the same effects of impulse decay Guman saw at Republic aviation and measured performance accordingly after at least 100 pulses. This lends credence to their data including the performance measurements of a duplicate GE A-7D thruster that were well below published data provided by GE. This will be discussed in more detail in the next section. Finally, unfortunately researchers at GD performed no real *controlled* experiments to see the effects of capacitance and inductance-per-unit-length on performance.

Impulse Bit (mNs)	Mass Bit (μg)	I_{sp} (s)	Energy (J)	T/P Ratio (μN/W)	Efficiency (%)
1.5	29	5,200	158	9.5	24
3.0	124	2,400	158	19.0	23
3.8	348	1,100	158	24.1	13
2.4	29	8,300	280	8.6	36
3.9	126	3,100	280	13.9	22
5.8	348	1,650	280	20.7	17
3.8	29	13,000	438	8.7	56
5.4	113	4,800	438	12.3	30
7.5	348	2,150	438	17.1	18

Table 1.1: General Dynamics GFPPT Performance using nitrogen. Taken from Ref. [17], runs 46a-46i.

Impulse Bit (mNs)	Mass Bit (μg)	I_{sp} (s)	Energy (J)	T/P Ratio (μN/W)	Efficiency (%)
2.8	120	2,360	158	17.7	21
3.9	543	710	158	24.7	9
5.3	1490	350	158	33.5	6
4.4	120	3,600	280	15.7	28
5.8	543	1,060	280	20.7	11
7.0	1490	460	280	25.0	6
5.4	120	4,500	438	12.3	28
8.1	543	1,500	438	18.5	13
12.1	1490	810	438	27.2	11

Table 1.2: General Dynamics GFPPT Performance using xenon. Taken from Ref. [17], runs 45a-45i.
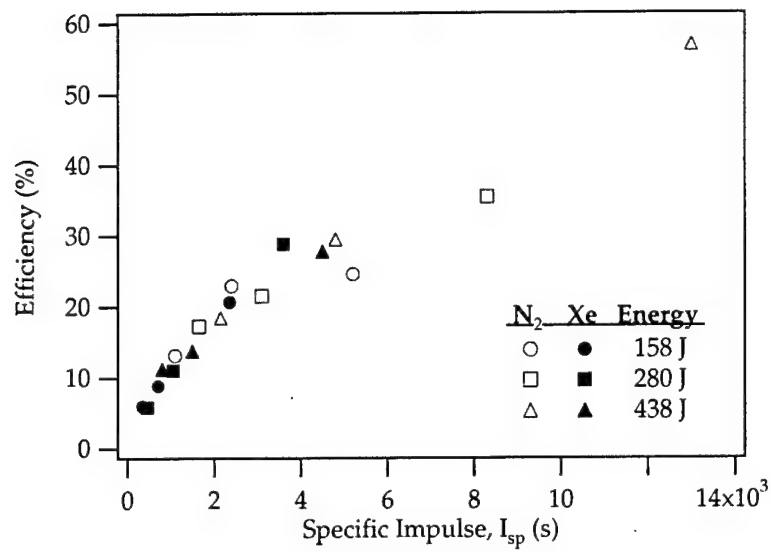
Figure 1.3: Graph of efficiency vs. specific impulse for the General Dynamics GFPPT. Data taken from Ref. [17] and also presented in Tables 1.1 and 1.2.
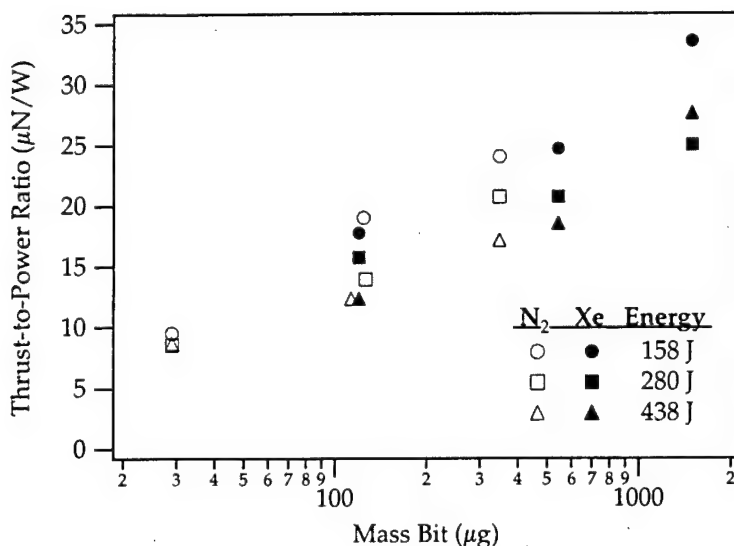
Figure 1.4: Graph of thrust-to-power ratio vs. mass bit for the General Dynamics GFPPT. Data taken from Ref. [17] and also presented in Tables 1.1 and 1.2.

1.3   General Electric

P. Gloersen, B. Gorowitz, T.W. Karras, J.T. Kenney, and J.H. Rowe.
1963-1970

General Electric started research in 1963 with a long, coaxial accelerator closely resembling the first Marshal (see Ref. [6]) plasma guns [19]. The "Model R" accelerator has a *two-stage* design (similar to a conventional single-stage thruster with a gas switch as the first-stage) and used helium, argon, and most often nitrogen as propellants. The second stage provided most of the acceleration with $r_{outer} = 8.75$ cm, $r_{inner} = 5$ cm, radius ratio= 1.75, and length = 47.5 cm from the propellant injection ports (themselves located 7.5 cm from the backplate). Using a 15 μF capacitor bank (for the R-1 and R-2 model) that could be charged up to 13 kV (1.27 kJ) for each pulse, the discharge was initiated with a paschen breakdown in the first stage when the propellant pressure became high enough. Small injection holes allowed some propellant to flow into the main accelerating region before the breakdown in the first stage. With nitrogen flowing at a steady rate of 100 mg/s, according to this author's calculations, only 10% of the propellant remained inside the accelerator at initiation. In this device, peak currents reached 100 kA in about 2 μs with about 90 nH of parasitic inductance and a very oscillatory current waveform[3]. Calorimetry

---

[3]Author's note: initial inductance measured from the current trace (initial slope) actually

Impulse Bit (mNs)	Mass Bit (μg)	I_{sp} (s)	Energy (J)	T/P Ratio (μN/W)	Efficiency (%)
0.65	29	2,200	63	10.3	11
0.72	35	2,100	63	11.4	12
0.73	52	1,400	63	11.6	8
0.86	29	2,900	109	7.9	12
1.03	35	3,000	109	9.4	14
1.15	29	3,900	158	7.3	14
1.32	35	3,800	158	8.4	16
1.46	52	2,800	158	9.2	13
1.73	69	2,500	158	10.9	14
2.04	98	2,100	158	12.9	13
1.73	29	5,900	280	6.2	18
2.05	42	4,900	280	7.3	18
2.02	47	4,300	280	7.2	16
2.22	52	4,300	280	7.9	17
3.33	98	3,400	280	11.2	20

Table 1.3: General Dynamics GFPPT Performance using a similar design to GE's A-7D thruster with xenon propellant. Taken from Ref. [17], runs 80-93.

measurements showed an efficiency of about 12% at 100 J, and increasing the capacitance to 45 μF led to a 26% efficiency at the same voltage. Non-conventional definitions of performance using "energy at terminals" and "effective mass bit", however, made comparing the performance difficult. In addition, although a thrust-stand was operational at this point, it was not used extensively in these first tests.

In 1964, General Electric began parametric performance studies on the effects of changing energy, capacitance, and initial inductance in the Model R accelerators [20]. First, a theoretical model for the acceleration process including a snowplow model for gas accumulation and a circuit equation neglecting the plasma resistance was used to show that reducing the initial inductance would lead to less oscillatory waveforms and better coupling between the driving circuit and the moving discharge. Their model also predicted that efficiency would scale as the inverse of the mass bit with the energy and capacitance kept constant. Increasing energy and capacitance was also found to increase efficiency and specific impulse. Modifications to the Model R gun led to a reduction in initial inductance (15 nH) and improved propellant utilization. Calorimeter measurements showed that the initial inductance drop corresponded to an increase in efficiency up to about 16% at 100 J (an increase by a factor of 1.5). Changes in capacitance (and hence energy at the same voltage) from 15 to 75 μF also

---

gives a *lower* value for the initial inductance close to 45 nH.

improved performance in close to a linear relation. Performance improvements were also seen from increasing the radius ratio, going to a radial instead of axial gas-injection scheme, and shortening the length of the electrodes, especially the inner electrode.

These tre·.ds in performance led to the development of the "Model A" guns that were single stage, pulse injected, coaxial accelerators with much shorter electrodes (20-30 cm), large radius ratios (7-10), and even a smaller initial inductance (about 15 nH) that lead to nearly critically damped current waveforms [20]. The "first stage" of the Model R guns was replaced by a small plenum and solenoid valve combination with pulse times of about 100 ms. Please see Table 1.4 for more details of the accelerator properties and Ref. [20] for a complete account of modifications. Only the most clear and experimentally controlled conclusions will be summarized here.

Model •	r_{inner} (cm)	r_{outer} (cm)	length (cm)	Prop. Injection Area (mm^2)	Capacitance (μF)	Trigger
R-1	5.0	8.75	55	-	15-75	gas
A-1	1.27	8.75	35-20	8.6	15-45	gas
A-3	1.27	12.5	20	8.6	45	gas
A-4(T)	1.27	12.5	20	95	45	gas
A-6	1.27	12.5	20	95	45	elec.
A-7D	1.27	20[†]	20	. 540	45-145	elec.
A-8D	1.27	20[†]	20	680	45	elec.
A-9D	1.27	20[†]	20	830	45	elec.

Table 1.4: General Electric accelerator properties, [†] denotes flared outer electrode from 12.5 to 20 cm over the 20 cm length. Taken from Refs. [20, 21, 22].

In the A-1 and A-3 guns, two zones of performance scaling (again measured with calorimetry) were noticed depending on initial capacitor voltage. At lower energies, initial voltages below 4 kV, the efficiency scaled linearly with voltage while at higher energies it remained relatively constant. Again, as the paschen effect controls the breakdown time and hence the amount of propellant that is able to flow before and after the discharge, higher voltages led to *lower* propellant utilization and hence the efficiency stopped increasing even as the discharge energy was increasing. A small collection of calorimeter performance measurements below the voltage cut-off point for the A-1 accelerator with varying energy and capacitance are shown in Table 1.5. The final design mentioned in Ref. [20], the A-4, had a larger radius ratio, and short electrodes, 10 and 20 cm respectively, with the highest reported energy conversion efficiency of 63% using 45 μF charged to 3 kV (203 J). The A-4T modification had a teflon valve seat yielding higher propellant utilization at higher voltages.

In 1965, based on the success of the A-4 design, GE went through a number

Capacitance (μF)	Voltage (kv)	Energy (J)	Efficiency (%)
15	2	30.0	1
45	2	90.0	18
15	?	67.5	13
30	3	135	21
45	3	203	27

Table 1.5: General Electrics calorimetry measurements for A-1 gun with varying capacitance and initial voltage.

of modifications to produce the A-6,A-7D,A-8D, and A-9D models [21]. The major modifications included:

- Electrical triggers (18 kV "pins") were introduced to eliminate initiation timing dependence on paschen breakdown and increase propellant utilization.

- The outer electrode was flared to increase the inductance change and decrease surface effects (surface to volume increased).

- Larger axial injection ports allowed better conductance of gas inside plenum to discharge volume and increased propellant utilization.

In addition, a steady-state thrust stand replaced calorimetric performance measurements with the thruster operating at 10 Hz, and performance measurements taken as average quantities. General Electric's definition of efficiency included a "Q-factor" (depends only on capacitor type) that compensated for internal impedance losses in the capacitor bank. The power supplied to the thruster was defined as,

$$P = \frac{1}{2}CV_0^2 \left(1 - \frac{1}{Q}\right) f_{pulse}. \tag{1.5}$$

The 45 μF bank described here had a Q-factor of 7 leading to a power that was used in efficiency calculations to be 14% lower than that actually supplied. Erosion measurements showed only 0.25 μg per pulse were lost over 10,000 pulses, and *no* impulse decay or other vacuum facility effect noticed in other labs were reported by GE. The electrode erosion rate was added to the mass flow rate for performance calculations, although this did not significantly alter the results. With the higher propellant utilization efficiencies, *overall* performance increased to $\eta = 70\%$ at 9000 s, 81 J, and 7.4 μg Xe with the A-7D model. Figure 1.5 shows a schematic drawing of the A-7D model.

The increase in propellant utilization was explained in more detail in Ref. [22]. Here the evolution of the mass injection system from the A-4T model to the A-9D was presented with the goal of high propellant utilization. The two major
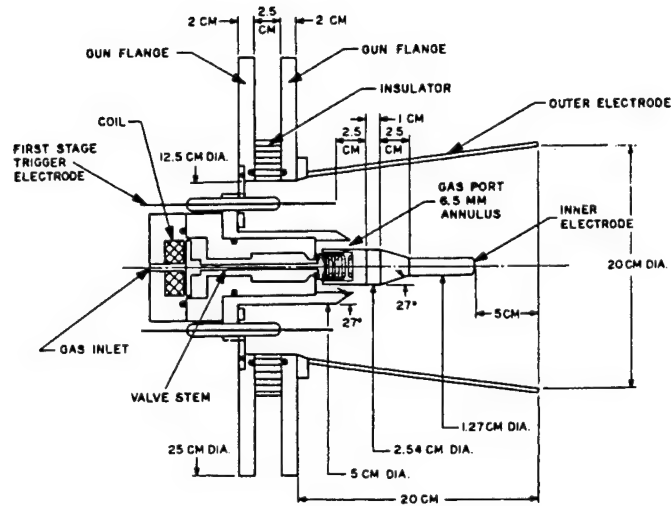
Figure 1.5: Schematic drawing of General Electrics A-7D GFPPT. Data taken from Ref. [22].

changes were to make the injection ports larger for better propellant conductance and to make them face in more of an axial direction to prevent premature self-triggering. Another major contributor to better propellant utilization was the addition of a fast acting solenoid valve. The the o-ring sealed valve was driven by a 4.4 kV supply permitting a 1 ms cycle time. The discharge was initiated by six 18 kV trigger pins 0.7 ms after the valve cycle was started. With the relatively slow thermal velocity of xenon, over 90% of the gas injected before each pulse remained within the electrode volume for the A-7D model. Fast ion-gauge neutral density measurements were used for the mass utilization efficiency calculation and showed that most of the mass was near the cathode (center electrode) and well away from the backplate. The A-8D and A-9D had similar results, however, not as high of performance with slightly more propellant loaded closer to the cathode for the A-8D and too much propellant ejected too quickly (conductance was too large) in the A-9D.

After 1965, the only reports of GE performance came from conference papers. In Ref. [23], Gorowitz, Gloersen, and Karras defended their A-7D performance measurements with detailed descriptions of experiments (but no tables or graphs of data) that eliminated facility effects (except contamination to this author's satisfaction), thermal drifts in the thrust stand, spurious current conduction to the tank or thrust stand, and contribution from electrode erosion. Once again, a 160 % performance improvement was shown from increasing the capacitance from 45 to 145 μF (the Q-factor of the new capacitor bank was given as 14). During a ten hour test running at 5 Hz (36,000 pulses total), the

A-7D model used 30 μg xenon and 65.2 J (950 V) per shot to achieve a 57% overall efficiency with an I_{sp} of 4930 s. The efficiency was seen to scale linearly with specific impulse (constant thrust-to-power ratio of about 20 μN/W) and *not* depend strongly on energy. Similar experiments using nitrogen showed a slightly smaller thrust-to-power ratio of 15 μN/W. A study of changing capacitance showed that efficiency scaled with the square-root of capacitance (within 5-10%) for a constant specific impulse of about 5,000 s. The next subsection gives more measurements with the A-7D model over a variety of mass flow rates and initial voltages. Gorowitz left GE in mid-1966 with his final conference paper providing a mission study using the A-7D which, along with other, later studies, continually quote an efficiency of nearly 60% at 5,000 s [24, 25, 26].

The final journal paper published by GE dealing with GFPPTs was submitted in 1965 and published in 1966 [27]. It described a multi-grid ion collection device that provided measurements of ion velocity and exhaust beam divergence angle with the ability to distinguish between ions of different charge to mass ratios. Although the data agreed with predicted xenon velocities from impulse measurements, carbon and oxygen ions were also present in significant amounts. The amount of these "contaminant" ions varied with each pulse and were not believed to contribute significantly to the thruster impulse.

1.3.1 Summary of GE Performance Measurements

The measurements provided here in Table 1.6 and Figures 1.6 and 1.7 represent thrust-stand measurements from GE's A-7D model using xenon propellant and a 144.5 μF capacitor bank with a Q-factor of 14. Unfortunately, only energy (with Q-factor reduction), specific impulse, and efficiency were given in Ref. [23] where all of this data is reported in graphic form. This is, however, the best source for pure data as GE did not frequently show many points in a data set or any tabular presentation. The mass bit and impulse bit values must, therefore, be inferred from the reported specific impulse, voltage, and efficiency measurements,

$$ I^*_{bit} = \frac{2\eta}{I_{sp}g_0} \frac{1}{2} CV_0^2 \left(1 - \frac{1}{Q} \right), \tag{1.6} $$

$$ m^*_{bit} = \frac{I^*_{bit}}{I_{sp}g_0}, \tag{1.7} $$

where the star superscript indicates the inferred quantities. Finally, it must be noted that out of every lab conducting GFPPT performance measurements on thrust stands [4, 5, 17], GE is the *only* one that did not report any decrease in measured thrust or impulse over the first 100-1000 pulses after pump-down, including tests at similar mass bits and energies. As GE's protocol for measuring thrust is not published explicitly except in very early publications, it is unclear if any preconditioning of the thruster took place before the thrust measurements. More on this topic will be discussed in the following subsection.

Impulse Bit (mNs)	Mass Bit (μg)	I_{sp} (s)	Energy (J)	T/P Ratio (μN/W)	Efficiency (%)
0.92	15	6,050	49	18.9	56
0.95	21	4,600	49	19.5	44
1.03	26	4,100	49	21.4	43
1.00	31	3,300	49	20.7	34
1.39	20	7,000	61	23.0	79
1.43	25	5,950	61	23.6	69
1.46	31	4,850	61	24.2	58
1.59	38	4,300	61	26.3	56
1.31	43	3,100	61	21.7	33
1.30	44	3,000	61	21.4	32
2.05	29	7,300	105	19.5	70
2.17	35	6,300	105	20.7	64
2.18	42	5,300	105	20.8	54
2.38	54	4,500	105	22.7	50

Table 1.6: General Electric A-7D GFPPT Performance with xenon propellant. The impulse bit and mass bit values have been inferred from published efficiency, specific impulse, and energy measurements. Taken from Ref. [23].
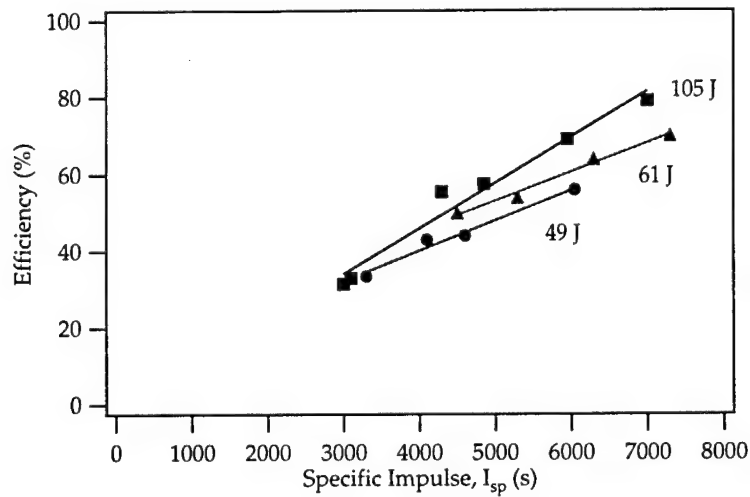
Figure 1.6: Graph of efficiency vs. specific impulse for the General Electric A-7D GFPPT. Data taken from Ref. [23] and also presented in Table 1.6.
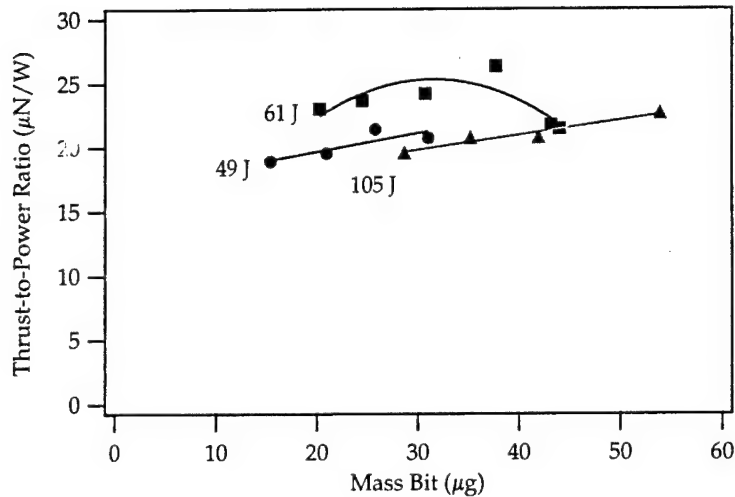
Figure 1.7: Graph of thrust-to-power ratio vs. mass bit for the General Electric A-7D GFPPT. Data taken from Ref. [23] and also presented in Table 1.6.

1.3.2 Discussion of Research at GE

General Electric has reported the highest efficiency measured on a thrust-stand of any GFPPT. After many geometry and propellant injection schemes, their best design, the A-7D, had a large radius ratio of about 16, a 144 μF capacitor bank with only 15 nH of parasitic inductance, and a typical energy per pulse of close to 65 J. Using close to 30 μg of xenon per shot, the efficiency reached 57.5% at a specific impulse of 4850 s. The efficiency was shown to be linear with exhaust velocity over a wide range of mass bits (smaller mass bits gave higher efficiency) with a relatively constant thrust-to-power ratio near 20 μN/W. The propellant utilization efficiency of this design exceeded 90% as a result of using primarily axial injection near the cathode, a 1 ms high-voltage solenoid valve, and separate discharge initiation timing allowed by using six 18 kV trigger pins. GE also conducted a performance survey over five different capacitance values from 50 to 200 μF to find that the performance scaled with the square-root of the capacitance to within 5-10%.

Unfortunately, the researchers at GE did not mention any impulse decay effects that have been observed at three other laboratories testing the performance of GFPPTs on thrust-stands in diffusion pumped chambers [4, 5, 17]. Although researchers at GE did not notice any performance changes from changing the pulse frequency, details of the this experiment and its results were not given. It should be noted that rather than pulse *rate*, the *total number* of pulses has been shown to be more important in conditioning the thruster for proper operation. Without such conditioning, adsorbed gases from the electrode surfaces and organic-monolayers from the roughing and diffusion pump oil can significantly

alter *both* the amount of mass in the discharge and the electrical conduction of the plasma near the electrode surface. Although these effects could indeed be beneficial to performance, *true performance* as would be expected in space operation, can only be measured after a conditioning period, and only as long as pump oil is not allowed to migrate to the thruster electrodes between discharges or test runs.

Three other pieces of evidence suggest that the performance measured at GE might include contamination effects:

1. GE's vacuum chamber used three 32" diffusion pumps that did not have baffles of any kind to prevent back-streaming. The closest pump was less than one meter away from the thrust stand [19].

2. Gridded ion velocity measurements taken by researchers at GE showed a significant amount of carbon and oxygen ions that varied from pulse-to-pulse. Although the total mass of these atoms may not have been significant compared to the xenon ions, their source and their effect on the current sheet structure remains unknown [27]. In addition, heavier molecules from pump oil can appear to have the same charge-to-mass ratio as xenon and be mis-interpreted as normal results.

3. General Dynamics constructed a very similar thruster to that of GE's A-7D and found, at best, a factor of two *smaller* performance [17].

That last item can best be visualized graphically with the results from Tables 1.3 and 1.6 being plotted in Figure 1.8. From this graph, it is easy to see that the data measured at General Dynamics has significantly lower performance than that measured at General Electric. It should be noted that General Dynamics and General Electric were competitors, however, only General Dynamics took the effects of background contaminants into account [17]. After 1970, there are no more publications from GE on GFPPTs, however, research at GE began on ablative pulsed plasma thrusters in the late 1960's with LaRocca.

1.4   Lockheed

P.J. Hart.   *1962-1964*

Lockheed had a similar GFPPT development program compared to other labs. Thruster parametric studies along with computational models attempted to explain and predict GFPPT performance. In his first paper, Hart used a complete circuit model including a constant plasma resistance term and the normal snowplow mass accumulation model to predict the performance of three different accelerator designs. The first two, models A and B, tested the effects of initial inductance, while the third model C tested the effects of capacitance, however, unfortunately, other parameters such as the electrode geometry and energy were also changed simultaneously. In these accelerators, the outer electrode was actually made of a copper screen material to allow light from the
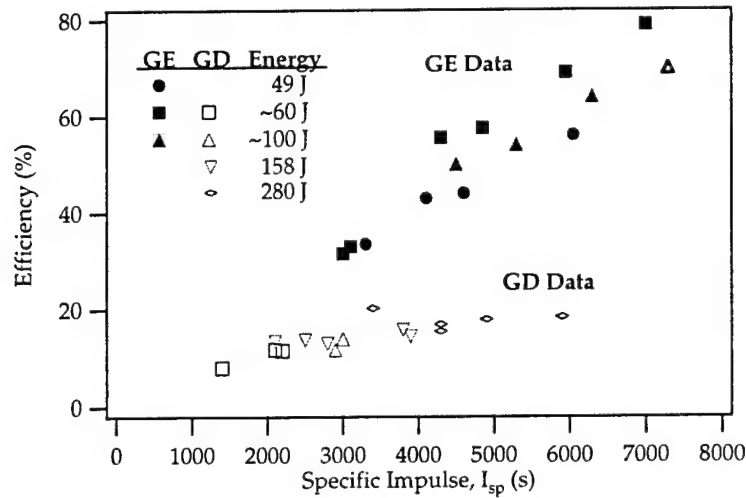
Figure 1.8: Graph of efficiency vs. specific impulse for the General Electric A-7D and General Dynamics A-7D replica GFPPT. Data taken from Ref. [17, 23] and also presented in Tables 1.3 and 1.6.

discharge to reach the rotating mirror of a streak camera. Table 1.7 shows the characteristics of the various designs.

Model	r_{inner} (cm)	r_{outer} (cm)	length (cm)	Init. Ind. (nH)	Capacitance (μF)	Energy (kJ)
A	0.64	2.38	7.0	90	2.0	1
B	0.64	2.38	7.0	240	2.2	1
C	0.74	7.40	84.0	150	300	15

Table 1.7: Lockheed accelerator designs. Taken from Ref. [28].

These parameters were inserted into his circuit-snowplow model and the resulting current sheet trajectory was compared to experimental measurements of sheet speed with streak photographs. In the model, the circuit and momentum equations were integrated until the velocity of the sheet began to slow down or asymptote. Test results using both hydrogen and air showed general agreement with the slope of the light trial (indicating the sheet velocity) front from streak photographs. Subsequent sheets, due to the oscillatory nature of the current waveform, were generally seen to travel *faster* than the first sheet. The measurements of sheet speed agreed relatively well with the snowplow model at high mass bits (the sheet moved slightly faster than predicted at the highest mass bit values) and fell well under the predicted speed at low mass bits, especially in

tests with air. Hart believed this was due to the addition of back-plate insulator material (Teflon) to the discharge having more of an effect at low mass bits. Hart used Teflon because he found it to be the only insulator that provided a uniform, symmetric breakdown near the backplate.

Reducing the inductance and increasing the capacitance both seemed to increase the sheet speed, however, Hart did not believe this trend would continue indefinitely. He measured sheet speeds in the A and B configuration to see that the efficiency of B was nearly half that of A with the corresponding initial inductance gain of 2.7 times. Comparing relatively similar mass loading conditions in the C design, the increase in capacitance, initial inductance, inductance-per-unit-length, and energy led to a five fold increase in sheet speed. He also saw that the subsequent sheets were forming slightly *before* the current zero-crossings, possibly due to inductive effects. Magnetic probe data showed that "loop currents" were forming between each subsequent discharge.

Hart saw some polarity effects at low mass bits. With a positive polarity (anode at center) he saw a fainter, but faster, sheet that was overtaken by another, stronger sheet, possibly from the next current reversal cycle. He dubbed this as "Mode II" operation and thought that it would be preferable for thrusters to work in this way. Unfortunately, it is impossible to distinguish whether the current sheet is canted from streak photos which only show the first front of luminosity on either the anode or the cathode. Mode I operation (higher mass bits) did not show any polarity effects.

Slug-like mass distributions were used in the circuit model although they could not be realized in the experimental accelerators. Hart showed, as expected, that not as much energy goes into internal modes of the plasma for slug-like distributions with the predicted efficiency correspondingly higher. Current waveforms predicted from this slug-model were close to critically damped in character indicating a large rate of inductance change which, in reality, would require long electrodes. Hart also showed that the snowplow model could be modified slightly to account for the finite thickness of the current sheet although it did not significantly effect the results unless the thickness was on the same order as the thruster electrode length.

In later work, Hart tried many different electrode geometries varying primarily the inductance-per-unit-length by changing the radius ratio in coaxial thrusters [29]. Figure 1.9 shows a very high radius ratio thruster tested at Lockheed. Again, he used ambient filled thrusters with Teflon backplates and screen-like outer electrodes to permit optical access for streak photography. The capacitance was set to the lower value of the designs tested perviously, 2 μF, and the initial inductance was further reduced to 48 nH. In these thrusters, the discharge initiation was more stable and symmetric at the lowest gas pressures and smallest inner electrode radius values corresponding to the most ablated mass from the insulator. He also found that the snowplow model over-predicted the performance of the 1" inner electrode case and under-predicted the performance of the 0.063" inner electrode case (more exposed Teflon). He then presented a modified snowplow model that relied on only the force near the center electrode to determine the sheet velocity. This modified model agreed well with the data,
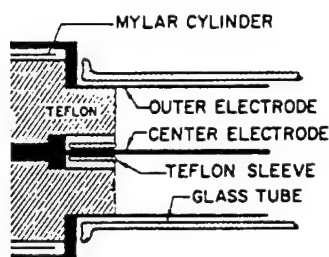
Figure 1.9: Schematic of Lockheed GFPPT with large radius ratio and Teflon backplate. Taken from Ref. [29] and modified to remove extraneous information on distributed inductance and physical discharge switch.

however, it did not take into account the effects of insulator ablation.

1.4.1 Discussion of Research at Lockheed

Hart may have been the first one to realize that a solid-propellant Teflon thruster could have space-flight applications (see footnote in Ref. [29]). Although he tested a variety of geometries, capacitance, inductance, and mass bit values, unfortunately all of his experiments were influenced by the ablation of a significant amount of Teflon from the backplate. With gas propellant mass bits between 10 and 500 μg and discharge energy levels being a 1 kJ or higher, The majority of the discharge could easily have been made up of Teflon at the lowest, middle, and even highest mass bits for the small inner electrodes. Although his computation models are valid (except possibly the modified form of the snowplow model), the results from streak photos that do not distinguish the *radial* position of the current sheet and should not be used as the only diagnostic for these potentially canted sheet. Unfortunately, these results with the Teflon contribution do not provide an adequate comparison or verification of the models that do not include its contribution. The "Mode II" operation showing the fastest sheet speed is probably a result of a very canted current sheet leading down the center electrode (anode) much faster than the true plasma center-of-mass.

1.5   Republic Aviation

L. Aronowitz, P.B. Carstensen, D.P. Duclos, F.P. Fessenden, W.J. Guman, P.M. Mostov, J.L. Neuringer, D.S. Rigney, and W. Truglio.   ***1961-1964***

Research at Republic Aviation (more commonly know later as Fairchild-Republic for their later ablative pulsed plasma thruster work) began with a theoretical paper on the acceleration of a plasma slug [30]. They used a non-

dimensional, constant mass model for the propellant eliminating any dynamic efficiency effects. They did not include any effects of plasma resistance, wall effects or radiation, although they did include a linearly distributed resistance for the electrodes. They tested two cases depending on integration time, however, they did not require a computer to solve the equations. Their "long time" model used asymptotic analysis to integrate the circuit and momentum equations out to an effective infinite time after the discharge. As any solution to the these equations shows a damped current waveform, the current flowing through will be zero and the velocity will be constant as time goes to infinity. Using this technique, the energy stored in the magnetic field and capacitor are always zero by the end of the integration. Along with the simple slug-mass assumption and without including the plasma resistance (instead, using a *constant* electrode resistance), the equations were solved at t=∞. The solution given for the efficiency is,

$$\eta(t = \infty) = 1 - \frac{2}{1 + \sqrt{1 + EL'^2/2m_{bit}R_0^2}},$$

(1.8)

where L' is the inductance-per-unit-length, E is the energy per pulse, m_bit is the slug-mass accelerated, and R_0 is the constant resistance of the electrodes. In another solution case, the "short time" model assumed that the sheet motion was weekly coupled to the external circuit, i.e. that the inductance was *constant*. This assumption makes the problem linear with separate, analytic solutions to the circuit and momentum equations. Again assuming a constant resistance,

$$\eta_{st} = \frac{1}{8}L'^2\frac{E}{m_{bit}}\frac{1}{R_0^2} = \frac{1}{2\sqrt{2}}\frac{L'}{R_0}\bar{u}_e.$$

(1.9)

Including the effects of linear electrode resistance introduces a small correction and gives a cut-off for the initial inductance value where efficiency actually begins to slowly *decrease* for decreasing initial inductance,

$$L_0 \leq \frac{R_0^2 C}{9}.$$

(1.10)

Otherwise, interestingly enough, the initial inductance *does not* enter into the efficiency solutions at all.

Researchers at Republic first ventured into the experimental realm of pulsed plasma acceleration with a z-pinch, coaxial hybrid thruster shown in a cut-away side view in Figure 1.10 [31]. The average turn radius on the outer electrode is about four inches with the initial break-down occurring at the minimum inductance point, near the outer insulator walls. The thruster was designed so that as the current progressed, the stronger Lorentz force near the center electrode would help turn the current sheet to follow the electrodes. Propellant, in most cases nitrogen, was injected radially outward toward the outer insulator walls with the initiation occurring at the paschen breakdown point. At voltages below 2 kV this method of initiation did not always produce symmetric discharges. Therefore, typically 3 kV was used with a 120 μF capacitor bank
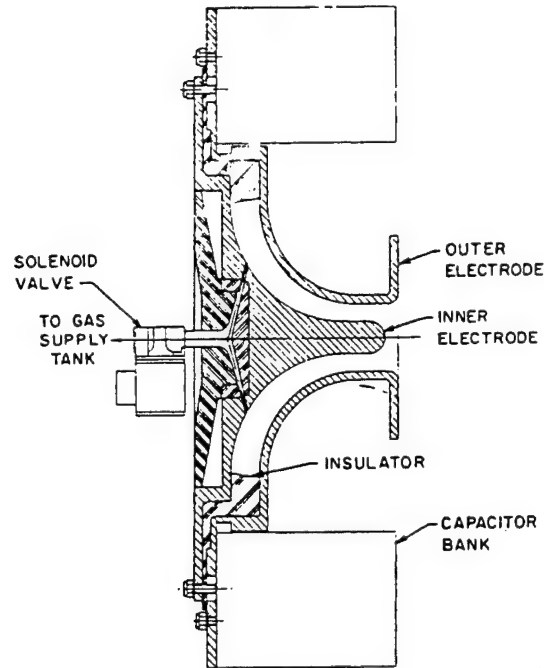
Figure 1.10: Schematic of Republic Aviation GFPPT with z-pinch, coaxial hybrid geometry. Taken from Ref. [32].

(540 J) to produce a uniform current sheet. Maximum current in this device was 235 kA reached in about 1.3 μs indicating an initial inductance of about 20 nH. Typically the discharge volume was filled with 10^{14} cm^{-3} molecules of nitrogen before breakdown.

Photo-detectors, electric probes, and microwave interferometry all detected, with fairly good agreement (within 0.4 μs), the arrival of a plasma front traveling at about 90,000 m/s. The measured plasma density, however, was only on the order of 10^{14} cm^{-3} indicating that a small fraction of the nitrogen was not swept up in the current sheet or was left behind as neutrals recombined on the electrode walls. Still, the speed of this sheet was observed to be linearly proportional to energy, a result predicted by electromagnetic acceleration. The plasma conductivity was also seen to increase with increasing voltage from the interferometry measurements. Later measurements on the same thruster showed that this plasma front was close to perpendicular all along the electrodes although the sheet itself was spreading out as it propagated [32]. Also, a variety of different propellant types (hydrogen, helium, nitrogen, freon) were tried and photocell measurements showed a slight increase in velocity for smaller molecular weights, although all the velocities were relatively similar except in the extreme case of

hydrogen.

William Guman joined the group in 1964 and began thrust measurements using a swinging-gate type thrust-stand that could measure the impulse from individual discharges. He found that regardless of propellant type, electrode material, or background tank pressure (up to 10^{-4}) there was a decay in the measured impulse bit as the total number of pulses since the last facility pump-down accumulated [4]. Tests using a sealed thruster showed that most of this loss in impulse came from the subsequent loss of adsorbed gases obtained on the electrode surface when they were exposed to atmosphere. He also suggested that organic-monolayers from pump-oil contaminants could play a role, although noticeably smaller, in the decay phenomenon as well. Guman also showed that any erosion rate experiments need to include outgassing effects for accurate results.

In the final work at Republic, the delay due to the pulsed-gas and paschen breakdown type of discharge initiation was seen to lead to significant losses in propellant utilization [33]. If the breakdown did not occur quickly enough, propellant would leak out of the thruster electrode volume. If it occurred too quickly, not all of the propellant would make it out into the discharge volume before the breakdown. Guman fixed this problem by adding a gas-discharge switch in series with the accelerator that could be properly timed with the propellant flow [34]. Still, even with the subsequent propellant utilization efficiency improvement, it appears that switch lifetime issues and performance concerns drove Republic Aviation towards a different type of pulsed plasma accelerator, the Teflon ablative pulsed plasma thruster.

1.5.1 Discussion of Research at Republic Aviation

The non-dimensional slug model for acceleration presented in Ref. [30] is interesting in that it provides a resistance that varies as the current sheet moves down the electrodes, however, they found this to be a minimal effect. Their "short time" solutions do not include the effective resistance generated by the current sheet motion. Although this uncoupled model does not represent the electro-mechanical system correctly, it does provide a basis for understanding the performance scaling. Their "long time" solution includes the effects of changing inductance, however, it does not include the effects of subsequent discharges typically found in accelerators with an oscillatory current. It also does not take into account the finite length of electrodes and corresponding maximum change in inductance for a given geometry. Still, with all of these assumptions in mind, it does produce an interesting scaling relation for a slug-like mass, Eq. 1.8, that with Eq. 1.9, shows a monotonic increase in efficiency with increases in inductance-per-unit-length and energy, and decreases in mass bit and external resistance.

Unfortunately, the experimental work with the z-pinch coaxial hybrid thruster never produced an efficiency calculation in the journal publications. They were suggested to be below 50% from calculations of the amount of energy going into the internal losses of the capacitors [32]. Velocity measurements from probes

do not necessarily correspond to the mass averaged exhaust velocity, however, as the sweeping efficiency of the sheet may not be 100%. For this thruster geometry, probably the most difficult thing to calculate was the mass bit which could explain the lack of efficiency data. In the summary produced by NASA Lewis [2], efficiencies were shown to be around 14% at 3,000 s (9.5 μN/W) with nitrogen although the exact configuration of the thruster is unclear compared to the thruster found in journal publications. In his last paper, Guman did measure the thrust-to-power ratio (without specific impulse) and found that it asymptotes to about 9 μN/W at small mass loadings (previously tested conditions) and reached almost an order of magnitude higher, 80 μN/W at higher mass distributions. This was, by far, the largest thrust-to-power ratio measured for any GFPPT at the time, although the efficiency and specific impulse at this condition were probably very low. Still, the lack of continuing research on them at Republic after this measurement is puzzling, although Guman did begin ablative pulsed plasma thruster research soon afterwards.

1.6 NASA Lewis (now NASA Glenn)

S. Domitz, J.E. Heighway, A.E. Johansen, H.G. Kosmahl, C.J. Michels, P. Ramins, N.J. Stevens, and D.J. Vargo. **1962-1965**

Researchers at NASA Lewis began studying plasma guns soon after Marshal (see Ref. [6]) showed that such a device could be useful for propulsion [35]. The coaxial accelerator at Lewis used propellant injection and an ignitron switch to initiate the discharge. The device itself, "Gun A," had an $r_{outer} = 4.75$ cm, $r_{inner} = 1.6$ cm (a radius ratio of about three), and a length of 48 cm, as shown in Figure 1.11. The first 9 cm length of the outer electrode (anode) was Vycor insulator with the propellant injection holes located 18.3 cm from the backplate. The capacitor bank was made up of eleven 1.1 μF capacitors charged up to between 10-30 kV (605-5450 J). The bank alone had a measured initial inductance of 10 nH although the initial slope from current traces predict a value closer to 70 nH which includes the cabling between the capacitors and the accelerator as well the inductance in the accelerator geometry itself. The propellant (hydrogen, nitrogen, or argon) was injected through a fast solenoid valve (100 μs) at various pressures to fill the chamber volume near the propellant injection holes with a 1.1 ms delay between the valve actuation and the ignitron switch closing. The discharge was reported to initiate near the propellant injection holes, and not near the backplate. Faster injection times giving more slug-like mass distributions were later seen to be subject to "spoking instabilities" in Ref. [36].

In these devices, the sheet speed was determined by a series of magnetic probes along the accelerator's outer electrode. The efficiency was calculated using a combination ballistic pendulum-calorimeter to measure the final plasma kinetic energy. Heading Guman's observation of impulse decay [4], ten pulses were fired before any measurements were taken to "outgas" the electrodes. They found the sheet velocity from magnetic probe data to asymptote to a value that
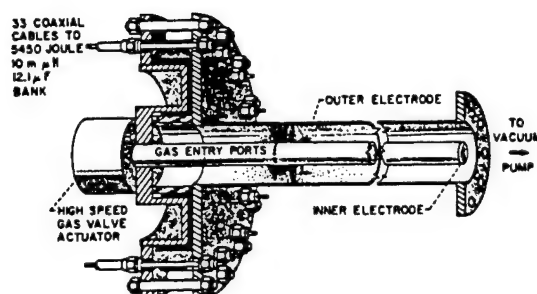
Figure 1.11: Schematic of NASA Lewis "Gun A" GFPPT. Taken from Ref. [35].

was independent of propellant density although there was a weak dependence on molecular weight ($V_{H_2} = 160$ km/s, $V_{Ar} = 100$ km/s). This velocity was measured after a crow-bar discharge occurred near the backplate, approximately 1.5 μs after initiation and in coincidence with the *voltage* reversal or maximum current. The ballistic pendulum-calorimeter measurements showed that argon had the best overall efficiency, 12%, which peaked at about 100 μg of propellant. Hydrogen reached its peak efficiency at a lower mass bit, 10 μg, with a value of 9%. In general, the efficiency was seen to scale with the square root of the energy to mass bit ratio.

These performance measurements along with others testing variations in propellant injection location were later compared to a fairly complete, non-dimensional snowplow model [36]. This model originated from previous work described in Ref. [37]) that used a slug-mass for the injected propellant and the snowplow effect for mass that was eroded from the electrodes and accumulated as the current sheet progressed. As can be expected, the performance in this first model strongly depended on a mass ablation coefficient that determined the ratio of ablated electrode mass to injected propellant mass. The overall trends, however, showed a similar global result to other one-dimensional models with the highest predicted performance corresponding to large values of inductance-per-unit-length, initial voltage, capacitance and small values of initial inductance and resistance.

The more advanced, non-dimensional model presented later in Ref. [36] used a distributed propellant mass and included terms for ionization energy losses, radiation losses, wall drag due to ion diffusion, and heat transfer from the plasma to the electrodes through the inclusion of a plasma energy equation[4]. Comparing results from a simplified model that did not include these effects showed that they consumed no more than 33% of the initial capacitor energy, with smaller discrepancies (less relative loss) at *higher* energies (see Fig. 1.12). Both families of solutions had a similar dependence on the mass profile with the highest per-

---

[4]Please see the following discussion sub-section for a more detailed description on how these terms were handled.

formance predicted for more slug-like distributions. The simplified model also examined the effects of crow-baring at a beneficial time when the current is zero (no energy is stored in the magnetic fields) and at the worst time when the current is maximum. In general, the effects of choosing an appropriate crow-barring time were more pronounced than those observed from the addition of the various loss mechanisms with up to a 40% performance reduction predicted using the "maximum current" crow-bar time. Experimentally, the crow-bar time was seen to depend on accelerator geometry, especially near the breech. Later geometries included an "inhibitor ring" that delayed the crow-bar to when the total current was beyond the maximum value. The performance measurements are presented in more detail in the next section, however, in general, they did not match the predictions in either absolute values or functional form. The author's explain this discrepancy is based mainly on the incorrectly modeled initial mass density profiles.

Research on *unsteady* pulsed plasma thrusters at Lewis stopped in 1965 after it was observed that the current sheet stabilized at the end of the accelerator after 12 μs [38] leading to further "quasi-steady" research. Also in 1965, Researchers at Lewis outside of the experimental group produced a comprehensive review of GFPPT research at many laboratories which brought out the following points [2]:

1. Calorimetry data from many labs did not agree with the subsequent performance data measured on thrust-stands. Thrust-stand data was generally accepted as the most accurate way to measure performance.

2. Crow-baring generally occurs in all unsteady devices sometime between the voltage and current reversal points depending on thruster geometry and driving circuit parameters.

3. The main acceleration mechanism inside the current sheet was believed to be primarily due to the polarization field created by the electrons trapped on an $E \times B$ drift and the subsequent charge separation. The report also mentioned, however, that many of the labs had very different results and disagreed in this area, especially on the influence and existence of ion conduction.

4. The coaxial geometry (compared to pinch or parallel-plate) was suggested to be the best because it trapped all of the electromagnetic fields although it has a large electrode surface area and small inductance-per-unit length which decreased efficiency.

5. Including an electric switch in the discharge initiation process (as apposed to using the Paschen break-down point alone) led to better repeatability, fewer spoking instabilities, and improved propellant utilization while, at the same time, it introduced parasitic inductance and resistance as well as adding reliability questions.

6. The report's conclusion stated the need for a simple performance model that was confirmed by repetitive, experimental performance measurements.

7. The report also stated that the only thing keeping GFPPTs from being used in space was their lack of "heat handling capability" and that research was shifting to quasi-steady devices which might have better performance.

1.6.1 Summary of NASA Lewis Performance Measurements

Researchers at NASA Lewis measured the performance (calorimetry) of four different accelerator designs, as shown in Table 1.8 and taken from Ref. [36]. The thruster was conditioned by firing ten times prior to any measurement. All the designs used mainly argon for propellant and an ignitron switch for discharge initiation timing. The propellant utilization for these devices was estimated to be 100% due to the short valve times (0.1 ms) and long gun barrels. The accelerators were all backed by a 12.1 μF capacitor bank that could be charged up to as much as 30 kV. Reduction in parasitic inductance came from improving the connection between the capacitor bank and accelerator as well as modifications to the gun geometry itself. Even with changes in propellant injection location, initial inductance, and inductance-per-unit-length, no noticeable difference in performance was measured until the electrode length was reduced by slightly more than 50%. Unfortunately, the inductance-per-unit-length was also changed in this configuration making the correlation with the stronger Lorentz force or reduced wall losses difficult to differentiate.

Gun	r_{inner} (cm)	r_{outer} (cm)	length (cm)	Prop. Inject. Location (cm)	Init. Ind. (nH)	Max. Eff. (%)
A	1.6	4.75	48	18	80	12
B	1.6	4.75	46	2	44	13
C	0.64	4.75	46	2	23	13
D	0.32	4.75	20	2	23	22

Table 1.8: NASA Lewis accelerator characteristics. The maximum efficiency point is from calorimetry measurements using argon at close to 4000 J (25 kV) over a range of three to four mass bit values. Taken from Ref. [36].

1.6.2 Discussion of Research at NASA Lewis

Probably the two biggest contributions from NASA Lewis are the most inclusive acceleration model published from any of the labs [36] and the review of GF-PPT research in 1965 [2]. Performance measurements at Lewis did not include thrust-stand data, although the thruster was pre-conditioned to eliminate electrode contamination. In addition, although changes were made in thruster geometry, propellant distribution, and energy, they were not systematically tested so correlation between the modifications and performance improvements could only be speculated. Finally, with only a few mass bit values tested and no

amount of error reported, the trends presented in the data are difficult to draw conclusions from.

Non-Dimensional Snowplow Model. NASA Lewis developed an acceleration model that included the effects of a variable mass distribution (from slug-like to uniform), and losses from "wall drag", heat transfer, ionization, and radiation [37, 36]. The exact details are left to the cited publication, however, the most important points are summarized here:

- The mass distribution function is not related to any physical phenomenon; that is, it does not have an exponential or linear nature that would be expected from pulsed gas injection or a uniform fill.

- Wall drag includes the loss in forward momentum from ions diffusing to the wall based solely on temperature and not current conduction.

- The internal energy of the plasma is based solely on temperature without including pressure effects. Energy is transferred to the plasma from the mass accumulation process and ohmic heating. Energy is lost from the plasma through heat conduction to the electrodes, electron current conduction, ion diffusion and recombination near the electrodes, ionization and radiation. It should be noted (by the author's own admission), however, that although ohmic heating, ionization, and radiation losses appear in the equations, they are not included in the actual solutions.

- The initial temperature is not specified explicitly in Ref. [36] and no profiles for plasma temperature are mentioned or displayed.

The effects of introducing the plasma energy equation are present in comparing the results of the more advanced model with one that does not include these losses, as shown in Figure 1.12. In general, the efficiency is found to follow a similar trend, peaking at a particular "Mass Loading Parameter" that is slightly smaller than what is predicted by the simplified model. The relative loss is smallest at small values of the Mass Loading Parameter. The Mass Loading Parameter is defined as,

$$\mathcal{M} \equiv \frac{2\ell m_0}{L' Q_0^2} = \frac{\ell m_0}{L' C E_0} \tag{1.11}$$

which includes the amount of mass in the initial discharge (m_0), the initial energy (E_0) or charge (Q_0) on the capacitor, the capacitance (C), the inductance-per-unit-length (L'), and the length of the electrodes (ℓ), but *not how the mass is distributed*. This definition makes it hard to differentiate between the various parameters, and its experimental value strongly depends on the initial mass taken up by the current sheet, a very difficult quantity to determine. The authors suggest that the largest loss is through ion diffusion to the walls and that radiation losses are negligible, although they do not provide magnitudes, relative or absolute. They also suggest that radiation cooling could play a significant
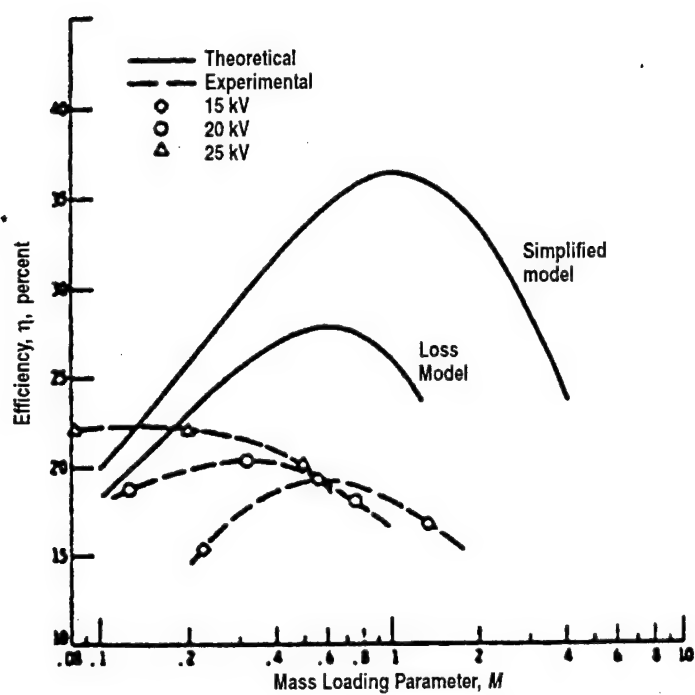
Figure 1.12: Graph of Efficiency vs. Mass Loading Parameter (see Eq. 1.11) including theoretical curves (both simple and advanced) and measured performance data (calorimetry) from "Gun D" using argon at 15, 20, and 25 kV. Taken from Ref. [32].

role, although it is not included in the final plasma energy equation. Although the model did not seem to match well with experimental data, this could have been as much a result of trusting calorimetry performance data then the fault of the model. Without more information on the temperature profile as a function of time, it is hard to say if the plasma energy equation and the associated assumptions were reasonable. Finally, it should be noted that the advanced model did not take crow-baring into account and used a non-dimensionalization scheme based on the *final* inductance of the current sheet at the end of the electrodes, assuming it got there before the current reversed and a crow-bar discharge was formed. The integration was carried out until the current sheet reached the end of the electrodes.

GFPPT Review. The GFPPT review in Ref. [2] provides a very important picture in continuing GFPPT development. Besides presenting a research summary shown in the itemized list of the previous section, it begins to explain why GFPPT research was not pursued much past 1966 in any laboratory at the time besides Princeton. With most efficiencies being below 50% and the reliability of the electrical switches and fast-acting valves in question, research shifted to higher performance quasi-steady pulsed plasma accelerators for main propulsion applications, and the simpler ablative pulsed plasma thruster for attitude control applications. Until only recently, as described in the next section on research at Princeton, have GFPPTs resurfaced as an alternative electric propulsion device once again, this time at lower energy (< 10 J).

1.7 Princeton

N.A. Black, R.L. Burton, E.Y. Choueiri, K.E. Clark, E.A. Cubbin, A.C. Eckbreth, W.R. Ellis, R.G. Jahn, W. von Jaskowsky, T.E. Markusic, P.J. Wilbur, T.M. York, J.K. Ziemer, and D. Birx (SRL Inc.).   ***1962-present***

The research at Princeton on unsteady electromagnetic acceleration can be divided in two categories based on research period, apparatus, and type of investigation. From 1962 until 1970, the structure of the current sheet in a z-pinch was examined including Kerr-cell photos, magnetic and electric field surveys, fast-response pressure probe measurements, and microwave interferometry. In 1969, Jahn wrote "Physics of Electric Propulsion" (Ref. [1]) which included a summary of GFPPT work up to that point. From 1970 until about 1997, Princeton focused on quasi-steady and steady-state MPD thrusters as well as some work dealing with ablative pulsed plasma thrusters in the 1990's. After 1997, in cooperation with Science Research Labs (SRL) Inc., GFPPT research began again focusing mainly on improving the performance of low-energy (< 10 J), low-mass versions of the coaxial guns of the past. In addition, a new study of unsteady current sheet canting and stability began in 1999. As this part of the review includes work by this author, there will be no discussion subsection,
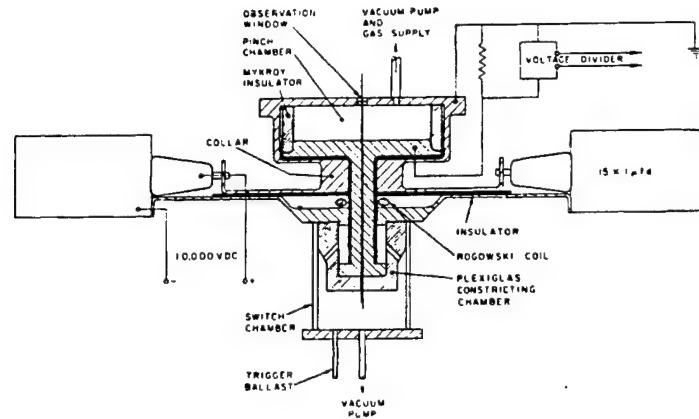
Figure 1.13: Drawing of Princeton Z-Pinch Apparatus. Taken from Ref. [39].

rather, the work at Princeton is divided into two separate subsections based on topic.

1.7.1   Basic Acceleration Scaling Studies at Princeton

Basic acceleration scaling studies began at Princeton in 1962 using a pre-filled z-pinch with a large outer radius [39] and investigating the basic scaling properties of the device. This device was used extensively in many of the studies and has the following dimensions: r_{outer} = 10.2 cm, electrode gap = 5 cm, as shown in Figure 1.13. Fifteen 1 μF capacitors were connected in parallel around the circumference of the device and charged up to 10 kV (750 J) yielding a damped oscillatory waveform with a peak current of 200 kA. The peak current was reached in 0.4 μs after the activation of a gas-switch indicating an initial inductance of about 20 nH [40]. Argon was used for propellant with an ambient pressure of between 20 mT-10 T before the pulse. Optical measurements from streak-photographs showed that the sheet velocity depended on the inverse of the square-root of the density. From magnetic field measurements it was found that a bulk of the current was actually carried near the outside insulator, near the initiation point, soon after the first sheet moved slightly inward. In time, the formation of the second sheet corresponded to the maximum voltage, or current zero-crossing. Internal current loops between the two sheets were found that maintained the same current *direction* in the first sheet. These circulating currents did not appear to be conducted through the electrodes allowing a 7.6 cm radius circle to be cut out of the top electrode and replaced by a pyrex window. Kerr-cell photographs showed that the sheet broke down near the outer insulator uniformly and propagated inward without instability and with no effect seen from the pyrex window. A C-channel like pyrex insert was used to examine the initial breakdown. It was found that although the current sheet still formed near

the lowest inductance points at the electrodes, it remained planer and did not bend outward along the inner surface of the channel. Once again, it propagated uniformly inward indicating that the magnetic effects were greater than the gas dynamic effects.

Studies continued on this device with more magnetic field measurements and the development of a snowplow model for z-pinches based on Rosenbluth's work at Los Alamos (see Ref. [41]). It was found that the luminous front fell slightly behind the current conduction zone of the first current sheet until the second sheet formed and subsequently conducted most of the current. It was also found the both the luminous front and the current conduction zone were traveling *faster* than what was predicted based on a snowplow model. It was concluded that the current sheet formed with the $r_{outer} = 10.2$ cm geometry was permeable with less than a 100 % sweeping efficiency. Inserting an insulating ring at $r = 5.1$ cm was shown to increase the sweeping efficiency to 100 % with the luminous front, current conduction zone, and snowplow model trajectory all in close agreement. The sweeping efficiency was also found to increase with increasing energy and decreasing mass bit. When the sweeping efficiency was high, the sheet velocity was seen to scale as expected with the non-dimensional "magnetic interaction parameter" β,

$$\beta \equiv -\frac{\mu_0 Q_0^2}{4\pi^2 \rho_0 r_0^4} = -\frac{\mu_0}{2\pi}\frac{h}{r_0^2}\frac{CE}{m_{bit}}, \tag{1.12}$$

where ρ_0 is the initial density, r_0 is the outer electrode radius, and h is the distance between the electrodes. Various values of the β parameter were investigated using different mass densities and outer electrode radii. The pinching effect was also found to be a strong function of β with the pinch occurring *before* the current reversal for tests with $|\beta| > 0.2$.

Research then turned to channeling the radially directed sheet into axial momentum. First, Jahn and Black showed that the z-pinch is an inherently good device for dynamic efficiency concerns as most of the propellant mass is swept up in the beginning of the discharge. In Ref. [42], he laid out how the overall efficiency could be greater than 50% as long as the propellant mass was swept up when the current sheet velocity was small. Next, Jahn and Burton built a 15.24 cm diameter, 61 cm long vacuum chamber around the top electrode of the z-pinch and removed the pyrex window to allow the plasma to expand outward from the pinch [43]. The electrode configuration was slightly changed for this device to reduce the parasitic inductance further and improve the sweeping efficiency with an inner radius of 6.35 cm. The peak current was close to 300,000 A with the same 15 μF, 10 kV capacitor bank. The entire volume (including the new exhaust chamber) was filled with argon propellant between 30-1920 mT before the discharge. Various exit orifices were tested (0.95, 1.9, 3.8, 5.1, 7.6, and 10.2 cm diameter holes cut in the center of the top electrode) and it was found that the luminous front expanded with a speed that increased with increasing diameter until the 10.2 cm case. In that case, only a little over 1 cm of electrode was left near the outer insulator, possibly not providing enough

electrode surface area for proper conduction. It was also found that the expanding axial front traveled with a little over half of the original inward radial sheet velocity until, eventually, the core of the pinched plasma caught up and passed the front. The best case of radial velocity change to axial velocity came for the 120 mT case where the ratio of the two velocities was near 80%. Again, current probe measurements showed that the sheet moved radially inward in a very similar fashion to the set-up with the pyrex window, and that the luminous front corresponded well to the beginning of the current conduction front.

In more recent work at Princeton, two models for performance scaling have been developed for coaxial and parallel-plate electrode geometries: a simple, fixed element approximation [44], and a full, single axis, non-dimensional model including the effects of a flared electrode geometry and an exponential mass distribution [45]. In the fixed element solution, primarily modeling a critically damped waveform, the inductance was assumed not to change (although it was given an *average* value, $< L >$, greater than the initial inductance, L_0), and the effective resistance was also held constant. The impulse was assumed to depend solely of the integral of the current squared with the final relation showing a linear dependence on the initial energy stored in the capacitor,

$$I_{bit} = L' \sqrt{\frac{C}{< L >}} E.$$
(1.13)

The efficiency was predicted as,

$$\eta = \frac{I_{bit}^2}{2m_{bit}E} = \frac{1}{2} L'^2 \frac{C}{< L >} \frac{E}{m_{bit}} = \frac{1}{2} L' \sqrt{\frac{C}{< L >}} \bar{u}_e.$$
(1.14)

Note that in this approximation, the average inductance quantity depends on the position of the current sheet and the inductance-per-unit-length. In this way, the efficiency could also be considered to depend on $\sqrt{L'}/\sqrt{\ell_{elect}}$. In any case, both the impulse bit (thrust-to-power ratio) and the efficiency are expected to scale with a square-root of capacitance. In the more complete non-dimensional model, the performance was seen to behave differently depending on the nature of the current waveform. In general, the efficiency increased with decreasing circuit resistance, however, for the underdamped cases with a uniform propellant fill, a maximum in the efficiency was found with a Dynamic Impedance Parameter, α, value near unity,

$$\alpha = \frac{L'^3 V_0^2 C^2}{18 L_0^2 m'},$$
(1.15)

where m' is the mass density gradient coefficient. For critically or overdamped cases with a uniform fill, the efficiency increased with $\alpha^{1/4}$ yielding,

$$\eta \propto \sqrt[4]{\frac{8 L'^3 V_0^2}{9 R_0^4 m'}},$$
(1.16)

with R_0 (including only the internal capacitor resistance and the plasma resistance) having the strongest influence. The thrust-to-power ratio *decreased* with

increasing α for the underdamped cases and remained relatively constant over α for the critically or overdamped cases. Using an exponential mass distribution increased the efficiency and thrust-to-power ratio in accordance with the dynamic efficiency improving. The character of the efficiency was also changed for the underdamped case with the maximum point shifting to much higher values of α, > 10. Higher values of α, however, were also seen to require very long electrodes with total inductance changes on the order of $100 \times L_0$ which are very difficult to achieve in reality. The nature of the thrust-to-power ratio did not change for the exponential mass distribution. Using flared electrodes also improved performance, but not to the same extent as the non-uniform propellant density. Further development of this model including crow-baring for the underdamped cases and finite electrode effects are ongoing at Princeton.

1.7.2   Current Sheet Structure Studies at Princeton

Three PhD theses [46, 47, 48] and three journal publications [49, 50, 51] by Burton, Ellis, and York, respectively, examined the structure of the current sheet through electric and magnetic field probing, microwave interferometry, and fast-response pressure measurement. These three sources will be combined (Note: Ref. [50] provides the best summary of the work as it is published after all the work had been completed) to form a coherent picture of current sheet structure as developed at Princeton. Although all of these measurements are taken at the midline of the z-pinch apparatus and at a radius half-way between the outer insulator and the center, there is no reason to think that a similar structure shouldn't exist in other pulsed accelerators with different geometries. The reader should consult all of these references for the entire story including the model development between references. Only the most simple, coherent results will be reproduced here.

First, the author's start with a generalized Ohm's Law in the frame of the moving current sheet (current sheet moves in *radial* direction in a z-pinch),

$$\vec{j} = \sigma_0 \left(\vec{E} + \vec{v}_i \times \vec{B} + \frac{\nabla P_e}{n_e e} \right) - \frac{\Omega_e}{|B|} \vec{j} \times \vec{B}. \qquad (1.17)$$

where all the terms here have the familiar definitions. Note that the Hall conductivity for the electrons (but not the ions) was included because the chamber dimensions were assumed to be much larger than the electron gyro-radius, but smaller than the ion gyro-radius. Also, the effects of ion-slip were not included, and an assumption of complete, single ionization occurring as soon as the molecule enters the sheet was held throughout the publications. The electric and magnetic fields were measured with probes [49] while the scalar plasma conductivity, plasma temperature, and density were measured by microwave interferometry [50]. The Hall parameter was inferred from these measurements as was the electron pressure from the kinetic relation, $P_e = n_e k T_e$. Only the azimuthal magnetic field was found to be significant while, similarly, only the radial and axial components of the electric field were important. In the moving

REGION: | I | II | III |
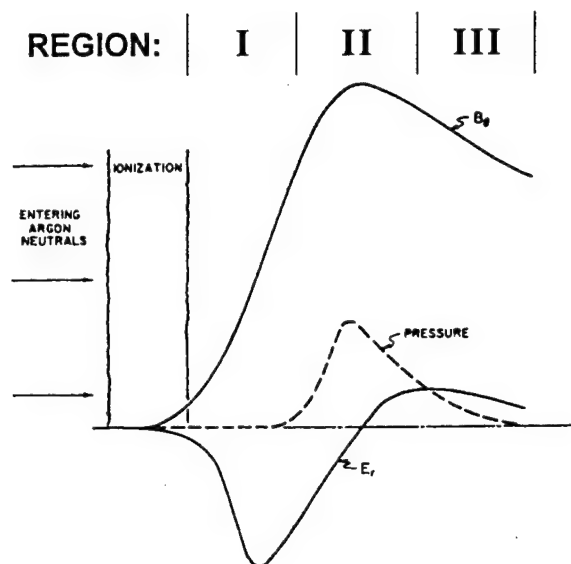
Figure 1.14: Radial electric field, azimuthal magnetic field, and heavy species pressure profiles in the current sheet frame. Taken from Ref. [49] with modifications to show regions identified in Refs. [50, 51]. The area of expected pressure increase was confirmed in Ref. [51]

frame of the current sheet, the radial ion velocity is assumed to start at sheet speed (measured from streak and Kerr-cell photos as well as probe arrival time data) and slow to zero, eventually traveling with the current sheet. As the axial current density is known from total current measurements as well as magnetic field probe data, only two unknowns remain: the radial current and the axial ion velocity. Measurements of these parameters in the current sheet frame of reference are presented in Figure 1.14.

It should be noted that the axial electric field should be expected to be very nearly balanced by the back EMF of the moving current sheet so that the *axial* electric field actually dominates the conductivity. As seen from the measurements, this was found to be true with the appearance of three regions bounded by the character of the radial electric field. In Region I, the radial electric field is very large and caused by the separation of the electrons caught on an $E \times B$ drift while the ions have a large amount of momentum and penetrate deeper into the sheet. This radial electric field does, however, slow down the ions into Region II, although it emphis not enough to slow the ions down completely to sheet speed. Region I was found to be dominated by axial electron current making up a significant fraction of the total current, but *not* enough for the *entire* current. Region I was found to be about 5 mm thick for argon. As the separation of the ions and electrons induces a radial polarization field, it

also creates a radial current. This radial current, although relatively small, interacts with the azimuthal field enough to cause the ion trajectories to deflect towards the cathode. In Region II, with the ions now moving slower and slightly deflected, *axial ion current* dominates with ions recombining on the electrode surface to complete the total current. This produces a $j_{iz} \times B_\theta$ that further decelerates the ions to sheet speed. Region II was also found to be the location of a large heavy species pressure gradient. As the radial electric field actually reverses sign (although not to the same magnitude) in Region II, the electrons actually try to drift against the current flow, however, with the greater ion density, collisions dominate and they remain relatively stationary with respect to the sheet. In Region III, the axial electric field is still negative, although smaller and returning to zero. As the ion density is low here, there is actually the possibility of a small reverse current being carried by the electrons in the trailing edge of the current sheet. The total sheet was found to be about 1 cm thick at the center line with a slight tilt, anode front leading cathode.

This tilt or cant of the current sheet has been investigated in more recent work at Princeton in a parallel plate accelerator [52]. In brief, optical measurements of sheet speed and tilting angle have qualitatively found that larger molecular weight propellants experience more canting, and that the canting angle is independent of initial voltage or peak current. Research is continuing with Schlieren photography.

1.7.3 Performance Measurements of Low-Energy GFPPTs at Princeton

In 1997 Princeton's Electric Propulsion and Plasma Dynamics Laboratory (EP-PDyL) began developing low-energy GFPPTs in cooperation with Science Research Laboratory, Inc. (SRL). The research focused on the following goals [53]:

1. Developing a low-mass (low-energy) GFPPT with the same or better performance as GFPPTs at higher energy. A target was set for 50% efficiency at 5000 s (thrust-to-power ratio of about 20 μN/W) based on the results from GE, but using only 1 J per pulse.

2. Designing a GFPPT that has a 100% mass utilization efficiency using existing, space-qualified valves that have greater than a one million cycle lifetime.

Achieving the these goal included:

- Using solid-state switching technology to increase pulses rates to above 4 kHz for high propellant utilization.

- Grouping pulses together in *bursts* to allow thrust and power modulation while also reducing the total number of valve cycles over the lifetime of the device.

- Developing a highly accurate ($< 10\%$ error), low-impulse (($< 100\mu$Ns), thrust stand and high-speed current sheet visualization techniques.
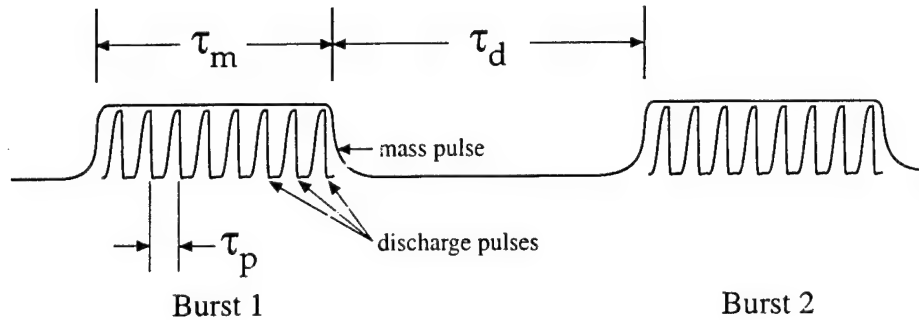
Figure 1.15: Schematic of a burst of pulses in an SRL-EPPDyL GFPPT.

- Rapid thruster prototyping to examine changes in geometry, propellant injection, discharge initiation, and driving circuit.

- Creating a low-energy discharge initiation system that provides a reliable, uniform, symmetric current sheet without inducing a large amount of erosion.

- Deriving and testing performance scaling laws based on simple analytic and complex non-dimensional models for current sheet acceleration.

To date, nine generations of SRL-EPPDyL GFPPTs have been tested with many modifications on each generation. Using a low-voltage (250 V), low-inductance (< 5 nH) capacitor bank (45-270 μF, 1.4-8.4 J), these GFPPTs have close to critically-damped current waveforms with no noticeable crow-baring. Peak currents are close to 10 kA with pulses lasting about 5 μs. As shown schematically in Figure 2.1, during a burst the valve is only cycled once, therefore, the ultra-fast, high energy valves used in previous GFPPT designs are not required. As the propellant flows at a constant rate, the propellant utilization is dictated by the pulse frequency and the thermal velocity of the propellant. For example, using argon ($v_{th} \approx 400$ m/s) and a 4 kHz pulse frequency, the electrodes are required to be at least 10 cm long to ensure that none of the propellant escapes outside of the discharge volume between pulses.

Although many different GFPPT designs have been tested at EPPDyL, the fifth-generation (designated as PT5) has undergone the most extensive performance measurements. Since its original design, changes have been made to its discharge initiation system and propellant distribution [10] as well as the performance measurement technique to insure proper conditioning [5]. As shown in Fig. 2.2, PT5 uses a stainless-steel, coaxial electrode set with an outer to inner electrode radius ratio of approximately four and a total volume of 350 cm^3. It uses four semi-conductor type surface-flashover spark plugs mounted on the inside of the outer electrode (cathode) at 90 degree azimuthal intervals to initiate the discharge uniformly. The main discharge is driven by a low-inductance (10 nH) 130 or 270 μF capacitor bank which is capable of being

Figure 1.16: Schematic of SRL-EPPDyL PT5.

charged to 250 V giving a maximum energy per pulse of 4 or 8 J, respectively. The entire thruster has a mass of approximately 6 or 8 kg depending on the capacitance level and including the electrode mass as well as the thruster housing mass. High-speed photographs of the discharge were taken with an Imacon Fast-Framing Camera (IFFT) at rates of 500,000 frames per second. A series of IFFT frames of PT5 showing the symmetrical discharge initiation are presented in Fig. 2.5. Before the modifications to the gas manifold were made to make propellant injection more uniform, the discharge initiation was seen to occur near the region of highest pressure. This is a similar result to those researchers who found spoking instabilities when the discharge was allowed to initiate based solely on a Paschen breakdown without an external switch.

Two energy levels for each of two capacitance values were tested over ten different mass bit values each yielding a 40-point GFPPT performance database. Four graphs which show PT5 performance as a function of mass bit and specific impulse with the capacitance and the initial stored energy level as parameters are shown with error bars in Fig. 2.11. Each point represents at least twenty trials including separate measurements of impulse, mass bit, and energy at the same conditions. Values of the performance data are given at the end of this section in Table 1.9. It is evident from all the plots in Fig. 2.11 that for each curve there is a transition with decreasing mass bit (or increasing I_{sp})

Figure 1.17: Unfiltered Imacon Fast-Framing Camera photos of a typical PT5 discharge looking straight into the discharge chamber using 0.5 µg argon and 4 J of energy per pulse. The photos seen here are spaced by 1 µs going from right to left and top-right to bottom-left.

from a mode (Mode I) where the efficiency and the impulse are respectively independent and dependent on the mass bit (and where the efficiency the thrust to power ratio are respectively independent and dependent on I_{sp}) to another mode (Mode II) where the converse statements hold.

Simple analytic models presented in the previous section show that the efficiency and thrust-to-power ratio should scale with the square-root of capacitance and not depend on the energy (at a constant exhaust velocity) for an electromagnetic accelerator. These trends are evident in Mode II where the efficiency increases linearly with the specific impulse and the thrust-to-power ratio is relatively constant.

It is interesting to note that the performance scaling suggested for a thruster where electrothermal acceleration is dominant are quite different[54]. In that case, the impulse bit is expected to scale with the square root of the discharge energy to mass bit ratio and not depend directly on capacitance or inductance change. In addition, the efficiency of a pure electrothermal accelerator is expected to be constant over wide range of specific impulse, energy and mass bit values. While the efficiency as seen in panels c and d of Fig. 2.11 is indeed independent of mass bit and I_{sp} at high mass bit values (i.e. Mode I), it does show a dependence on energy, albeit a weaker one than for Mode II. This tends to indicate that the acceleration in Mode I may be due to a combination of both electrothermal and electromagnetic effects. Again, as the losses associated with sweeping up the propellant are not accounted for in these predictions, an explanation for trends in Mode I could be a function of improved dynamic efficiency as well.

Figure 1.18: Performance of PT5. Graphs (a) and (c) show the impulse bit and efficiency as a function of mass bit. Graphs (b) and (d) show the thrust-to-power ratio and efficiency as a function of specific impulse. All graphs contain four curves which show changes in performance due to changing capacitance values and initial stored energy levels.

Figure 1.19: Cathode of SRL-EPPDyL PT7 showing the damage to the surface-flashover spark-plug after 1.5 million pulses.

Later generations of SRL-EPPDyL GFPPTs were used to examine lifetime issues and inductance-per-unit length effects. PT7, a parallel-plate "quad" design (see Ref. [55]), was pulsed 1.5 million times at a discharge energy of 2 J with 0.3 μg of xenon propellant per shot. As seen in Figure 1.19, the single spark-plug initiation system used in this design was severely damaged with measured erosion rates of 0.2 μg per shot. Although the spark-plug did not short-out in this test as it did in a subsequent 100,900 pulse test, it is seen to be the lifetime limiting component of this GFPPT design. Later designs switched to a lower-energy RF spark-plug (PT8, see Ref. [56]) and an even smaller surface-flashover plug (PT9, see Ref. [57]) that did not have an electrode in common contact with the thruster electrodes. Erosion rates have now been measured to be below 0.1 μg per pulse in both systems, however, system mass and life-time concerns still need to be addressed. The latest design, PT9, was also used to examine the effects of inductance-per-unit-length on performance although the pyrex side-walls used to contain the plasma in the parallel-plate geometry were suspected to induce a large amount drag on the current sheet, reducing performance [57]. More recent studies at EPPDyL include testing PT9 without sidewalls, and will be presented later this year.

Cap. (μF)	Energy (J)	m_{bit} (μg)	I_{bit} (μN-s)	I_{sp} (s)	η (%)
270	4.0	0.20	11.6	5940	8.53
		0.25	12.0	4890	7.20
		0.30	11.9	4060	6.01
		0.35	12.0	3500	5.22
		0.40	12.0	3060	4.56
		0.50	13.2	2680	4.35
		0.75	16.9	2290	4.77
		1.00	18.6	1900	4.35
		1.50	22.3	1520	4.16
		2.00	27.6	1410	4.70
	6.0	0.20	19.5	9930	15.8
		0.25	18.6	7600	11.6
		0.30	19.8	6720	10.9
		0.35	18.5	5400	8.16
		0.40	18.6	4740	7.26
		0.50	19.5	3990	6.42
		0.75	23.2	3160	6.12
		1.00	26.3	2680	5.91
		1.50	31.1	2120	5.40
		2.00	37.1	1890	5.79
130	2.1	0.20	3.32	1690	1.37
		0.25	3.39	1380	1.15
		0.30	3.64	1240	1.10
		0.35	3.97	1160	1.11
		0.40	4.00	1020	0.99
		0.50	4.80	980	1.12
		0.75	6.24	848	1.21
		1.00	7.42	757	1.23
		1.50	9.30	632	1.21
		2.00	9.75	497	0.99
	4.0	0.20	7.68	3920	3.81
		0.25	7.38	3010	2.80
		0.30	7.32	2490	2.31
		0.35	7.74	2260	2.21
		0.40	8.21	2090	2.16
		0.50	9.29	1900	2.20
		0.75	12.2	1670	2.50
		1.00	14.7	1500	2.64
		1.50	18.7	1270	2.76
		2.00	21.4	1091	2.68
$\pm$1%	$\pm$2%	$\pm$2%	$\pm$8%	$\pm$5%	$\pm$10%

Table 1.9: PT5 performance data for capacitance values of of 130 and 270 $\pm$2 μF and energy levels of 2.1, 4.0, and 6.0 $\pm$0.1 J. The last row in the table is the average error from each measurement.

Part II

Research by Subject

This part of the review is designed for those readers who would rather see information presented by subject in GFPPT research rather than the entire body of work from each particular laboratory alone. With that in mind, much of the information presented in this part of the review is duplicated from Part I including the relevant citations, but not figures or tables. Some additional work that is not from any of the major laboratories or was related to work in other fields and not presented in Part I are also cited in the sections on current sheet structure and acceleration model development.

1.8 Current Sheet Structure

Two laboratories (General Dynamics run by Lovberg, and Princeton by Jahn in the 1960's) made investigating the current sheet structure their primary task. Their research will be presented, first, individually, then used in a discussion subsection that covers all work related to current sheet canting that this author could find in the literature. Some interesting trends dealing with the permeability of the sheet and its effectiveness as a "snowplow" will be discussed in a following section on performance scaling.

1.8.1 Current Sheet Structure Research at GD

In the current sheet studies at General Dynamics, Lovberg used electric field and B-dot probes [7, 9] as well as Schlieren photography to investigate the nature of the current sheet and acceleration process in both parallel-plate [14] and coaxial [15] geometries using mainly hydrogen for propellant. One of the main questions he was trying to answer was if the current sheet behaved as a snowplow or a strong shock-wave.

In the parallel-plate geometry, he saw a very planar, thin current sheet that had an electron density ten times that of the ambient pre-pulse density. In addition, probe data on arrival time agreed well with the visual indications of the front. He concluded that the sheet *did* behave as a snowplow effectively sweeping up all the gas in front of it. He also found that there was a strong polarization field within the sheet and speculated that the electrons were conducting all of the current, experiencing a Lorentz force which then slightly separated them from the ions. The polarization field that develops as a result of this separation was measured to be enough to explain the subsequent ion acceleration. Using gases such as nitrogen and argon, however, he saw the sheet "bifurcate" near the anode with the bulk of the current being carried on a canted sheet, anode leading cathode. He did not study this phenomenon in depth but suggested that it was a result of the higher molecular weight, and subsequent larger gyro-radii, of nitrogen and argon molecules. Regardless of propellant, Lovberg noticed a thin but strong density gradient in a small layer all along the cathode surface.

In the coaxial geometry using hydrogen, nitrogen, and argon, he saw very different features depending on polarity and molecular weight. In some of his earliest papers using hydrogen, Ref. [7, 9], the center electrode was at negative

potential (cathode) and the current sheet seemed to be planar from field probe measurements. With the sheet speed measured from probe data being about twice that expected from a snowplow model, and the fact that the current sheet itself was *not* bowed outward due to the $1/r^2$ Lorentz force profile, he concluded that the sheet did *not* behave like a snowplow. Electric field data showed a similar polarization field to that seen in the parallel-plate geometry, however, it dropped off towards the anode. Although this might be expected with a non-uniform Lorentz profile, the polarization field was no longer strong enough for the ions to be accelerated to the observed sheet speed near the anode. Lovberg postulated that that the current sheet was permeable and acted more like a strong shock-wave in this case. In another case with reverse polarity, using the Schlieren technique (with a slotted outer electrode, Ref. [15]) the current sheet was seen to separate into two layers. The leading, thin sheet was seen to bow out along the center electrode as should be expected by the non-uniform Lorentz force in a coaxial accelerator. In the second, planar layer, he saw a much more diffuse region that did not conduct much current, possibly from a small amount of ion conduction to the cathode. Integrating the gradient information from the Schlieren photos showed that the electron density was about the same as the ambient conditions indicating that this again *did not* behave like a snowplow, rather like a strong shock. A possible explanation for this behavior was the need for ion conduction to the cathode which could leave a large number of recombined molecules near the cathode moving only with thermal speed, much slower than the sheet speed. The presence of strong radial density gradients near the cathode seemed to agree with that theory.

The coaxial thruster tested by Lovberg showed some interesting features depending on polarity. Although Schlieren photos showed a front that seemed to expand depending on the Lorentz force (bowed outward near the inner electrode) regardless of polarity, electric probe data for the cathode-center configuration showed a very planar current conduction zone. It could be possible that in the negative polarity the non-uniform Lorentz force profile is balanced by some other effect that normally causes canting with the anode leading the cathode. Other researchers have also seen effects from changing the polarity of a coaxial geometry which will be covered in more detail in following subsections.

1.8.2 Current Sheet Structure Research at Princeton

Three PhD theses [46, 47, 48] and three journal publications [49, 50, 51] by Burton, Ellis, and York, respectively, examined the structure of the current sheet through electric and magnetic field probing, microwave interferometry, and fast-response pressure measurement. These three sources will be combined (Note: Ref. [50] provides the best summary of the work as it is published after all the work had been completed) to form a coherent picture of current sheet structure as developed at Princeton. Although all of these measurements are taken at the midline of the z-pinch apparatus and at a radius half-way between the outer insulator and the center, there is no reason to think that a similar structure shouldn't exist in other pulsed accelerators with different geometries.

The reader should consult all of these references for the entire story including the model development between references. Only the most simple, coherent results will be reproduced here.

First, the author's start with a generalized Ohm's Law in the frame of the moving current sheet (current sheet moves in *radial* direction in a z-pinch),

$$\vec{j} = \sigma_0 \left(\vec{E} + \vec{v}_i \times \vec{E} + \frac{\nabla P_e}{n_e e} \right) - \frac{\Omega_e}{|B|} \vec{j} \times \vec{B}. \tag{1.18}$$

where v_i is with respect to the current sheet velocity, and E is the net field including the applied field and the back emf contribution from the moving sheet. Note that the Hall conductivity for the electrons (but not the ions) was included because the chamber dimensions were assumed to be much larger than the electron gyro-radius, but smaller than the ion gyro-radius. Also, the effects of ion-slip (sheet permeability) were not included, and an assumption of complete, single ionization occurring as soon as the molecule enters the sheet was held throughout the publications. The electric and magnetic fields were measured with probes [49] while the scalar plasma conductivity, plasma temperature, and density were measured by microwave interferometry [50]. The Hall parameter was inferred from these measurements as was the electron pressure from the kinetic relation, $P_e = n_e k T_e$. Only the azimuthal magnetic field was found to be significant while, similarly, only the radial and axial components of the electric field were found to be important. In the frame of the current sheet, the radial ion velocity is assumed to start at sheet speed (measured from streak and Kerr-cell photos as well as probe arrival time data) and slow to zero, eventually traveling with the current sheet. As the axial current density is known from total current measurements as well as magnetic field probe data, only two unknowns remain: the radial current and the axial ion velocity. Measurements of these parameters as a function of time as the current sheet sweeps by are presented in Figure 1.14.

It should be noted that the axial electric field should be expected to be very nearly balanced by the back EMF of the moving current sheet so that the axial electric field actually dominates the conductivity. As seen from the measurements, this was found to be true with the appearance of three regions bounded by the character of the radial electric field. In Region I, the radial electric field is very large caused by the separation of the electrons caught on an $E_r \times B_\theta$ drift while the ions have a large momentum and penetrate deeper into the sheet with only a slight deflection towards the cathode. This radial electric field does, however, slow down the ions into Region II, although it emphis not enough to slow the ions down completely to sheet speed. Region I was found to be dominated by axial electron current making up a significant fraction of the total current, but *not* the *entire* current. Region I was found to be about 5 mm thick for argon. As the separation of the ions and electrons induces a radial polarization field, it also creates a radial current. This radial current, although relatively small, interacts with the azimuthal field enough to cause the ion trajectories to deflect even more towards the cathode. In Region II, with the ions now moving slower and slightly deflected, *axial ion current* dominates with

ions recombining on the electrode surface to complete the total current. Burton suggested that this produces a $j_{iz} \times B_\theta$ that further decelerates the ions to sheet speed. Region II was also found to be the location of a large heavy species pressure gradient. As the radial electric field actually reverses sign (although not to the same magnitude) in Region II, the electrons actually try to drift against the current flow, however, with the greater ion density, collisions dominate and they remain relatively stationary with respect to the sheet. In Region III, the axial electric field is still negative, although smaller and returning to zero. As the ion density is low here, there is actually the possibility of a small reverse current being carried by the electrons in the trailing edge of the current sheet. The total sheet was found to be about 1 cm thick at the center line with a slight tilt, anode front leading cathode. At that time, no explanation was given for the tilt.

This tilt or cant of the current sheet has been investigated in more recent work at Princeton [52]. In brief, optical measurements of sheet speed and tilting angle have qualitatively found that larger molecular weight propellants experience more canting, and that the canting angle is independent of initial voltage or peak current. Research is continuing with Schlieren photography and a further discussion is presented in the next subsection.

1.8.3 Current Sheet Canting

From Lovberg's work and others it is clear that the molecular weight of the species plays an important role in determining the degree of canting. Using the same parallel-plate apparatus, Lovberg did not see canting with hydrogen, but did, in fact, see it using nitrogen and argon. Recent work at Princeton (Ref. [52]) has begun to study the degree of canting based on a parametric analysis of propellant species, gas density, and magnetic field (initial voltage and current) strength.

Other researchers who have observed canting include Keck at Avco-Everett who, like Lovberg, saw significant differences in magnetic probe data depending on the polarity of his coaxial accelerator using argon [58]. For the positive polarity, anode center, he noticed a 2 cm thick sheet that was tilted out along the anode. Although this result is to be expected from the stronger Lorentz force near the center electrode (regardless of polarity), he observed different behavior with reverse polarity. With the cathode as the center electrode, he noticed a very planar but thicker, 4 cm, current sheet that moved slightly *slower* than the positive polarity. In the same company, Fishman and Petschek tried to explain this phenomenon by combining the non-uniform Lorentz force and the assumption that the ions must carry a significant part of the current by recombination on the cathode [59]. In both polarity case, the non-uniform Lorentz force and potentially a precursor shock-wave were suspected to push some of the propellant towards the outer electrode. When the anode is the center electrode the ions are pushed toward the cathode which is considered the "normal" mode and the total current can be accounted for easily. If the center electrode is the cathode, however, now the ions are forced to move*away* from

the cathode. With insufficient electrode emission at the cathode, the ions must slowly diffuse to the cathode against the Lorentz force, potentially spreading out and slowing down the current sheet due to the higher plasma resistance. Fishman and Petschek's model also suggests that a relatively large amount of mass might be left behind near the outer electrode in a "bubble" where the current sheet has a smaller current density and is more permeable.

In yet another experiment, Liebing observed canting in a parallel plate accelerator using argon and a lumped transmission-line energy source [60]. Using streak cameras and magnetic field probes, Liebind found that the luminous front matched well with the current conduction zone and that the anode *always* led the cathode. He reversed polarity and found a similar result with evidence of an "anode foot" that was spread out with a lower current density than that observed at the cathode. A bright spot noticed near the cathode was suggested to be from radiation of plasma left behind the sheet. Finally, in another separate experiment using a ruby laser Schlieren system and a parallel-plate geometry, MacLelland noticed similar canting effects, although more pronounced with argon than hydrogen [61]. Still, even in the hydrogen discharges, the sheet eventually becomes canted with long enough electrodes and pulse duration. MacLelland also saw that, in a region near the cathode, the sheet was fairly planar and that an "anode foot" developed into the final canted structure.

With all of these researchers observing canting in pulsed accelerators, only two really tried to explain the reasons why it occurred in detail. In Ref. [62], Bostick examined a coaxial geometry and suggested that Hall currents combine with the normal, radial electron conduction current to give a total current deflected an angle. He also suggested that the current loops required for these near-axial Hall currents could be accounted for through the inclusion of "plasma vortices" within the current sheet that result from the sheer as the tilt develops. His evidence for such vortices was from the oscillating magnetic and axial electric field data he (as well as others he cited) had collected. In Ref. [63] Johansson, yet again at Avco-Everett, examined the current sheet tilt in an inverse z-pinch with hydrogen and argon at similar pressures. In this experiment, UV photo-detectors and magnetic field coils were used to measure the progression of the sheet. Like MacLelland, Johansson noticed an eventual canting in *both* hydrogen and argon discharges, although the tilt in hydrogen only occurred in a region near the anode. Near the cathode, the sheet was seen to be more planar with hydrogen, but the cant consumed the entire discharge in argon. At similar pressures, 100 mT (same H_2 and Ar number density), and using a separate high-voltage system to provide uniform initiation, Johansson saw that the tilt angle was similar between the two gases *as a function of radius* with the hydrogen discharge traveling almost twice as fast. In more extensive tests with argon at low pressures, he found that the trajectory of the center-of-mass of the sheet propagated as expected from a snowplow model. At higher pressures, the luminous region ran slightly ahead of the center-of-mass indicating a slightly permeable current sheet. The tilt angle as a function of radius (tilt angle increases slightly with radius) was similar at all the pressures although the current sheet was very diffuse at the highest pressures making it difficult

to quantify exactly. Johansson postulated that since the cathode could not be capable of producing the necessary electrons to conduct the total current, that ions must be the dominant current carriers near the cathode. He calculated the height (distance from the anode) where ions were assumed to carry *all* of the current as,

$$h_0 = \frac{1}{q}\sqrt{\frac{2M_w}{\mu_0 n}},\tag{1.19}$$

where q is the charge of the ion, M_w is the molecular weight, and n is the ambient fill number density. He found this estimation to be roughly correct compared to his own data, Lovberg's and others.

In all of these research projects it seems that ion conduction, molecular weight (gyro-radius), number density, and the lack of sufficient electron conduction from the cathode (possibly surface effects) are involved in the canting effect. Canting has been observed in parallel-plate, coaxial, z-pinch, and inverse z-pinch geometries with the anode always leading the cathode. Although it appears that many researchers are satisfied with their own explanation, a unified theory that yields the canting angle (or how to eliminate it altogether) as a function of accelerator design parameters such as electrode separation, propellant type, total current, etc. requires further, more detailed, investigation.

1.9   Acceleration Model Development

Researchers in almost every program studying pulsed plasma accelerators used an acceleration model (only the more detailed studies will be covered here) that consisted of an effective circuit equation representing the discharge elements, and a momentum equation that usually included a coupling term between the motion of the discharge and the effective driving circuit. It is this driving term that makes the typically one-dimensional equation set non-linear and impossible to solve analytically without making some severe approximations to uncouple the equations. In general, there are two classes of solutions, those using a constant mass (a "slug-mass" approximation) and those including the sweeping up of mass as the current sheet progresses. The earliest work which suggested that the current sheet acts like a "snowplow" can be found in Ref. [41] where Rosenbluth examined an infinitely thin sheet with no plasma resistance.

In one of the first papers on an acceleration model for plasma thrusters, Republic Aviation used a non-dimensional slug-model for the propellant eliminating any dynamic efficiency effects [30]. They also did not include any effects of plasma resistance, wall effects or radiation, although they did include a linearly distributed resistance for the electrodes. They tested two cases depending on integration time, however, they did not use a computer to solve the equations. The "long time" model used asymptotic analysis to integrate the circuit and momentum equations out to an effective infinite time later. As any solution to the these equations shows a damped current waveform, the current flowing through will be zero and the velocity will be constant at the end of the integra-

tion. Using this technique, the energy stored in the magnetic field and capacitor are also zero by the end of the integration. Along with the simple slug-mass assumption and without including the plasma resistance (instead, using a *constant* electrode resistance), this allows the equations to solved at t=∞. The solution given for the efficiency is,

$$\eta(t = \infty) = 1 - \frac{2}{1 + \sqrt{1 + EL'^2/2m_{bit}R_0^2}}, \tag{1.20}$$

where L' is the inductance-per-unit-length, E is the energy per pulse, m_bit is the slug-mass accelerated, and R_0 is the constant resistance of the electrodes. The "short time" model assumed that the sheet motion was weekly coupled to the external circuit, i.e. that the inductance was *constant*. This assumption makes the problem linear with separate, analytic solutions to the circuit and momentum equations. Again assuming a constant resistance,

$$\eta_{st} = \frac{1}{8}L'^2 \frac{E}{m_{bit}} \frac{1}{R_0^2} = \frac{1}{2\sqrt{2}} \frac{L'}{R_0} \bar{u}_e. \tag{1.21}$$

Including the effects of linear electrode resistance introduces a small correction and gives a cut-off for the initial inductance value where efficiency begins to decrease,

$$L_0 \leq \frac{R_0^2 C}{9}. \tag{1.22}$$

Otherwise, the initial inductance *does not* enter into the efficiency.

The non-dimensional slug model for acceleration presented in Ref. [30] is interesting in that it provides a resistance that varies as the current sheet moves down the electrodes, however, they found this to be a minimal effect. Their "short time" solutions do not include the effective resistance generated by the current sheet motion. Although this uncoupled model does not represent the electro-mechanical system correctly, it does provide a base for understanding the performance scaling. Their "long time" solution includes the effects of changing inductance, however, it does not include the effects of subsequent discharges typically found in accelerators with an oscillatory current. It also does not take into account the finite length of electrodes and corresponding maximum change in inductance for a given geometry. Still, with all of these assumptions in mind, it does produce an interesting scaling relation for a slug-like mass, Eq. 1.20, that with Eq. 1.21, shows a monotonic increase in efficiency with increases in inductance-per-unit-length and energy, and decreases in mass bit and external resistance.

In Ref. [28], Hart used a slug-mass circuit model that was solved using a computer and only at a few conditions. Although Hart recognized that the solutions could not be realized in the experimental accelerators with ambient fills, he thought that the results might apply reasonably well to pulse-injected systems. Hart showed, as expected, that not as much energy goes into internal modes of the plasma for slug-like distributions with a corresponding increase in

efficiency. Current waveforms predicted from this model were close to critically damped in character indicating a large rate of inductance change which, in reality, would require long electrodes. Hart also examined a constant mass distribution snowplow model and found very different waveforms depending on gas density. Hart also showed that a snowplow model could be modified slightly to account for the finite thickness of the current sheet although it did not significantly effect the results unless the thickness was on the same order as the thruster electrode length. In later work [29] Hart presented a modified snowplow model for coaxial accelerators with very small inner electrodes. The modified model was required to explain his experimental sheet velocity measurements, although a significant amount of unaccounted for Teflon insulator was probably the cause of the deviation from normal models.

Another slug-model developed at NASA Lewis and described in Ref. [37], actually included snowplow-like effect for mass that was eroded from the electrodes and accumulated as the current sheet progressed. As can be expected, the performance in this model strongly depended on a mass ablation coefficient that determined the ratio of ablated mass to injected propellant mass. The overall trends, however, showed a similar global result to other one-dimensional models with the highest predicted performance corresponding to large values of inductance-per-unit-length, initial voltage, capacitance and small values of initial inductance and resistance.

A more advanced, non-dimensional model developed later at Lewis and presented in Ref. [36] used a distributed propellant mass and included terms for ionization energy losses, radiation losses, wall drag due to ion diffusion, and heat transfer from the plasma to the electrodes through the inclusion of a plasma energy equation. The inclusion of the plasma energy equation included the following assumptions:

- The mass distribution function is not related to any physical phenomenon; that is, it does not have an exponential or linear nature that would be expected from pulsed gas injection or a uniform fill.

- Wall drag includes the loss in forward momentum from ions diffusing to the wall based solely on temperature and not current conduction.

- The internal energy of the plasma is based solely on temperature without including pressure effects. Energy is transferred to the plasma from the mass accumulation process and ohmic heating. Energy is lost from the plasma through heat conduction to the electrodes, electron current conduction, ion diffusion and recombination near the electrodes, ionization and radiation. It should be noted (by the author's own admission), however, that although ohmic heating, ionization, and radiation losses appear in the equations, they are not included in the actual solutions.

- The initial temperature is not specified explicitly in Ref. [36] and no profiles for plasma temperature are mentioned or displayed.

The effects of introducing the plasma energy equation are present in comparing the results of the more advanced model with one that does not include these losses, as shown in Figure 1.12. In general, the efficiency is found to follow a similar trend, peaking at a particular "Mass Loading Parameter" that is slightly smaller than what is predicted by the simplified model. The relative loss is smallest at small values of the Mass Loading Parameter. The Mass Loading Parameter is defined as,

$$\mathcal{M} \equiv \frac{2\ell m_0}{L'Q_0^2} = \frac{\ell m_0}{L'CE_0} \tag{1.23}$$

which includes the amount of mass in the initial discharge (m_0), the initial energy (E_0) or charge (Q_0) on the capacitor, the capacitance (C), the inductance-per-unit-length (L'), and the length of the electrodes (ℓ), but *not how the mass is distributed*. This definition makes it hard to differentiate between the various parameters, and its experimental value strongly depends on the initial mass taken up by the current sheet, a very difficult quantity to determine. The authors suggest that the largest loss is through ion diffusion to the walls and that radiation losses are negligible, although they do not provide magnitudes, relative or absolute. They also suggest that radiation cooling could play a significant role, although it is not included in the final plasma energy equation. Although the model did not seem to match well with experimental data, this could have been as much a result of trusting calorimetry performance data then the fault of the model. Without more information on the temperature profile as a function of time, it is hard to say if the plasma energy equation and the associated assumptions were reasonable. Finally, it should be noted that the advanced model did not take crow-baring into account and used a non-dimensionalization scheme based on the final inductance of the current sheet at the end of the electrodes. The integration was carried out until the current sheet reached the end of the electrodes.

The simplified model that did not include the plasma energy equation did, however examine the effects of crow-baring at a beneficial time when the current is zero (no energy is stored in the magnetic fields) and at the worst time when the current is maximum. In general, the effects of choosing an appropriate crow-barring time were more pronounced than those observed from the addition of the various loss mechanisms with up a 40% performance reduction predicted using the "maximum current" crow-bar time. Experimentally, the crow-bar time was seen to depend on accelerator geometry, especially near the breech. Later geometries included an "inhibitor ring" that delayed the crow-bar to when the total current was smaller. The performance measurements are presented in more detail in the section on work at NASA Lewis in Part I, however, in general, they did not match the predictions in either absolute values or functional form. The author's explain this discrepancy based mainly on the assumed initial mass density profiles.

Researchers in Italy followed almost the same exact non-dimensional scheme as Lewis' simplified model in their acceleration model studies [64]. Their model, however, also assumed infinite conductivity of the plasma and driving circuit

leaving the expanding current sheet as the only impedance. This assumption led to underdamped waveforms in almost every solution. A gaussian propellant distribution was also examined and produced a result similar to the mass-loading distribution used by Lewis. The research at Italy mainly contributed two things: 1.) As it was developed in 1972, computers were far enough along in their development to provide a large number of solutions for a wide range of parameters. 2.) A second, quasi-2D model examined the non-uniform Lorentz force in coaxial accelerators and found very different current sheet profiles depending on the *radial* propellant loading. This second model, however, did not make any correction for the canting effect noticed in many coaxial geometries and discussed previously.

At Princeton, Jahn included a comprehensive study of acceleration models in his book [1]. Pulling information from similar models in the literature, he used a non-dimensional approach based on the initial conditions for a parallel-plate accelerator. He examined the current waveforms and resulting current sheet trajectories for both slug and uniform propellant distributions. In a later non-dimensional model developed at Princeton, the effects of an expanding electrode geometry and an exponential mass distribution expected from kinetic theory were included along with the normal constant plasma resistance and snowplow models [45]. In the results from this model, tested over a wide range of parameters, the performance was seen to behave differently depending on the nature of the current waveform. In general, the efficiency increased with decreasing circuit resistance, however, for the underdamped cases with a uniform propellant fill, a maximum in the efficiency was found with a Dynamic Impedance Parameter, α, value near unity,

$$\alpha = \frac{L'^3 V_0^2 C^2}{18 L_0^2 m'},$$ (1.24)

where m' is the mass density gradient coefficient. For critically or overdamped cases with a uniform fill, the efficiency increased with $\alpha^{1/4}$ yielding,

$$\eta \propto \sqrt[4]{\frac{8 L'^3 V_0^2}{9 R_0^4 m'}},$$ (1.25)

with R_0 (including only the internal capacitor resistance and the plasma resistance) having the strongest influence. The thrust-to-power ratio *decreased* with increasing α for the underdamped cases and remained relatively constant over α for the critically or overdamped cases. Using an exponential mass distribution increased the efficiency and thrust-to-power ratio in accordance with the dynamic efficiency improving. The character of the efficiency was also changed for the underdamped case with the maximum point shifting to much higher values of α, > 10. Higher values of α, however, were also seen to require very long electrodes with total inductance changes on the order of $100 \times L_0$ which are very difficult to achieve in reality. The nature of the thrust-to-power ratio did not change for the exponential mass distribution. Using flared electrodes also improved performance, but not to the same extent as the non-uniform propel-

lant density. Further development of this model including crow-baring for the underdamped cases and finite-length electrode effects are ongoing at Princeton.

1.10 Estimates of Performance Scaling

This section differs from the previous section on acceleration models in that it specializes in how these acceleration models predict performance scaling. Many of the models mentioned earlier were not used explicitly to determine performance scaling, rather to check the trajectories of current sheets observed experimentally and determine the sweeping efficiency. Part of the reason why the early models did not search out more general trends is due to the lack of computer resources to examine a wide number of cases and develop trends. In addition, experimentally observed effects such as current sheet permeability as a function of the driving circuit and propellant loading were not included in the models. Simple estimates of performance based on both empirical data as well as simple acceleration models have paved the way for improvements in GFPPTs.

The first simple scaling relation came from the asymptotic solutions of a slug-model studied at Republic Aviation [30]. In that model, the efficiency was seen to scale as:

$$\eta(t = \infty) = 1 - \frac{2}{1 + \sqrt{1 + EL'^2/2m_{bit}R_0^2}}, \qquad (1.26)$$

where L' is the inductance-per-unit-length, E is the energy per pulse, $m_b it$ is the slug-mass accelerated, and R_0 is the constant resistance of the electrodes. In another "short time" model, it assumed that the sheet motion was weekly coupled to the external circuit, i.e. that the inductance was *constant*. This assumption makes the problem linear with separate, analytic solutions to the circuit and momentum equations. Again assuming a constant resistance,

$$\eta_{st} = \frac{1}{8}L'^2 \frac{E}{m_{bit}} \frac{1}{R_0^2} = \frac{1}{2\sqrt{2}} \frac{L'}{R_0} \bar{u}_e. \qquad (1.27)$$

Including the effects of linear electrode resistance introduces a small correction and gives a cut-off for the initial inductance value where efficiency begins to decrease,

$$L_0 \leq \frac{R_0^2 C}{9}. \qquad (1.28)$$

Otherwise, the initial inductance *does not* enter into their efficiency estimates. These results show a monotonic increase in efficiency with increases in inductance-per-unit-length and energy, and decreases in mass bit and external resistance.

In more recent work at Princeton, a similar, fixed element approximation [44] for performance scaling has been developed for coaxial and parallel-plate electrode geometries. In the fixed element solution, primarily modeling a critically damped waveform, the inductance was assumed not to change (although it was given an *average* value, $< L >$, greater than the initial inductance, L_0), and the

effective resistance was also held constant. The impulse was assumed to depend solely of the integral of the current squared with the final relation showing a linear dependence on the initial energy stored in the capacitor,

$$I_{bit} = L' \sqrt{\frac{C}{<L>}} E. \tag{1.29}$$

The efficiency was predicted as,

$$\eta = \frac{I_{bit}^2}{2m_{bit}E} = \frac{1}{2} L'^2 \frac{C}{<L>} \frac{E}{m_{bit}} = \frac{1}{2} L' \sqrt{\frac{C}{<L>}} \bar{u}_e. \tag{1.30}$$

Note that in this approximation, the average inductance quantity depends on the position of the current sheet and the inductance-per-unit-length. In this way, the efficiency could also be considered to depend on $\sqrt{L'}/\sqrt{\ell_{elect}}$. In any case, both the impulse bit (thrust-to-power ratio) and the efficiency are expected to scale with a square-root of capacitance. A similar relation can be found in Ref. [65].

In a more complicated snowplow model for a z-pinch at Princeton [40], the model results were put together with experimental data to find that, when the sweeping efficiency was high, the sheet velocity was seen to scale with the non-dimensional "magnetic interaction parameter" β,

$$\beta \equiv -\frac{\mu_0 Q_0^2}{4\pi^2 \rho_0 r_0^4} = -\frac{\mu_0}{2\pi} \frac{h}{r_0^2} \frac{CE}{m_{bit}}, \tag{1.31}$$

where ρ_0 is the initial density, r_0 is the outer electrode radius, and h is the distance between the electrodes. Various values of the β parameter were investigated using different mass densities and outer electrode radii. The pinching effect was also found to be a strong function of β with the pinch occurring *before* the current reversal for $|\beta| > 0.2$.

In another, non-dimensional model including the effects of a flared electrode geometry and an exponential mass distribution [45], the performance was seen to behave differently depending on the nature of the current waveform. In general, the efficiency increased with decreasing circuit resistance, however, for the underdamped cases with a uniform propellant fill, a maximum in the efficiency was found with a Dynamic Impedance Parameter, α, value near unity,

$$\alpha = \frac{L'^3 V_0^2 C^2}{18 L_0^2 m'}, \tag{1.32}$$

where m' is the mass density gradient coefficient. For critically or overdamped cases with a uniform fill, the efficiency increased with $\alpha^{1/4}$ yielding,

$$\eta \propto \sqrt[4]{\frac{8 L'^3 V_0^2}{9 R_0^4 m'}}, \tag{1.33}$$

with R_0 (including only the internal capacitor resistance and the plasma resistance) having the strongest influence.

In the non-dimensional model developed at NASA Lewis [36] and used again at the University of Pisa [64], the optimal performance over many operational parameters occurred when the Mass Loading Parameter was near unity. The Mass Loading Parameter is defined as,

$$\mathcal{M} \equiv \frac{2\ell m_0}{L' Q_0^2} = \frac{\ell m_0}{L' C E_0} \tag{1.34}$$

which includes the amount of mass in the initial discharge (m_0), the initial energy (E_0) or charge (Q_0) on the capacitor, the capacitance (C), the inductance-per-unit-length (L'), and the length of the electrodes (ℓ), but *not how the mass is distributed*. This definition makes it hard to differentiate between the various parameters, and its experimental value strongly depends on the initial mass taken up by the current sheet, a very difficult quantity to determine.

In experimental performance scaling experiments, it is interesting to note that thrusters with current rise rates per unit width of less than $10^{12} A/(m \cdot s)$ have empirically been shown to have less than 100% sweeping efficiency [1, 40]. In the case of Lovberg's experiments where he found mixed results [7, 14], this criteria holds true: the parallel-plate accelerator has a width of 8 cm and a current rise rate of 250e9 A/s giving about 3e12 A/ms while the coaxial geometry has an average width of 22.6 cm and a current rise rate of 160e9 A/s giving about 0.7e12 A/ms. In accordance with the rule of thumb, the parallel-plate thruster showed behavior like a snowplow while the coaxial geometry did not. In another coaxial geometry tested later at GD [11], a higher capacitance and smaller average radius electrodes reached up to 1.4e12 A/ms [11]. Although the authors did not expressly try to match or exceed this criteria at the time, probe data confirmed that the current sheet was indeed acting like a snowplow in this later, coaxial device. This rule of thumb applies well to almost any geometry as demonstrated in other experiments as well, frequently without the authors realizing that they did meet the criteria [19, 35, 63]. It is also interesting to note that in many experiments where the sheet was classified *not* to be an effective sweeper [7, 28, 39], the sheet velocity scaled as the *square-root* of the energy to mass ratio as apposed to an expected linear scaling as predicted for effectively sweeping sheets [14, 31, 40, 63]. In Ref. [54], Guman showed with a relatively simple model that the square-root scaling would be expected for an electrothermal acceleration mechanism. The linear relation is expected for electromagnetic acceleration as shown in Eq. 1.30.

Many experimental performance scaling studies have been completed in GF-PPT research, although, unfortunately, many of them have not been controlled experiments. That is to say that instead of varying only one parameter (capacitance, for example) at a time, most researchers enact many changes at once, sometimes without even realizing it. Therefore, any conclusions they make about their modifications cannot be attributed to a specific change in one parameter and the specific scaling relation is unclear.

At General Electric, following many, multi-parameter modifications [20], the efficiency was shown to be linear with exhaust velocity over a wide range of mass bits (smaller mass bits gave higher efficiency) with a relatively constant

thrust-to-power ratio near 20 μN/W at similar capacitance and discharge energy levels [21]. GE also conducted a performance survey over five different capacitance values from 50 to 200 μF to find that the performance scaled with the square-root of the capacitance to within 5-10% [23]. As discussed in the sections on research at GE and GD in Part I, however, GE's performance measurements have the possibility of including facility background-contamination. This may add doubt to their *absolute* performance measurements, but perhaps their *scaling* trends are more acceptable.

Hart may have been the first one to realize that a solid-propellant Teflon thruster could have space-flight applications (see footnote in Ref. [29]. Although he tested a variety of geometries, capacitance, inductance, and mass bit values, unfortunately all of his experiments were influenced by the ablation of a significant amount of Teflon from the backplate. With gas propellant mass bits between 10 and 500 μg and discharge energy levels being a 1 kJ or higher, The majority of the discharge could easily have been made up of Teflon at the lowest, middle, and even highest mass bits for the small inner electrodes. Although his computation models are valid (except possibly the modified form of the snowplow model), the results from streak photos that do not distinguish the radial position of the current sheet do not provide an adequate comparison or verification of the models. The "Mode II" operation showing the fastest sheet speed is probably a result of a canted current sheet leading down the center electrode (anode) much faster than the true plasma center-of-mass.

At Princeton, the performance of a low-energy, high-rep-rate GFPPT was studied parametrically. Two energy levels for each of two capacitance values were tested over ten different mass bit values each yielding a 40-point GFPPT performance database. Four graphs which show PT5 performance as a function of mass bit and specific impulse with the capacitance and the initial stored energy level as parameters are shown with error bars in Fig. 2.11. Each point represents at least twenty trials including separate measurements of impulse, mass bit, and energy at the same conditions. Values of the performance data are given at the end of this section in Table 1.9. It is evident from all the plots in Fig. 2.11 that for each curve there is a transition with decreasing mass bit (or increasing I_{sp}) from a mode (Mode I) where the efficiency and the impulse are respectively independent and dependent on the mass bit (and where the efficiency the thrust to power ratio are respectively independent and dependent on I_{sp}) to another mode (Mode II) where the converse statements hold.

Simple analytic models presented in the previous section show that the efficiency and thrust-to-power ratio should scale with the square-root of capacitance and not depend on the energy (at a constant exhaust velocity) for an electromagnetic accelerator. These trends are evident in Mode II where the efficiency increases linearly with the specific impulse and the thrust-to-power ratio is relatively constant.

It is interesting to note that the performance scaling suggested for a thruster where electrothermal acceleration is dominant are quite different (again, see Ref. [54]). In that case, the impulse bit is expected to scale with the square root of the discharge energy to mass bit ratio and not depend directly on capacitance

or inductance change. In addition, the efficiency of a pure electrothermal accelerator is expected to be constant over wide range of specific impulse, energy and mass bit values. While the efficiency as seen in panels c and d of Fig. 2.11 is indeed independent of mass bit and I_{sp} at high mass bit values (i.e. Mode I), it does show a dependence on energy, albeit a weaker one than for Mode II. This tends to indicate that the acceleration in Mode I may be due to a combination of both electrothermal and electromagnetic effects. Again, as the losses associated with sweeping up the propellant are not accounted for in these predictions, an explanation for trends in Mode I could be a function of improved dynamic efficiency as well.

In general, all the models and experimental evidence points to using high-voltage, high-capacitance, high-inductance-per-unit-length, low mass discharges with a minimum of parasitic inductance or resistance and short electrodes. Current sheet permeability, propellant utilization efficiency, and the potential problems of crow-bar discharges are important to consider when designing the driving circuit as well. Discharge symmetry, and the resulting decrease in performance from asymmetric discharges, are a result of proper discharge initiation.

1.11   Experimental Performance Measurements

Again, many of the experimental performance measurements have been presented before, however they will be repeated here to some extent. The measurements are divided according to research laboratory and the results are sometimes shown graphically or with tables in Part I. More details on specific geometries or the progression of GFPPT design at each laboratory can be found in Part I.

1.11.1   Summary of GD Performance Measurements

The measurements presented here were performed during the later stages of GFPPT development at General Dynamics [17] using a thrust stand (pulsed operation at 10 Hz gave effective "steady" measurement and average impulse bit) and an appropriately conditioned thruster to eliminate contamination effects. The capacitance was increased to a final value of 140 μF with a distributed inductance giving nearly a square current pulse. The geometry of this thruster was slightly different than that of Figure 1.1. The length of the center electrode was shorter (5.5 cm) with the same radius (1.9 cm) while the outer electrode was about the same length (15.8 cm) but had a larger radius (6.25 cm). The new radius ratio was about 3.3. The propellant was injected radially at the breech with the discharge initiation timing controlled by a gas-discharge switch. Propellant utilization was measured to be just over 60% with nitrogen and a 350 μs delay. The mass bit was controlled by changing the feed pressure and the quantity was determined by integrating measured density profiles. Both nitrogen and xenon data were used in this study as shown in Tables 1.1 and 1.2 and Figures 1.3 and 1.4. In general, the efficiency varied from 6 to 56%, the specific impulse varied from 350 to 13,000 s, and the thrust-to-power ratio varied from

33.5 to 8.7 μN/W, respectively, depending mass bit and energy. As expected, the highest efficiencies corresponded to the highest energy and lowest mass bit values, however, the thrust-to-power ratio is highest at the *lowest* energy and highest mass bit values.

Thrust stand data was also obtained using a GFPPT very similar in design to General Electric's A-7D GFPPT with axial propellant flow (xenon) and a separate high-voltage discharge initiation system. GE's mass injection scheme was duplicated very closely to insure the same propellant utilization ($> 90\%$) and density profiles. While faraday cup measurements of ion velocity and exhaust beam divergence were very similar to those obtained at GE (see next section), thrust stand and performance measurement data disagreed with significantly lower values measured at General Dynamics [17]. Table 1.3 shows performance values at four energy levels. For this device, the efficiency is relatively constant at a fixed energy while the thrust-to-power ratio still shows a tendency to decrease with increasing energy and decreasing mass bit.

1.11.2 Summary of GE Performance Measurements

The measurements provided in Table 1.6 and Figures 1.6 and 1.7 represent thrust-stand measurements from GE's A-7D model using xenon propellant and a 144.5 μF capacitor bank with a Q-factor of 14. Unfortunately, only energy (with Q-factor reduction), specific impulse, and efficiency were given in Ref. [23] where all of this data is reported in graphic form. This is, however, the best source for pure data as GE did not frequently show many points in a data set or any tabular information. The mass bit and impulse bit values must, therefore, be inferred from the reported specific impulse, voltage, and efficiency measurements,

$$I_{bit}^* = \frac{2\eta}{I_{sp}g_0} \frac{1}{2} C V_0^2 \left(1 - \frac{1}{Q}\right), \qquad (1.35)$$

$$m_{bit}^* = \frac{I_{bit}^*}{I_{sp}g_0}, \qquad (1.36)$$

where the star superscript indicates the inferred quantities. Finally, it must be noted that out of every lab conducting GFPPT performance measurements on thrust stands [4, 5, 17], GE is the *only* one that did not report any decrease in measured thrust or impulse over the first 100-1000 pulses, including tests at similar mass bits and energies. As GE's protocol for measuring thrust is not published explicitly, it is unclear if any preconditioning of the thruster took place before the measurement.

Unfortunately, the researchers at GE did not mention any impulse decay effects that have been observed at three other laboratories testing the performance of GFPPTs on thrust-stands in diffusion pumped chambers [4, 5, 17]. Although researchers at GE did not notice any performance changes from changing the pulse frequency, details of the this experiment were not given. Rather than pulse *rate*, the total number of pulses has been shown to be more important in conditioning the thruster for proper operation. Without such conditioning,

adsorbed gases from the electrode surfaces and organic-monolayers from the roughing and diffusion pumps can significantly alter *both* the amount of mass in the discharge and the electrical conduction of the plasma near the electrode surface. Although these effects could be beneficial, true performance as would be expected in space operation can only be measured after a conditioning period and as long as pump oil is not allowed to migrate to the thruster electrodes.

Three other pieces of evidence suggest that the performance measured at GE might include contamination effects:

1. GE's vacuum chamber used three 32" diffusion pumps that did not have baffles of any kind to prevent back-streaming. The closest pump was less than one meter away from the thrust stand [19].

2. Gridded ion velocity measurements taken by researchers at GE showed a significant amount of carbon and oxygen ions that varied from pulse-to-pulse. Although the total mass of these atoms may not have been significant compared to the xenon ions, their source and their effect on the current sheet structure remains unknown [27].

3. General Dynamics constructed a very similar thruster to that of GE's A-7D and found, at best, a factor of two *smaller* performance [17].

The last item can best be visualized graphically with the results from Tables 1.3 and 1.6 being plotted in Figure 1.8. From this graph, it is easy to see that the data measured at General Dynamics has significantly lower performance than that measured at General Electric. It should be noted that General Dynamics and General Electric were competitors, however, only General Dynamics took the effects of background contaminants into account [17]. After 1970, there are no more publications from GE on GFPPTs, however, research at GE began on ablative pulsed plasma thrusters in the late 1960's.

1.11.3 Summary of Republic Performance Measurements

Unfortunately, the experimental work with the z-pinch, coaxial hybrid thruster never produced an efficiency calculation in the journal publications. They were suggested to be below 50% from calculations of the amount of energy going into the internal losses of the capacitors [32]. Velocity measurements from probes do not necessarily correspond to the mass averaged exhaust velocity as the sweeping efficiency of the sheet may not be 100%. For this thruster geometry, probably the most difficult thing to calculate was the mass bit which could explain the lack of efficiency data. In the summary produced by NASA Lewis [2], efficiencies were shown to be around 14% at 3,000 s (9.5 μN/W) with nitrogen although the exact configuration of the thruster is unclear compared to the journal publications. In his last paper, Guman did measure the thrust-to-power ratio (without specific impulse) and found that it asymptotes to about 9 μN/W at small mass loadings (previously tested conditions) and reached almost an order of magnitude higher, 80 μN/W at higher mass distributions. This was,

by far, the largest thrust-to-power ratio measured for any GFPPT at the time, although the efficiency and specific impulse at this condition were probably very low. Still, the lack of continuing research on them at Republic after this measurement is puzzling, although Guman did begin ablative pulsed plasma thruster research soon afterwards.

1.11.4 Summary of NASA Lewis Performance Measurements

Researchers at NASA Lewis measured the performance (calorimetry) of four different accelerator designs, as shown in Table 1.8 and taken from Ref. [36]. The thruster was conditioned by firing ten times prior to any measurement. All the designs used mainly argon for propellant and an ignitron switch for discharge initiation timing. The propellant utilization for these devices was estimated to be 100% due to the short valve times (0.1 ms) and long barrels. The accelerators were all backed by a 12.1 μF capacitor bank that could be charged up to as much as 30 kV. Reduction in parasitic inductance came from improving the connection between the capacitor bank and accelerator as well as modifications to the gun geometry itself. Even with changes in propellant injection location, initial inductance, and inductance-per-unit-length, no noticeable difference in performance was measured until the electrode length was reduced by slightly more than 50%. Unfortunately, the inductance-per-unit-length was also changed in this configuration making the correlation with the stronger Lorentz force or reduced wall losses difficult to differentiate.

Probably the two biggest contributions from NASA Lewis are the most inclusive acceleration model published from any of the labs [36] and the review of GFPPT research in 1965 [2]. Performance measurements at Lewis did not include thrust-stand data, although the thruster was pre-conditioned to eliminate electrode contamination. In addition, although changes were made in thruster geometry, propellant distribution, and energy, they were not systematically tested so correlation between the modifications and performance improvements could only be speculated. Finally, with only a few mass bit values tested and no amount of error reported, the trends presented in the data are difficult to distinguish.

1.11.5 Summary of Princeton Performance Measurements

To date, nine generations of SRL-EPPDyL GFPPTs have been tested with many modifications on each generation. Using a low-voltage (250 V), low-inductance (< 5 nH) capacitor bank (45-270 μF, 1.4-8.4 J), these GFPPTs have close to critically-damped current waveforms with no noticeable crow-baring. Peak currents are close to 10 kA with pulses lasting about 5 μs. As shown schematically in Figure 2.1, during a burst the valve is only cycled once, therefore, the ultrafast, high energy valves used in previous GFPPT designs are not required. As the propellant flows at a constant rate, the propellant utilization is dictated by the pulse frequency and the thermal velocity of the propellant. For example,

using argon ($v_{th} \approx 400$ m/s) and a 4 kHz pulse frequency, the electrodes are required to be at least 10 cm long to ensure that none of the propellant escapes outside of the discharge volume between pulses.

Although many different GFPPT designs have been tested at EPPDyL, the fifth-generation (designated as PT5) has undergone the most extensive performance measurements. Since its original design, changes have been made to its discharge initiation system and propellant distribution [10] as well as the performance measurement technique to insure proper conditioning [5]. As shown in Fig. 2.2, PT5 uses a stainless-steel, coaxial electrode set with an outer to inner electrode radius ratio of approximately four and a total volume of 350 cm^3. It uses four semi-conductor type surface-flashover spark plugs mounted on the inside of the outer electrode (cathode) at 90 degree azimuthal intervals to initiate the discharge uniformly. The main discharge is driven by a low-inductance (10 nH) 130 or 270 μF capacitor bank which is capable of being charged to 250 V giving a maximum energy per pulse of 4 or 8 J, respectively. The entire thruster has a mass of approximately 6 or 8 kg depending on the capacitance level and including the electrode mass as well as the thruster housing mass. High-speed photographs of the discharge were taken with an Imacon Fast-Framing Camera (IFFT) at rates of 500,000 frames per second. A series of IFFT frames of PT5 showing the symmetrical discharge initiation are presented in Fig. 2.5. Before the modifications to the gas manifold were made to make propellant injection more uniform, the discharge initiation was seen to occur near the region of highest pressure. This is a similar result to those researchers who found spoking instabilities when the discharge was allowed to initiate based solely on a Paschen breakdown without an external switch.

Two energy levels for each of two capacitance values were tested over ten different mass bit values each yielding a 40-point GFPPT performance database. Four graphs which show PT5 performance as a function of mass bit and specific impulse with the capacitance and the initial stored energy level as parameters are shown with error bars in Fig. 2.11. Tables of the performance data are given at the end of this section. It is evident from all the plots in Fig. 2.11 that for each curve there is a transition with decreasing mass bit (or increasing I_{sp}) from a mode (Mode I) where the efficiency and the impulse are respectively independent and dependent on the mass bit (and where the efficiency the thrust to power ratio are respectively independent and dependent on I_{sp}) to another mode (Mode II) where the converse statements hold. More performance measurements with changing inductance-per-unit-length are ongoing at Princeton.

Part III

Summary

1.12 Progression of GFPPT Designs

Gas-Fed Pulsed Plasma Thrusters have been developed in many laboratories over many years. Originally developing from the magnetic shock tubes [66, 67] and applications to fusion research [6], the first plasma guns of many laboratories (see Refs. [8, 19, 28, 35] had long, coaxial electrodes with small radius ratios and propellant injection near the middle of the electrode volume. Typically these first GFPPTs were also operated at high energy ($>$ 1 kJ) and low capacitance ($\approx 10\mu$F) with the Paschen break-down controlling the discharge initiation. Many of the designs had relatively large amounts of parasitic inductance ($\approx$ 100 nH) and lightly damped oscillatory current waveforms where the dynamics of the discharge were dominated by subsequent crow-baring. As the designs progressed, radius ratios were more than doubled, the electrodes were shortened by almost a factor of four, the driving capacitance was increased by an order of magnitude the parasitic inductance and resistance were reduced as much as possible, and average energy was reduced to below 100 J. Some of these later devices did not exhibit crowbarring with near critically damped current waveforms while others timed the crowbar (current reversal) to coincide with the discharge reaching the end of the electrodes so that no energy stored in magnetic fields was wasted. High speed, high voltage valves were introduced from improved propellant utilization, close to 100% in many designs. The discharge initiation process was also controlled with either a high current, low inductance gas discharge switch or high-voltage spark triggers. Efficiencies of these devices were greater than 20 % at specific impulse values near 4000 s with thrust-to-power ratios close to 10 μN/W.

The progress was best summed up in 1965 where researchers at Lewis outside of the experimental group produced a comprehensive review of GFPPT research [2]. It gave the following list of important lessons learned to date:

1. Calorimetry data from many labs did not agree with the subsequent performance data measured on thrust-stands. Thrust-stand data was generally accepted as the most accurate way to measure performance.

2. Crow-baring generally occurs in all unsteady devices sometime between the voltage and current reversal points depending on thruster geometry and driving circuit parameters.

3. The main acceleration mechanism inside the current sheet was believed to be primarily due to the polarization field created by the electrons trapped on an $E \times B$ drift and the subsequent charge separation. The report also mentioned, however, that many of the labs had very different results and disagreed in this area, especially on the influence and existence of ion conduction.

4. The coaxial geometry (compared to pinch or parallel-plate) was suggested to be the best because it trapped all of the electromagnetic fields although it has a large electrode surface area and small inductance-per-unit length which decreased efficiency.

5. Including an electric switch in the discharge initiation process (as apposed to using the Paschen break-down point alone) led to better repeatability, fewer spoking instabilities, and improved propellant utilization while, at the same time, it introduced parasitic inductance and resistance as well as adding reliability questions.

6. Stated the need for a simple performance model that was confirmed by repetitive experimental performance measurements.

7. Stated that the only thing keeping GFPPTs from being used in space was their lack of "heat handling capability" and that research was shifting to quasi-steady devices which might have better performance.

Unfortunately, GFPPT research began to fade soon after this report. The two main problems were the lifetime and performance issues associated with the ultra-fast, high energy solenoid valves as well as relatively low performance and large system mass compared to other electric propulsion systems being developed at the same time (ion thrusters for example) for main propulsion. Research at General Dynamics, NASA Lewis, and Princeton shifted to quasi-steady gas fed devices where discharge times were increased and the current sheet was allowed to stabilize near the end of the electrodes. These devices did not require the fast valves of the past and showed promisingly better overall performance with the ability to process many mega-watts of power in relatively small device. At the same time, as these devices are pulsed, they share the advantage of arbitrarily lower steady-state power consumption. Still, system mass was large and this type of device did not experience in-space testing until recently with the flight of the Japanese Space-Flier Unit. Research at General Electric and Republic aviation shifted to ablative pulsed plasma thrusters that used much lower energy and were geared more towards attitude control applications. Some of these US developed devices flew in space as early as the 1970's on a Navy satellite.

Recently at Princeton, GFPPTs have resurfaced as a higher efficiency alternative to APPTs for attitude control applications, low-power deep space missions, and missions where a unique propellant requirement or contamination issues are important. These GFPPTs operate at much lower energies than their predecessors and have similar, although slightly lower, performance. The fast acting valves have been replaced by using modern, solid-state pulse-forming technology that allows > 4 kHz pulse rates and steady mass flow during the burst of pulses. The performance scaling of the devices has been measured over a wide range of operational parameters, and two modes of operation depending on propellant distribution, have been observed. The first mode has a high thrust-to-power ratio and relatively low efficiency while the second mode has a relatively high efficiency and low thrust-to-power ratio. These thrusters are now under consideration for various space missions.

1.13 Future of GFPPT Research

The future of GFPPT research still lies in the general category of improving performance. Although the modern, low energy devices have achieved similar performance to the older, higher-energy devices while requiring much less massive systems, there are still areas where performance can be improved:

1. Understanding the permeability and canting of the current sheet as a function of various operational parameters and, possibly controlling them.

2. Creating a more uniform, reliable discharge initiation system that reduces erosion rates.

3. Developing ways of further reducing parasitic inductance and resistance or improving plasma conductivity especially at low energy.

4. Using higher inductance-per-unit-length electrode geometries, possibly with externally applied fields.

5. Testing the devices in space examining potential contamination, performance, waste-heat processing, and EMI effects.

Chapter 2

Is the Gas-Fed PPT an Electromagnetic Accelerator?

2.1 Introduction

The question of whether the dominant acceleration mechanism in pulsed plasma thrusters (PPTs) is electromagnetic or electrothermal is of current interest[65, 68] and is important not only due to its fundamental value but also due to its implications on improving propulsive performance and clarifying how to properly scale these devices to higher or lower discharge energies.

The goal of this study is twofold: 1) present a performance database measured with a modern GFPPT operating over a wide range of mass bits, energy levels, and driving capacitance values and 2) use the measured performance trends to investigate the question about the nature of the acceleration. The goal is *not* to present the best performance data that can be attained with a given thruster.

Although the dominant acceleration mechanism of ablative pulsed plasma thrusters (APPTs) may still be under debate, trends in this database as discussed in this chapter indicate that for a typical *gas-fed* PPT, the performance can be easily be made to transition to a mode where the trends follow the expected scaling of electromagnetic acceleration.

Previous performance measurements at EPPDyL[53, 44] as well as Fairchild Republic[4] in 1966 have been shown to be influenced by diffusion pump oil contamination. A thin oil-film is believed to build up on the thruster electrodes between impulse measurements and influence the discharge dynamics due to the small mass bit nature ($< 2\mu$g per pulse) of GFPPT operation. Steps have been taken at EPPDyL to eliminate this problem including modifying existing baffles to accept liquid nitrogen cooling and develop a protocol for thruster

decontamination and conditioning.

This chapter begins by describing the current GFPPT system (PT5) studied in this database and improvements to the discharge initiation circuitry to insure a reliable, symmetric, and simultaneous break-down at the start of the GFPPT discharge. The next section describes the issue of diffusion pump oil contamination, a comparison of the performance measurements taken at EPPDyL's recently renovated facility with impulse measurements taken at a cryo-pumped facility at NASA JPL, and an outline of a new procedure for eliminating contamination effects from performance measurements. The performance measurement technique used for this database is detailed along with an error analysis of measured parameters. Finally, The results of the database are presented with a discussion of trends and a comparison of the data set to a simple electromagnetic acceleration model.

2.2   The PT5 GFPPT

A detailed description of the SRL family of GFPPTs has been given in other papers[53, 44, 10] and will only be summarized here. A steady-state power supply charges the PPT capacitor bank which is discharged at a finite duty cycle between two co-axial electrodes where gas has been injected just before the pulse (see Fig. 2.2). If the gas discharge initiation is uniform, a disk-like current sheet forms and is accelerated due to the Lorentz force created by the current flowing through the sheet and the self-induced magnetic field. The plasma current sheet acts like a piston or snow-plow on the gas in front of it and exhausts the gas at a velocity of a few tens of km/s. Typical operational parameters for one pulse include charging voltages close to 250 V, peak discharge currents on the order of 10 kA, and discharge durations of less than 10 μs. During the pulse, instantaneous power is close to a megawatt, however, the duration is short enough that only 1-10 J of stored energy is necessary for each pulse.

Until recently GFPPTs suffered from low propellant utilization efficiency due to the fact that the fastest available space-qualified gas valve with long enough life ($> 10^7$ pulses) has an open time not shorter than 1 ms. As the time to fill the discharge chamber is only the on the order of 100 μs, much of the propellant could not utilized effectively over the life of the device. Recent work has resulted in a complete solution[53] to this problem by using state-of-the-art pulse power technology raising the propellant utilization efficiency to well above 90%. This solution is illustrated in Fig. 2.1 and relies on using modern pulsed-power conditioning technology to adjust the period τ_p between pulses to a length very close to the time it takes for the cold injected gas to fill the thruster chamber. This typically corresponds to pulse frequencies of a few kHz during the burst. Depending on the available bus power and mission requirements, sets of such pulses can be produced such that each lasts a period τ_p that is at least as long as the response of a space-qualified valve (e.g. 1 ms) thus making sure that practically all injected propellant is utilized. A typical voltage and mass flow rate history of multiple pulses is shown in Fig. 2.1.
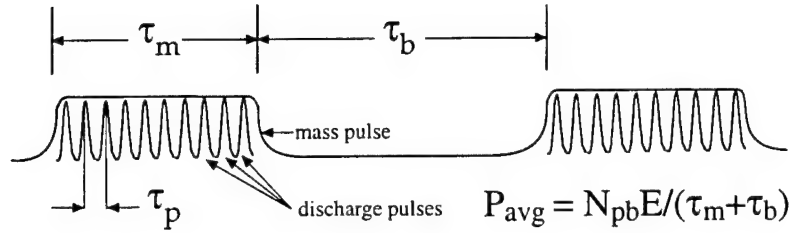
Figure 2.1: Schematic of a burst of pulses.

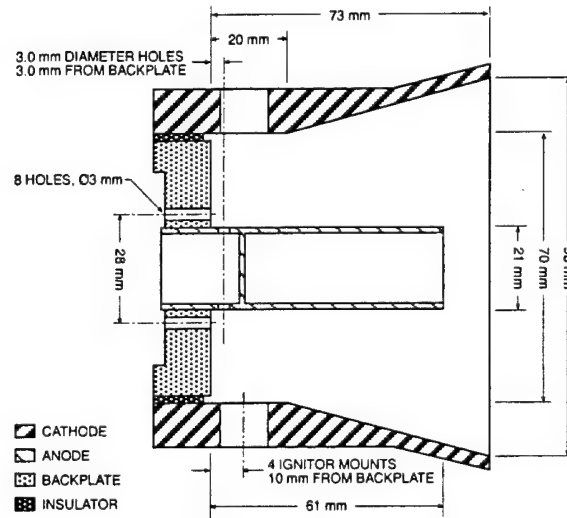$$P_{avg} = N_{pb}E/(\tau_m+\tau_b)$$

Figure 2.2: Schematic of PPT5.

The fifth-generation SRL-GFPPT used in the present study is designated as PT5 and has undergone five additional modifications since its original design including changes to its discharge initiation system and propellant distribution[10]. A schematic of PT5 is shown in Fig. 2.2. The PT5 has a relatively large, stainless-steel co-axial set of electrodes with an outer to inner electrode radius ratio of approximately four and a total volume of 350 cm^3. It uses four semi-conductor type spark plugs mounted on the inside of the outer electrode (cathode) at 90 degree azimuthal intervals to initiate the discharge uniformly. The main discharge is driven by a low-inductance ($<$ 10 nH) 130 or 270 μF capacitor bank which is capable of being charged to 250 V giving a maximum energy per pulse of 4 or 8 J, respectively. The entire thruster has a mass of approximately 6 or 8 kg depending on the capacitance level and including the electrode mass as well as the thruster housing mass. The latest modification involves a new discharge initiation circuit that provides reliable, simultaneous

activation of all four spark plugs at the beginning of the discharge as described in the next section.

2.2.1 New Parallel Discharge Initiation Circuit

The design of the discharge initiation (DI) system for co-axial geometry GF-PPTs has undergone many revisions at EPPDyL to improve repeatablity, spark plug lifetime, and discharge symmetry. In the last iteration, the same Bendix semi-conductor type spark plugs used in the LES8/9 ablative pulsed plasma thruster (APPT) were adopted for their low break-down voltage characteristics [69] and demonstrated long-lifetime. Firing four or more spark plugs *simultaneously* to create a uniform and symmetric discharge, however, was found not to be a trivial task. Discharge asymmetry due to one or more spark plugs not firing at all was shown by fast-framing camera images of co-axial GFPPT discharges over many different operating conditions [10]. In addition, as described in Section 2.3.3, performance measurements conducted at NASA JPL showed that the impulse bit was reduced by as much as 40% when only one spark plug fired instead of four.

To correct this problem, the spark plugs were removed from the outer electrode of the PT5 and an entirely new discharge initiation system was designed and tested in a small high-vacuum facility which allowed for quick modifications. First, the ignition characteristics of one spark plug were tested over a wide range of background argon pressures (0.1-10 millitorr) and applied voltages (200-1000 V) using a 0.2 μF capacitor on the primary side of a 10x pulse transformer. The breakdown condition of this type of spark plug was found to be a strong function of the time derivative of the voltage, the absolute magnitude of the applied voltage, and the internal resistance of the spark plug. Breakdown was found to be a weak function of argon pressure although the argon in these tests was supplied as a background gas and did not directly impinge on the spark plugs as it does in the PT5 configuration. Minimal breakdown conditions for a typical spark plug at 1 millitorr of argon were found to include a dV/dt $> 400V/\mu s$ and an absolute voltage greater than 250 V as shown in a sample voltage trace of four spark plugs in Fig. 2.3.

As the spark plug testing continued, the internal resistance of each spark plug changed over a wide range of values between 200 and 2000 Ω generally increasing with the number of pulses fired although not monotonically. The breakdown voltage characteristics increased with increasing internal resistance leading to a slightly higher requirement for the dV/dt and absolute voltage magnitude in order for all the spark plugs to break down regardless of internal resistance. Once this was determined, a DI circuit that could produce the necessary voltage characteristics to all four spark plugs connected in parallel (common cathode) was designed and tested.

Following a similar design to the Fairchild DI circuit in the LES8/9 APPT, the secondary side of the original pulse transformer was modified to include a high-voltage, 20 nF mylar capacitor in parallel with the spark plug. In addition, a high-current, fast-switching diode (International Rectifier part HFA15TB60)
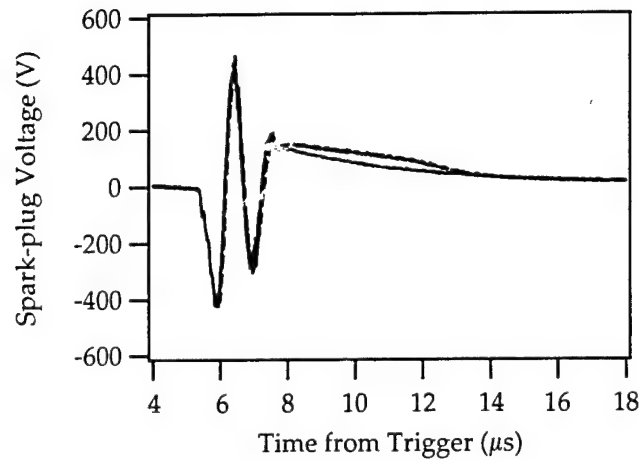
Figure 2.3: Voltage on all four spark plugs during discharge.

and 10 Ω resistor in series with the spark plug were used to insure that each capacitor did not lose its charge to another spark plug already in the process of breaking down. This is important as the first spark plug to fire provides the lowest impedance path that can drain the other spark plugs' capacitors before they have had the chance to fire. A schematic of the new DI circuit is shown in Fig. 2.4.

2.2.2 Discharge Initiation Symmetry

The new DI circuitry was installed on PT5 and the thruster was tested under a variety of operating conditions including changes to the DI primary capacitor
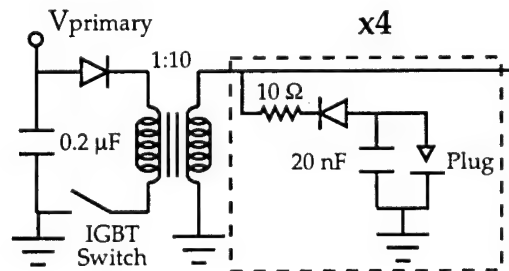

Figure 2.4: Schematic of the new discharge initiation circuit. The portion of the circuit surrounded by the dashed box is repeated four times in parallel, one for each spark-plug.
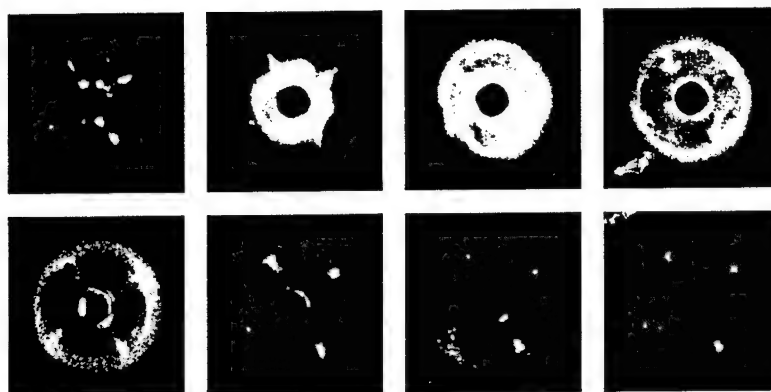
Figure 2.5: Imacon Fast-Framing Camera photos of a typical PT5 discharge looking head on into the discharge chamber at 0.5 μg per pulse at 4 J of energy. The photos seen here are spaced by 1 μs going from right to left.

voltage. The DI circuit was found to operate most effectively and repeatably with a primary capacitor voltage of 500 V. Although initiation at higher voltages worked equally well, the primary capacitor voltage was kept at a minimum to reduce the energy added to the discharge by the spark plugs and to reduce the possible erosion of the spark plug material due to higher current operation. Impulse was measured as a function of primary capacitor voltage and did not noticeably change until the primary voltage exceeded 800 V, however, even then only slightly, <5%. At a primary capacitor voltage of 500 V, only 25 mJ of energy are necessary for the discharge initiation including all four spark plugs.

High-speed photographs of the discharge were taken with an Imacon Fast-Framing Camera (IFFT) at rates of 500,000 frames per second. This diagnostic tool has been used before [10] to examine the symmetry of the discharge with an exposure to all visible wavelengths of light and was used in a similar fashion here. A series of IFFT frames of PT5 with the new DI circuitry are shown in Fig. 2.5 and show the resulting discharge symmetry.

2.3 Contamination Reduction at EPPDyL

Unlike previous pulsed thrust measurements at EPPDyL where impulse bits > 280 μNs[1] were measured repeatably, lower impulse bit measurements have shown signs of magnitude decay that seem to implicate pump-oil contamination effects. In these performance measurement experiments consisting of multiple repetitive trials with small mass bits, the magnitude of the impulse bit has been seen to decrease as the total number of pulses increases as can be seen in

---

[1]This number corresponds to the impulse bit of an LES8/9 APPT measured at EPPDyL[70] that agrees with measurements from other laboratories, for example[71].
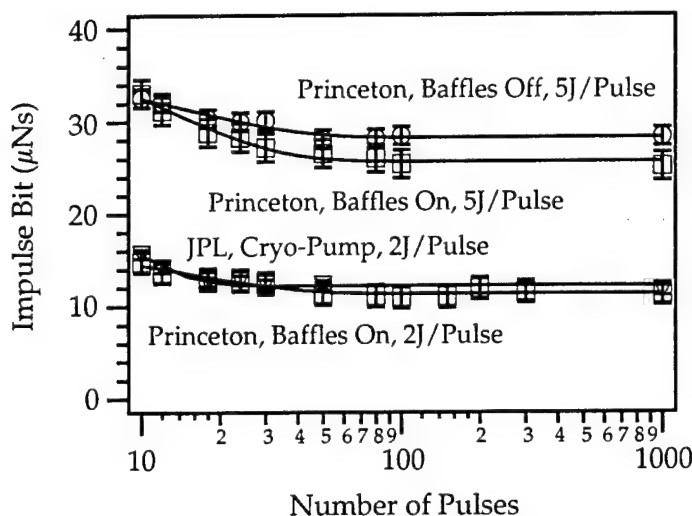
Figure 2.6: Impulse bit decay as a function of the number of pulses at two different energies and two different facilities.

Fig. 2.6. This impulse bit decay was first noted in experiments in Princeton last summer[45] and has also been noticed before in other experiments with GFPPTs where changing surface conditions were blamed[4]. To a large extent the accumulation of diffusion pump oil (used at Princeton for obtaining high vacuum) on the electrodes of the thruster has been blamed for the initially high impulse values. Line emission spectroscopy indicated that as more pulses are fired, more of the oil is removed from the electrodes gradually reducing the amount of extra mass and extra impulse provided by the contaminant to the discharge. As the number of pulses increases, the impulse value seems to reach an asymptote providing a "clean" data point.

Consequently, a substantial effort has been invested in cleaning the vacuum facility and modifying the existing baffle system to accept liquid nitrogen and reduce backstreaming as much as possible. These activities are described in detail in the appendix.

2.3.1 Overall Diffusion Pump Oil Contamination Reduction

To measure the level of background oil vapor, a UTI 100C residual gas analyzer (RGA) was connected to the tank through an isolation valve mounted on one of the optical ports at the end of the tank. The isolation valve was kept closed unless the LN$_2$ baffles were activated to reduce the possibility of the ionizing filament or faraday cup becoming contaminated. In addition, before making
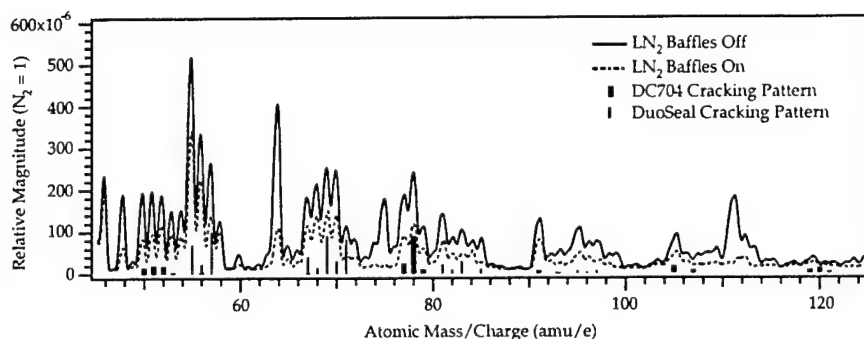
Figure 2.7: Mass spectrum of background gases from the RGA with baffles on and off as well as expected DC704 diffusion pump oil and DuoSeal roughing pump oil cracking patterns.

any of the measurements presented in this chapter, the entire RGA unit was baked at close to 200°C for over 48 hours to remove any contaminants from the gauge walls. Figure 2.7 shows a typical mass spectrum produced by the RGA just as the baffles were activated and two hours later. This figure also shows the predicted spectra of DC 704 diffusion pump oil and conventional Duo-Seal roughing pump oil both used in the high vacuum facilities at EPPDyL. Many of the peaks shown in Fig. 2.7 match up with those predictions indicating that diffusion and roughing pump oil vapors exist, however, at very low levels (partial pressures on the order of 20×10^{-9} Torr) compared to the background nitrogen levels. This data also shows an overall trend of about 50% reduction in background gases over a wide range of atomic masses. Choosing one atomic mass over charge value as a representative for diffusion pump oil levels (78 amu/e) and roughing pump levels (57 amu/e) allows a quantitative assessment of background vapor level during baffle cooling. These two levels were chosen from a list of maximum peaks in various cracking patterns. A graph showing the reduction of oil and water vapor as a function of time and baffle temperature is shown in Fig. 2.8. Again, this shows approximately a 50% reduction of possible contaminants after the baffles have been cooling for over 100 minutes down to a temperature of −60°C. This reduction level was confirmed by opening the RGA isolation valve for a short time after the liquid nitrogen cooling was deactivated and the baffles were allowed to completely warm up. The levels measured by the RGA at that time returned to the previous value before the baffles were activated.

2.3.2 Discharge Cleaning of SRL5e-GFPPT

Both spectroscopic studies and impulse measurements have shown that performance and background oil levels reach an asymptote after a small number of
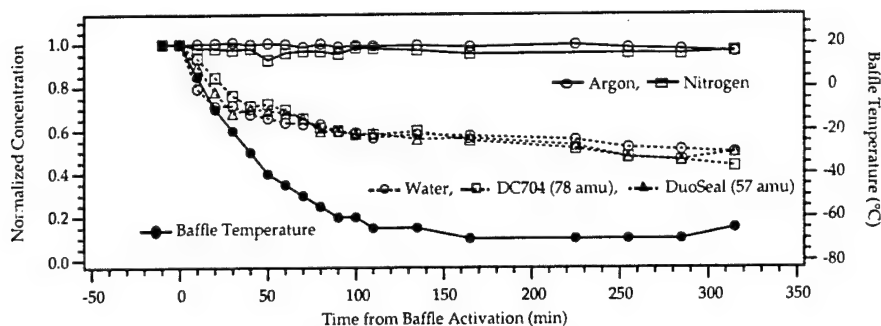
Figure 2.8: Baffle temperature and background gases as a function of time from baffle activation.

pulses indicating that the high current GFPPT discharge cleans potential contaminants off the electrodes on every pulse. Occasional breaks between pulses occur while waiting for the thrust arm to naturally relax back to its neutral position and during the cold gas measurements. These breaks between discharges can allow more deposits to build up which must then be cleaned off before accurate impulse measurements can be made. By experimenting with various delays between bursts, impulse bit increases were noticed (>5% increase) repeatably only for breaks larger than 10 minutes. A period of 50 seconds used between all bursts described in this chapter is considered a short enough time to insure an insignificant amount of oil has been deposited on the electrodes between trials.

RGA data taken after the electrodes had been cleaned by many discharges still showed a tenfold increase in DC 704 oil levels *immediately* after each burst. However, simultaneously, the increase in the argon levels due to the propellant flow were measured to be 1000 times larger than the oil levels. Oil level increases were much larger on the first few bursts after long delay without firing, however, levels returned to their lower steady values after only four or five bursts. From this observation, we can conclude that after the electrodes have been properly cleaned, the amount of oil residue in the discharge is minimal.

Using the discharge as a method for cleaning the thruster is a technique in the new performance measurement protocol at EPPDyL. As seen in Fig. 2.6, after an extended break, and especially after pump-down, at least 60 pulses (10 bursts) are required to bring the impulse bit level down to the asymptote that agrees with data taken at NASA-JPL immediately after pump-down.

2.3.3 Comparison of Results with Impulse Measurements at NASA JPL

In order to confirm that the asymptote level apparent after approximately ten bursts of six pulses each is a "clean" data point, the PT5 was tested in a known clean environment (a cryo-pumped facility that is only exposed to roughing
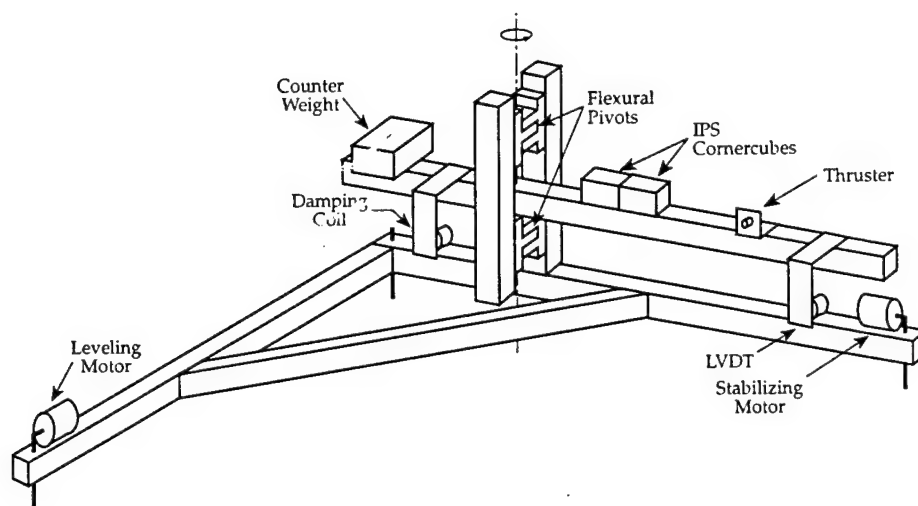
Figure 2.9: JPL micro-thrust stand.

pump oil during the pump-down phase of operation) at the same operating conditions.

Performance measurements taken at JPL were conducted in a 1.5 m diameter, 2.0 m long steel tank containing a Princeton-designed thrust stand (see Fig. 2.9) at NASA JPL. A CVI TM500 twenty inch cryo-pump brings the tank to an operating pressure of 1.5×10^{-6} Torr without propellant flow. Tank pressure peaked below 4×10^{-5} Torr during the maximum pulsed argon propellant flow. Care was taken to minimize mechanical pump oil back-streaming during rough pumping which was susrected to be a cause of contamination that can affect performance measurements. The impulse and performance measurements are made in a similar way to those at EPPDyL as described in Section 2.4.

Figure 2.6 shows both data taken at Princeton before the renovations at higher energy per pulse, 5 J, and data taken after the renovations using the same operating conditions as those tested at NASA JPL, approximately 2 J per pulse and 0.5 μg per pulse. Activation of the baffles reduced the asymptote level by 11% at the higher energy level while providing agreement within the error bars to the data set from JPL. In all cases, at least 50 pulses are required to reach the asymptote.

2.3.4   Impulse Measurement Protocol

A protocol for performance measurements that are free of contamination effects was developed in light of the above described experiments. It includes the following three guidelines:

1. The LN$_2$ baffles must be activated for at least 100 minutes before testing

to reach the correct impulse asymptote

2. After pump-down or extended times between hot pulses, 1000 pulses should be fired to insure that the thruster electrodes are clean and the impulse magnitude has reached an asymptote level.

3. Because of the ten minute break between hot pulses caused by routine cold gas measurements, the first 10 bursts (60 pulses) of 30 bursts at one operating condition should be ignored to insure uncontaminated impulse measurement.

This protocol was followed for every performance data point reported here.

2.4 Performance Measurements of PT5

For a GFPPT, performance is calculated based on the impulse produced by a measured amount of stored energy and the measured amount mass that was accelerated. The efficiency of a PPT is defined here in the conventional manner as a ratio of the directed kinetic energy to the initial stored energy,

$$\eta \equiv \frac{\frac{1}{2}m_{bit}\bar{u}_e^2}{\frac{1}{2}CV_0^2} = \frac{I_{bit}^2}{m_{bit}CV_0^2}, \tag{2.1}$$

where the mass bit, m_{bit}, is found from the mass flow rate as described in Section 2.4.2, the average exhaust velocity, $\bar{u}_e$, is defined as $\bar{u}_e \equiv I_{bit}/m_{bit}$, C is the measured capacitance, V_0 is the measured initial voltage on the capacitor, and I_{bit} is the average impulse of one pulse in a burst or the "impulse bit". For a PPT, the thrust-to-power ratio is the same as the impulse bit to energy bit ratio,

$$\frac{T}{P} = \frac{I_{bit}}{E} = \frac{I_{bit}}{\frac{1}{2}CV_0^2}. \tag{2.2}$$

Finally, the specific impulse is the amount of impulse provided by the thruster per unit weight on earth of the propellant used in the pulse,

$$I_{sp} = \frac{I_{bit}}{m_{bit}g_0} = \frac{\bar{u}_e}{g_0}. \tag{2.3}$$

To evaluate these parameters, three measurements are required for each individual pulse: stored energy, mass bit, and impulse bit. For all data presented in this chapter, a train of six pulses was fired per trial at close to 270 μs intervals. All results consist of what would be the average value of a single pulse in that train. The techniques for finding these average per-pulse values are described below and a schematic of the entire experimental set-up is shown in Fig. 2.10.
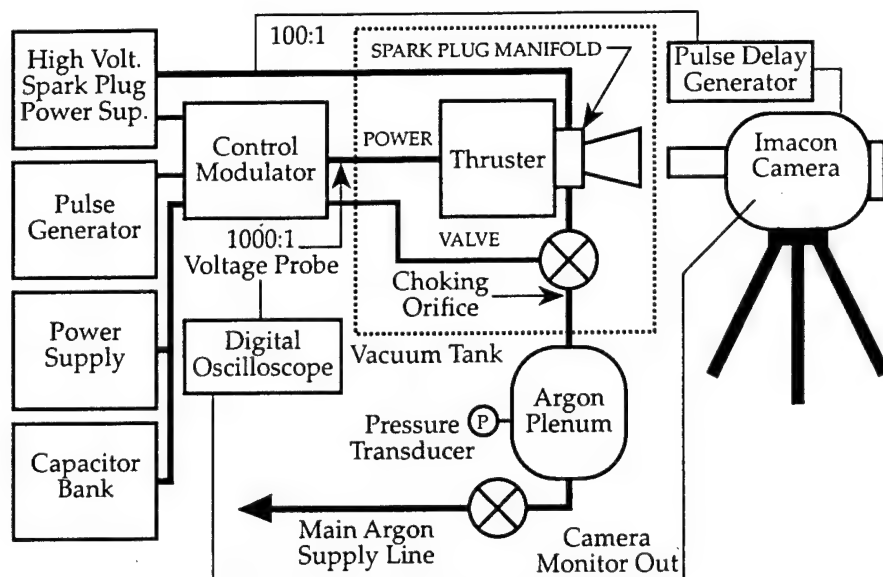
Figure 2.10: Schematic of the SRL-GFPPT experiment including the Imacon camera and related equipment.

2.4.1 Pulse Energy Determination

The primary capacitor voltage is measured at the charging supply through a calibrated 1000:1 voltage probe. For each set of pulses, a voltage trace is captured on a digital oscilloscope showing the charging and discharging cycle of the capacitor for all the pulses in the burst. The oscilloscope is set to acquire the discharge voltage history with sufficient speed and resolution to allow the current history to be accurately inferred from the numerical voltage derivative. To determine the energy per pulse, the voltage trace is squared and multiplied by the measured capacitance with a typical accuracy of within 1.5 %. The peak energy before every pulsed is averaged to determine the energy per pulse and the standard deviation of that average is used as the error in this measurement. For most measurements, this error is below 4%.

2.4.2 Mass Bit Determination

Propellant, in this case argon, is supplied to PT5 through a valve, choking orifice, and plenum arrangement as shown in figure 2.10. The valve is located approximately 10 cm upstream from the thruster propellant injection ports. It is opened and closed by the control module and timed by a signal generator. For these experiments, the valve was open for 45 ms and the thruster was set to fire 40 ms after the valve opened to allow sufficient time for the gas to reach a steady flow rate. This time could be reduced with faster acting valves. The mass flow

rate is controlled by changing the pressure in the plenum upstream of the sonic orifice. Soon after the valve is open, the flow is choked and a steady-mass flow rate is reached. In this case, the sonic orifice is a copper plate with a 0.36 mm hole. The mass flow rate as a function of plenum pressure was measured to calibrate the sonic orifice before the database was taken.

The mass bit value itself comes from the timing of the pulses within a burst. This timing is determined from the main capacitor voltage trace. Except for the first two pulses which are slightly longer, all the later pulses have close to 270 μs between discharges. This time multiplied by the mass flow rate generates an average mass bit for each pulse in the pulse train. Obviously, for the first pulse, mass is entering the thrust chamber for much longer than 270 μs, however, the cold gas exhaust velocity has been measured at close to 400 m/s. At that speed, if the gas is moving primarily in the axial direction, it would begin to leave the thrust chamber after only about 200 μs. Therefore, we expect similar gas loading conditions for each pulse.

2.4.3 Impulse Measurement

The impulse produced by a PPT discharge is measured by monitoring the position of the thruster mounted at the end of a swinging gate type thrust stand. The thrust stand has a vertical rotational axis through two flexural pivots that allows relatively free rotational motion in the horizontal direction. Knowing the position of the thruster at all times allows the impulse to be determined based on calibrated thrust stand dynamics. These dynamics as well as the position measurement system are described in ref. [70].

2.4.4 Measurement Sequence and Error Analysis

The sequence of experimental trials was designed to reduce the average error in the measurements through repetitive testing at the same conditions. One data point represents the operation of the thruster at one initial stored energy value and one mass bit condition. As described in Section 2.3.4, one data point is made up of 40 impulse measurement trials including 10 cold-gas pulses (where the thruster capacitors are not charged) and 30 "hot" pulses used to determine the impulse bit and shot-to-shot repeatablity.

In all the trials, the impulse is actually measured for one *burst* of pulses and the impulse bit of a particular trial is the *average* impulse per pulse in the burst obtained by measuring the impulse and dividing by the number of pulses in a burst. Since the propellant flows for much longer than the burst time, typically 65 ms of effective gas flow compared to 2 ms of pulses, during thruster operation the cold-gas contribution to the impulse is completely subtracted before any performance calculations are made. This subtraction yields the hot impulse value. The cold-gas impulse is determined for each mass bit by averaging 10 trials at the same plenum pressure without charging the main capacitors. All the impulse data presented in this report are found by averaging the hot impulse values from the last 20 of the 30 hot trials. The first ten trials at any condition

are discarded due to the impulse bit decay phenomena present in the data as discussed in Section 2.3.

The error in measuring a particular impulse comes from the effective mass calibration error, the error in measuring the thrust arm velocity just before the impulse accurately, and the random noise in the position history. Putting these factors together, the average error for a single impulse measurement is $< 3\%$. Typically the average cold-gas impulse from 10 trials has a standard deviation of $\pm 3 \mu$Ns out of a typical value of 100 μ Ns indicating good shot-to-shot repeatablity with a small error. The average hot impulse has a standard deviation of $\pm 10 \mu$Ns out of typically 100μNs or about $\pm 10\%$. This deviation is a result of deviations of energy, mass-bit and spark plug operation from pulse to pulse. Performance parameters such as efficiency and the thrust-to-power ratio are calculated from measurements made on individual trials to bring out this correlation and reduce the overall error. The final error associated with each performance parameter is simply the standard deviation of the average parameter value over 20 measurements at the same conditions. Typical errors for the efficiency and thrust-to-power ratio are near 10%.

2.4.5 Experimental Results

Two energy levels for each of two capacitance values were tested over ten different mass bit values each yielding a 40-point GFPPT performance database. Four graphs which show PT5 performance as a function of mass bit and specific impulse with the capacitance and the initial stored energy level as parameters are shown with error bars in Fig. 2.11. The lines between the data points are simple fourth order polynomial curve fits meant to show overall trends apparent in the data, however, this is not necessarily the correct functional form to the data. The coefficients for the curve fits are not shown here as the chosen curve-fit function did not always match the data well, especially at low specific impulse values. Tables of the performance data are given at the end of this article.

2.5 Discussion

It is evident from all the plots in Fig. 2.11 that there is for each curve a transition with decreasing mass bit (or increasing I_{sp}) from a mode (Mode I) where the efficiency and the impulse are respectively independent and dependent on the mass bit (and where the efficiency the thrust to power ratio are respectively independent and dependent on I_{sp}) to another mode (Mode II) where the converse statements hold.

We now explore these trends and their significance using the theoretically expected scaling corresponding to electromagnetic or electrothermal acceleration.
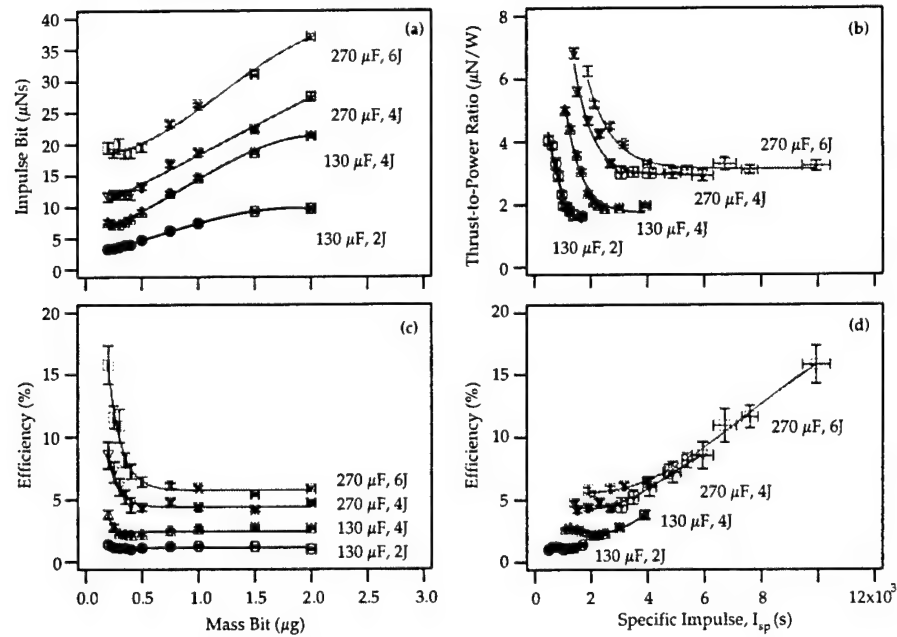
Figure 2.11: Performance of PT5. Graphs (a) and (c) show the impulse bit and efficiency as a function of mass bit. Graphs (b) and (d) show the thrust-to-power ratio and efficiency as a function of specific impulse. All graphs contain four curves which show changes in performance due to changing capacitance values and initial stored energy levels.
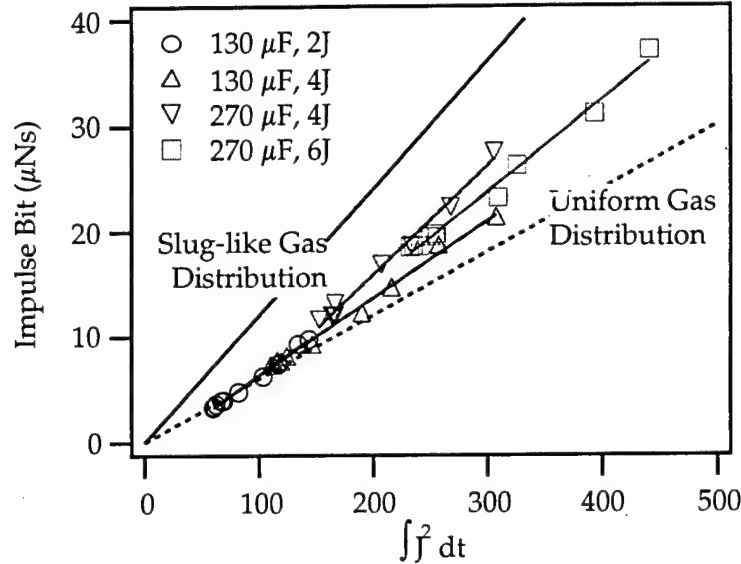
Figure 2.12: PT5 impulse bit as a function of the integral of the current squared during the discharge. Two lines showing the predicted performance from electromagnetic theory for two different mass distributions are also shown.

2.5.1 Theoretical Electromagnetic Performance

Simple models neglecting the gas dynamics of sweeping up the mass in front the snow-plow-like current sheet have been presented and used before to examine PPT performance trends [45, 65, 44, 54]. Most of these models assume an equivalent RLC circuit for the discharge including a variable inductance, a fixed capacitance and a resistance based on the plasma conductivity. The simplest relation for the impulse bit of a self-field, co-axial PPT based on an electromagnetic acceleration mechanism is,

$$I_{bit} = \frac{\mu_0}{4\pi} \ln \frac{r_{out}}{r_{in}} \int J^2 dt = \frac{1}{2} L_1 \int J^2 dt, \qquad (2.4)$$

where L_1 is the inductance-per-unit-length, mainly a geometry parameter. This equation does not include any losses associated with the dynamic efficiency. The impulse bit would be reduced by a factor of one-half, for example, if there was a uniform propellant distribution in the discharge chamber before the pulse [42]. A graph showing measured impulse bit as a function of the measured integral of the current squared is shown in Fig. 2.12. This graph also contains two lines which show what Eq. 2.4 predicts using both a slug-like propellant distribution where all the propellant mass is included in the beginning of the discharge and a uniform propellant distribution where the impulse is reduced by half. This

graph shows that most of the data follows a linear relation between the impulse bit and the integral of the current squared while falling somewhere between a dynamic efficiency of 50 and 75%.

By considering the relations between the current magnitude and driving capacitance as well as the changing inductance based on the current sheet velocity, two other relations can be derived[65, 44, 54],

$$I_{bit} \propto EL_1\sqrt{\frac{C}{<L>}}, \tag{2.5}$$

$$\eta \propto I_{sp}L_1\sqrt{\frac{C}{<L>}}, \tag{2.6}$$

where $<L>$ is the average inductance as the current sheet propagates down the electrodes. In ref. [44] this term has been replaced by the product of the inductance-per-unit-length times some average length of electrode required to accelerate the current sheet to its final velocity, yielding

$$I_{bit} \propto E\sqrt{\frac{CL_1}{<l_{elec}>}}. \tag{2.7}$$

As the electrode geometry does not change throughout the experiment, the terms relating to the inductance should be fairly constant and we should see more of a dependence on thruster performance with the square-root of the capacitance. To demonstrate this trend in the database, a "normalized" impulse bit will be defined as,

$$I_{norm} \equiv \frac{I_{bit}}{E}\sqrt{\frac{<l_{elec}>}{CL_1}}, \tag{2.8}$$

with l_{elec} set to a constant value of 8 cm for PT5. A plot showing the normalized impulse with varying mass bit is presented in Fig. 2.13. This plot, in comparison to Fig. 2.11(a) shows that, especially for low mass bits (high I_{sp}), the normalized impulse relation collapses all the curves with varying energy and capacitance onto one. In general the trend of the impulse bit scaling with the energy level and square-root of the capacitance level is present throughout the data. The normalized impulse values greater than unity correspond to mass bits > 0.5 μg and Mode I operation as described previously. These higher than expected values could be explained by the choice of a constant $<l_{elec}>$ being the full extent of the electrodes. It could be that at these higher mass bits the current sheet does not travel the complete length before the discharge is extinguished and the normalized impulse should be reduced. This also has implications for changing the dynamic efficiency if the mass accumulation process is different is this mode of operation.

Equation 2.7 implies that the thrust-to-power ratio is dependent on the square-root of the capacitance and is independent on the energy in the pulse. This trend is present in the data as shown in Fig. 2.14 where the mass bit is held constant and the energy is varied as a parameter in measuring the impulse. The graph shows that the impulse bit is linearly related to the discharge energy
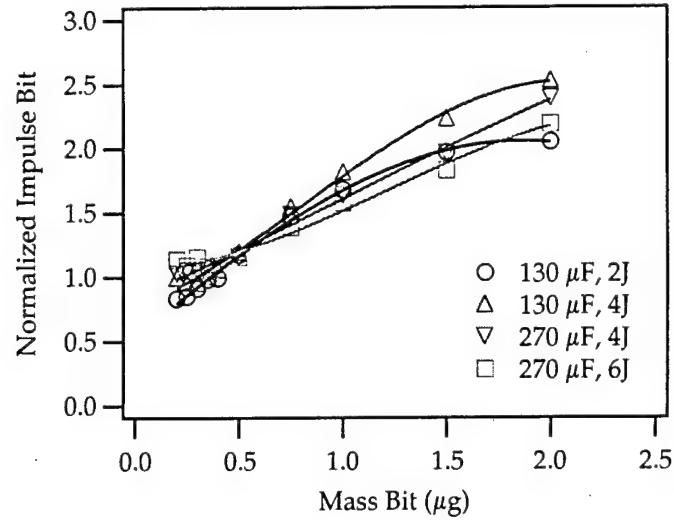
Figure 2.13: PT5 normalized impulse bit (see Eq. 2.8) as a function of mass bit at various capacitance and energy levels. The error bars are not larger than the markers.
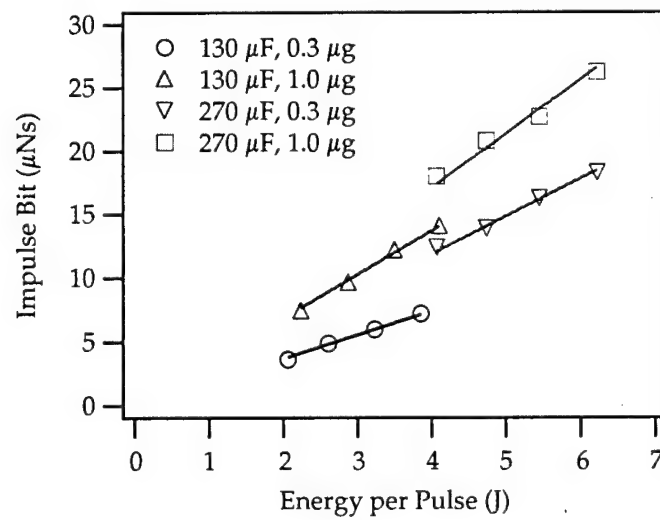

Figure 2.14: PT5 impulse bit as a function of initial stored discharge energy for two different mass bits and two levels of capacitance.

for both small and large mass bit values (both Mode I and Mode II operation) and various levels of capacitance. This implies that the thrust-to-power ratio (impulse bit to energy ratio) does not depend on discharge energy which is to be expected in an electromagnetic accelerator.

The dependencies suggested for a thruster where electrothermal acceleration is dominant are quite different[54]. In that case, the impulse bit is expected to scale with the square root of the discharge energy to mass bit ratio and not depend directly on capacitance or inductance change. In addition, the efficiency of a pure electrothermal accelerator is expected to be constant over wide range of specific impulse, energy and mass bit values. While the efficiency as seen in panels c and d of Fig. 2.11 is indeed independent of mass bit and I_{sp} at high mass bit values (i.e. Mode I), it does show a dependence on energy, albeit a weaker one than for Mode II. This tends to indicate that the acceleration in Mode I may be due to a combination of both electrothermal and electromagnetic effects. Again, as the losses associated with sweeping up the propellant are not accounted for in our predictions, an explanation for trends in Mode I could be a function of improved dynamic efficiency as well.

2.5.2 Influence of Erosion Products on Performance

Erosion rate measurements conducted at JPL using a slightly smaller, parallel-plate geometry GFPPT have shown that the electrodes, specifically the cathode and spark plug, can erode a significant amount per discharge relatively independent of discharge energy and mass bit levels. It is believed that most of the erosion comes from the stainless-steel spark plug cathode possibly late in the discharge as seen from bright spots near the spark-plugs in Imacon FFT pictures. Currently work is continuing at EPPDyL to quantify the erosion rates of the spark plug ignitors in the co-axial geometry GFPPT. The erosion of electrode material plays, as yet, an unknown role in GFPPT performance. Although preliminary results from measurements at EPPDyL suggest that erosion rates in PT5 are very similar to those measured at JPL, a similarly large amount of material was found to be *added* to the anode PT5 suggesting that the erosion products do not entirely contribute to the exhaust. Experiments are planned at EPPDyL to accurately quantify erosion and deposition rates and asses their influence on performance.

2.6 Conclusions

The following summary and conclusions can be drawn from the above study:

- Impulse bit measurements with mass bits on the order of 1 μg/s and lower may be affected significantly by contamination from diffusion pumps and required a major renovation of the facilities at EPPDyL including the implementation of LN$_2$-cooled baffles and the development of a protocol for thruster decontamination which was verified by comparing the data with measurements taken in a cryo-pumped facility.

- A new discharge initiation circuit was required to provide a reliable, symmetric breakdown to begin each pulse, significantly improving thruster performance and shot-to-shot repeatablity.

- With an effective method for measuring the impulse and a repeatable discharge, an argon propellant database was collected over various mass bits, energy levels, and capacitance values.

- Two modes of performance scaling were clearly discerned in each of the performance curves. For all operation parameters fixed, decreasing the mass bit lead to a transition to a mode in which the measured performance scales as theoretically expected from electromagnetic acceleration. Specifically, the impulse bit, efficiency, and thrust-to-power ratio all scale with the square-root of capacitance.

2.7 APPENDIX: Test Facility Changes

In order to reduce the diffusion pump oil back-streaming rate into the test facility at EPPDyL two major steps were taken: vacuum chamber cleaning and repair as well as the installation of liquid nitrogen cooling lines to the existing baffle system. Both of these renovations will be described in more detail in this section of the chapter.

2.7.1 Vacuum Chamber Cleaning and Repair

The vacuum vessel used for this study is a 2 m diameter, 5 m long fiberglass tank shown in Fig. 2.15 which is backed by two 48 inch diffusion pumps and a large 1340 cfm roughing system. This facility has accumulated over 50,000 hours of operation since it was first evacuated twenty years ago. Experiments performed in this facility have included use of quasi-steady magnetoplasma-dynamic thrusters (MPDTs), ablative pulsed plasma thrusters (APPTs), and many other devices. Over time, residual roughing and diffusion pump oil as well as various erosion products from different experiments have built up on the facility walls. As part of the facility renovations, the entire interior surface of the tank was cleaned by scrubbing with iso-propyl alcohol effectively eliminating the background contaminants from the walls.

The facility has also experienced some surface fatigue due to pressure cycling. This is apparent from the visual cracks in the gel-coat surface covering the fiberglass flanges and optical ports. The cracks produced numerous small leaks which increased the background pressure and, therefore, oil back-streaming rate. The cracks were repaired through a process of grinding out the material around each crack and replacing removed with three layers of gel-coat epoxy. Care was taken to replace the smooth finish of the flange surfaces keeping leaks to a minimum. After all repairs were complete, the facility background pressure was reduced by 50% to an operating pressure now normally below 4×10^{-5} Torr.
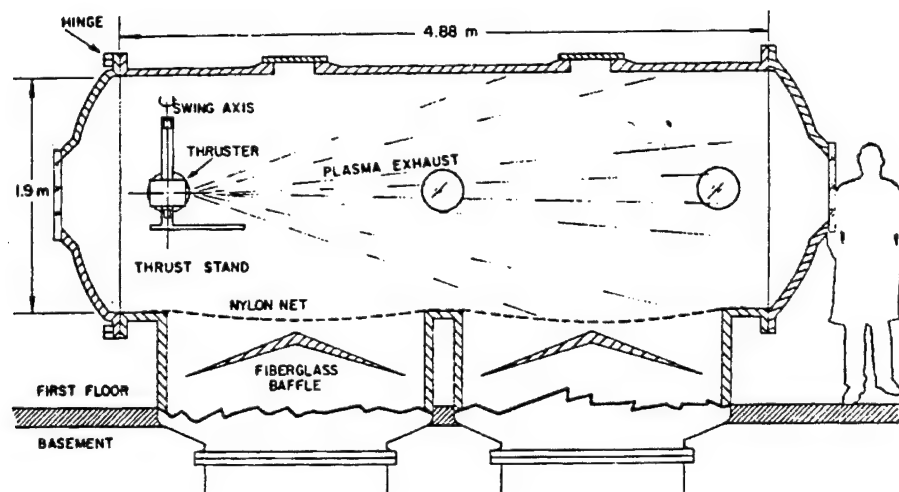
Figure 2.15: Drawing of the Pulsed Performance Measurement facility at EP-PDyL showing thrust stand and baffle location.

2.7.2 Activation of Liquid Nitrogen Cooled Baffles

Further reduction of diffusion pump oil back-streaming and contamination requires active cooling of baffles or traps very near the diffusion pump entry into the facility. The baffles in the fiberglass facility at EPPDyL (shown in Fig. 2.15) have been in place since its construction, however, they have not been actively cooled until recently. The baffles used here are low-profile fiberglass cones with a copper plate attached on the underside towards the diffusion pump. Copper tubing (3/8" diameter) is attached to the copper plate with small clamps in a spiral configuration. Only two inches separate each turn of the coil, and the total length of the lines close is to 150 ft. for each baffle. Originally designed for a freon-based cooling system, the baffles have been converted for liquid nitrogen cooling by the installation of new cryo-genic feed-throughs and the replacement of all Swagelok fittings with hard-soldered connections. The baffles are connected in parallel for even cooling and have Type T thermocouples mounted to the inlets and outlets of both baffles inside the tank. Liquid nitrogen is supplied for eight hours at a time by a 160 liter portable dewar that is refilled before each test. Between tests, the baffles are *not* actively cooled requiring a cleaning process before testing as described in Section 2.3.2.

Slightly more than an hour after activation, the baffles reach their lowest operating temperature of at most −70°C as measured by the outlet temperature of the baffle cooling lines. The inlet temperature reaches −180°C almost immediately after activation and both baffles generally cool down at the same rate.

m_{bit} (μg)	I_{bit} (μN-s)	I_{sp} (s)	η (%)
0.20	11.6	5940	8.53
0.25	12.0	4890	7.20
0.30	11.9	4060	6.01
0.35	12.0	3500	5.22
0.40	12.0	3060	4.56
0.50	13.2	2680	4.35
0.75	16.9	2290	4.77
1.00	18.6	1900	4.35
1.50	22.3	1520	4.16
2.00	27.6	1410	4.70

Table 2.1: PT5 performance data for a fixed energy of 4.0±0.1 J and a capacitance value of 270±3 μF. The last row in the table is the average error from each measurement.

The background tank pressure typically decreases by 10% due in a large part to the freezing of water vapor to the baffle surface. The baffle operation and cooling rate are very similar from test to test although the outlet temperature of the baffle is verified to be below $-60°$C before any testing begins.

m_{bit} (μg)	I_{bit} (μN-s)	I_{sp} (s)	η (%)
0.20	19.5	9930	15.8
0.25	18.6	7600	11.6
0.30	19.8	6720	10.9
0.35	18.5	5400	8.16
0.40	18.6	4740	7.26
0.50	19.5	3990	6.42
0.75	23.2	3160	6.12
1.00	26.3	2680	5.91
1.50	31.1	2120	5.40
2.00	37.1	1890	5.79

Table 2.2: PT5 performance data for a fixed energy of 6.0±0.1 J and a capacitance value of 270±3 μF. The last row in the table is the average error from each measurement.

m_{bit} (μg)	I_{bit} (μN-s)	I_{sp} (s)	η (%)
0.20	3.32	1690	1.37
0.25	3.39	1380	1.15
0.30	3.64	1240	1.10
0.35	3.97	1160	1.11
0.40	4.00	1020	0.99
0.50	4.80	980	1.12
0.75	6.24	848	1.21
1.00	7.42	757	1.23
1.50	9.30	632	1.21
2.00	9.75	497	0.99
±2%	±8%	±5%	±10%

m_{bit} (μg)	I_{bit} (μN-s)	I_{sp} (s)	η (%)
0.20	7.68	3920	3.81
0.25	7.38	3010	2.80
0.30	7.32	2490	2.31
0.35	7.74	2260	2.21
0.40	8.21	2090	2.16
0.50	9.29	1900	2.20
0.75	12.2	1670	2.50
1.00	14.7	1500	2.64
1.50	18.7	1270	2.76
2.00	21.4	1091	2.68
±2%	±8%	±5%	±10%

Table 2.3: PT5 performance data for a fixed capacitance value of 130±2 μF and energy levels of 2.1±0.1 J and 4.0±0.1 J. The last row in the table is the average error from each measurement.

Chapter 3

Effects of Capacitance, Electrode Geometry, and Inductance per Unit Length

3.1 Introduction

Due to the complex multi-variable nature of pulsed plasma thruster design, investigators have turned to empirical, parametric studies to understand how electrode configuration impacts performance. Specifically, the advantages and disadvantages of the two main types of electrode geometry, co-axial and parallel-plate, have for long been a topic of debate. Experimental data have yet to uncover the best configuration for performance (efficiency and thrust-to-power ratio) over a wide range of operational parameters.

Recent activity at the Electric Propulsion and Plasma Dynamics Lab (EP-PDyL) of Princeton University in cooperation with Science Research Laboratory, Inc. (SRL) and the Advanced Propulsion Group at NASA Jet Propulsion Laboratory (JPL) has focused on designing gas-fed PPTs (GFPPTs) with modular components such as capacitance[5] and electrode geometry[55] to measure the various effects on performance. Through analytic models of electromagnetic acceleration, the performance of GFPPTs is expected to scale with the square-root of the product of capacitance and inductance-per-unit-length while being independent of propellant mass. In actual GFPPTs, however, a portion of the injected propellant mass may escape the electrode volume before being entrained by the accelerating current sheet. This results in a low *propellant utilization efficiency* which adversely impacts the overall performance. The propellant utilization efficiency is shown to scale with the *inverse* of capacitance which limits the extent to which the performance can be improved by varying the capacitance. This leaves the inductance-per-unit-length as the most promising design parameter that can influence overall performance over a wide

Thruster	Geometry	Cap. (μF)	$L^{'}$ (nH/cm)
PT5	Co-axial	130	~ 2.8
PT6a	Co-axial	63	~ 1.3
PT6b	P-Plate	63	~ 4.9
PT8	P-Plate	63	~ 6.3
PT9a	P-Plate	130	2.83
PT9b	P-Plate	130	5.68

Table 3.1: Thruster electrode configuration, capacitance, and inductance-per-unit-length. Because PT5, 6, and 8 have slightly flared electrodes the inductance-per-unit-length value, $L^{'}$, shown here is the average value.

range of operational conditions.

The purpose of this chapter is twofold: 1) to help verify the relation of inductance-per-unit-length (and hence electrode geometry) to GFPPT performance in a systematic way, and 2) to discuss which electrode geometry (co-axial or parallel-plate) is better for overall performance.

The chapter begins by describing the four different GFPPTs used in performance testing. The following section defines the propellant utilization efficiency and derives a theoretical relation for the dependence of performance on capacitance and inductance-per-unit-length. Next, performance measurements are presented and trends in the data are used to discuss the effects of inductance-per-unit-length. Finally, there is a discussion of other factors such as wall losses and non-uniform current sheet profiles which could influence the debate on which electrode geometry is better.

3.2   The SRL Family of GFPPTs

The SRL family of GFPPTs has been described before in refs. [5, 55] and will only be summarized here. SRL-GFPPTs use modern pulse forming technology to create a series of high-repetition rate pulses that are grouped in bursts. During one burst of pulses, propellant flows at a constant rate filling the discharge volume just before the next pulse occurs. If the the time between pulses, τ_p, is too long or the electrode length, ℓ_{elec}, is too short, a slight amount of propellant mass may be lost as described in more detail in Section 3.3.1 and shown schematically in Fig. 3.1. The overall performance of GFPPTs is related to the driving capacitance, electrode configuration, propellant loading, and many other parameters that have been explored through the creation of many generations of GFPPT designs[5, 55].

All the relevant parameters of the designs tested in this study are illustrated in Table 1. Of these thrusters, only PT8 and PT9 have not been introduced in the literature and a more detailed description of them follows.
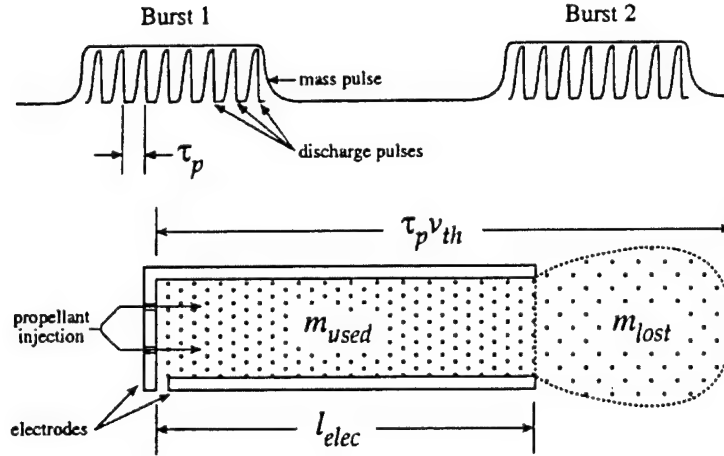
Figure 3.1: Schematic drawing of the high-repetition pulse sequence in SRL-GFPPTs and the injected propellant mass distribution just before a pulse. The time between pulses, τ_p, is typically between 100-500 μs with the accelerated mass much greater than the non-accelerated mass, $m_{used} \gg m_{lost}$.

3.2.1 PT8

PT8 is a slightly flared[1] parallel-plate GFPPT that belongs to the group of GF-PPTs including PT6 and PT7 called the "quad thrusters" which are explained in more detail in ref. [55]. Compared to the first quad designs, PT8 has three major modifications: it uses a new lower-energy RF system to initiate the discharge, it uses a non-axial propellant injection scheme to reduce the axial cold gas velocity and improve propellant utilization, and it has a set of ferrite blocks around the electrodes to reduced magnetic field fringing effects and increase the inductance-per-unit length. Although the magnetic field of PT8 has yet to be measured, it is assumed that the ferrite blocks will remove the fringing effects of the finite parallel-plate geometry and provide a uniform magnetic field with an L' value of approximately 6.3 nH/cm. PT8 has the highest value of L' out of all the thrusters used in this study.

3.2.2 PT9

PT9 uses the capacitors and thruster casing from PT5 (see ref. [5]) with a modular set of parallel-plate electrodes for testing various values of inductance-per-unit-length. All the electrodes are made from 1/8" thick 70% tungsten 30% copper plates with dimensions of 1" x 4" (width x length) or 1/2" x 4". There are two places to mount the electrodes at distances of either 1" or 1/2" apart,

---

[1]Although PT6b and PT8 have slightly flared electrodes with expansion angles of $< 10°$, they will be classified here using the conventional term "parallel-plate".

and both mountings include a uniform, axially directed propellant flow. This gives four different electrode configurations (aspect ratios) and three different inductance-per-unit-length values. Two of the four configurations were tested for this study including the smallest (PT9a, H/W = 0.5, L' = 2.83 nH/cm) and largest (PT9b, H/W = 2, L' = 5.68 nH/cm) values of inductance-per-unit-length.

For discharge initiation, PT9 uses a high voltage (2 kV) low energy (50 mJ) spark between a sharp, 10 mil tungsten wire and the cathode of the thruster. Although erosion rates have yet to be measured accurately for this thruster, visible damage to thruster components is greatly reduced compared to damage seen in life-tests with the surface-discharge plugs in PT7 [55]. The main purpose of PT9 is to test different inductance-per-unit-length configurations at similar operational conditions to those tested with the co-axial set of electrodes in PT5 which has roughly the same value of L' as PT9a.

3.3 Performance Considerations for Both Geometries

This section of the chapter will document the calculations used to compare the performance of *both* co-axial and parallel-plate GFPPTs tested at EPPDyL and NASA JPL. Conventional definitions for efficiency, thrust-to-power ratio, and specific impulse will be used as defined in ref. [5]. A derivation of the propellant mass utilization efficiency is shown to depend on electrode length, discharge pulse frequency and propellant type. The derivation of this efficiency helps to show why the capacitance can not be raised to an arbitrary value without possibly wasting propellant. Through the use of an electromagnetic acceleration model for GFPPT discharges, the trade-offs between the predicted thruster performance and the propellant utilization efficiency will be discussed. Through this analysis, the inductance-per-unit-length is found to be an important parameter in performance scaling. Finally, calculations of L' for the two geometries are presented.

3.3.1 Propellant Utilization Efficiency

In high repetition rate GFPPTs the total mass bit value, m_{bit}, used for overall performance calculations is a product of the the steady mass flow rate, $\dot{m}$, and the time between pulses, τ_p, during a burst. As shown schematically in Fig. 3.1, depending on the electrode length and the mean thermal velocity of the cold gas, v_{th}, some of the mass included in this efficiency calculation might not actually be accelerated by the discharge. Using the maximum possible thermal velocity, v_{th}, the axial extent of the cold-gas column before each discharge can be estimated by,

$$\ell_{gas} = v_{th}\tau_p = \tau_p\sqrt{\frac{3kT}{m_w}}, \tag{3.1}$$

with the total mass bit including *all* the injected propellant mass,

$$m_{bit} = \dot{m}\tau_p \;=\; \dot{m}\frac{\ell_{elec}}{v_{th}} + \dot{m}(\tau_p - \frac{\ell_{elec}}{v_{th}})$$
$$=\; m_{used} + m_{lost}. \tag{3.2}$$

As an example, using argon and a pulse frequency of 4 kHz, $\ell_{gas} \approx 10$ cm and the electrodes must be made at least 10 cm long or some portion of the gas will escape the electrode volume.

The propellant mass utilization efficiency, η_{pu}, can now be defined as the ratio of the electrode length, ℓ_{elec}, to the gas column length, ℓ_{gas}.

$$\eta_{pu} \equiv \frac{\ell_{elec}}{\ell_{gas}} = \frac{\ell_{elec}}{\tau_p}\sqrt{\frac{m}{3kT}} = \frac{m_{used}}{m_{bit}}. \tag{3.3}$$

Obviously even if the electrodes are longer than the gas column, the propellant utilization efficiency can not exceed 100%.

3.3.2 System Wide Trade-offs for Maximizing Propellant Utilization

From Eq. (3.3), maximizing the propellant utilization efficiency can include selecting a large molecular weight propellant, pulsing at a high frequency, using long electrodes, or a combination of these prescriptions. Changing these parameters, however, may have an adverse effect on performance and there are recognizable trade-offs in terms of predicted electromagnetic performance. In ref. [5] we derived the following theoretical expressions for GFPPT performance,

$$\eta_t \propto \frac{u_e}{2}\sqrt{\frac{CL'}{\ell_{elec}}} \qquad \frac{T}{P} \propto \sqrt{\frac{CL'}{\ell_{elec}}}, \tag{3.4}$$

where η_t is the *thrust* efficiency and u_e is the velocity of the current sheet at the end of the electrodes. These relations assume that the discharge is mainly an *inductive* load that reaches the end of the electrodes at the moment the capacitor is fully drained. This expression for thrust efficiency represents the *maximum* obtainable efficiency when the propellant utilization efficiency is 100%. The *overall* efficiency, η, is the product of the thrust efficiency and the propellant utilization efficiency,

$$\eta = \eta_t \eta_{pu} = \frac{\frac{1}{2}m_{bit}\bar{u}_e^2}{E}, \tag{3.5}$$

where the mass averaged exhaust velocity, $\bar{u}_e$, is calculated from the impulse bit,

$$\bar{u}_e \equiv \frac{I_{bit}}{m_{bit}} = \eta_{pu} u_e. \tag{3.6}$$

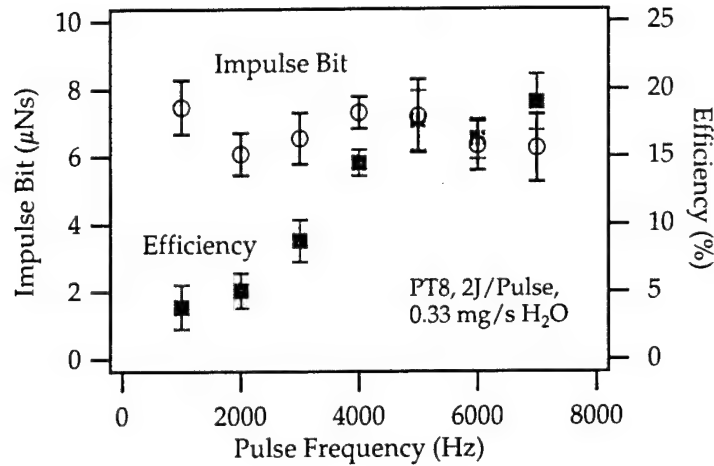Note that the thrust-to-power ratio does not depend on η_{pu}.

Figure 3.2: Impulse bit and efficiency as a function of pulse frequency for PT8 using water vapor for propellant at 2 J per pulse.

Large Molecular Weight Propellant. At a fixed plenum temperature, larger molecular weight propellants yield a lower thermal velocity. Compared to smaller molecular weight propellants at similar mass loading conditions, heavier molecules will also provide a smaller gas-dynamic pressure in the discharge chamber before the pulse begins, however, they have a higher viscosity coefficient. The choice of propellant molecule may effect the conductivity of the plasma and possibly cause frozen flow losses which could also adversely effect performance although this remains to be studied in GFPPTs.

High Pulse Frequency. The minimum time between pulses (the highest pulse frequency) is regulated by the time to charge the main capacitor. It is proportional to the capacitance magnitude and can be reduced by simply using smaller capacitance values or increasing the charging current, however, the latter choice can also decrease the power conditioner performance. The benefit of setting the pulse rate to the maximum the capacitance will allow is shown in Fig. 3.2 where the overall efficiency can be seen to increase to its maximum value as the pulse frequency increases at a constant mass flow rate. Note that the impulse bit, and therefore the thrust-to-power ratio, does not change within the error of the measurements and is not dependent on the propellant utilization efficiency.

A contrary argument to decreasing the capacitance can be seen from Eq. (3.4) and experimental evidence in ref. [5] which suggests that the performance of a GFPPT increases with the square-root of the capacitance. This trade-off between the discharge performance and the propellant utilization efficiency points to using smaller capacitances until η_{pu} is exactly unity. Yet, although the over-

all efficiency may now be optimized, the maximum *possible* performance still occurs at the highest values of capacitance. Therefore, decreasing the capacitance of a GFPPT may not be the best way to improve the propellant utilization efficiency and should only be used if no other avenue is possible. On the other hand, increasing the capacitance to boost performance makes it more and more difficult to obtain reasonable propellant utilization. This points to using the inductance-per-unit-length parameter instead of capacitance as a way to increase performance as further described in Section 3.3.3.

Electrode Length. It can be seen from Eqs. (3.3) and (3.4) that there is a complex trade-off between lengthening the electrodes to use all the propellant effectively and a decrease in the predicted performance. At the same time, if the electrodes are short and the mass bit is small (typically where the highest performance occurs), then the current sheet will not reside within the electrodes long enough to absorb all the energy from the capacitor. In addition, the total inductance change with a short set of electrodes may not be large enough for efficient electromagnetic acceleration. Therefore, the electrode length, the operational mass bit, and the capacitance must be chosen so that η_{pu} is near 100% and that the current sheet is at the end of the electrodes just as the capacitor is fully drained. There is also the possible factor of increased viscous and heat transfer losses from longer electrodes that has been noticed in these studies and will be explained further in Section 3.5.1.

3.3.3 Inductance-per-Unit-Length

The magnitude of the inductance-per-unit-length, L', is one of the most important differences between parallel-plate and co-axial electrode geometries. It is calculated by integrating the magnetic flux through a volume inclosed by the discharge. The inductance gradient for a parallel-plate thruster can be estimated by treating the electrodes as a single-turn infinite coil with a uniform field,

$$L'_{pp} \approx \mu_0 \frac{H}{W}. \tag{3.7}$$

For a co-axial GFPPT, the calculation can be carried out directly and no approximation is necessary assuming a planar current sheet,

$$L'_{co-ax} = \frac{\mu_0}{2\pi} \ln \frac{r_{out}}{r_{in}}. \tag{3.8}$$

As other authors[72] have pointed out, however, most commonly designed parallel-plate thrusters produce very non-uniform fields, and the fringing effects of finite-width electrodes must be taken into account. Using a conformal mapping technique to determine the electromagnetic fields in a parallel rail launcher, ref. [73] provides the necessary tabular data to determine the actual value of the inductance-per-unit-length for a given electrode aspect ratio. The graph in Fig. 3.3 shows the approximate L' value and the actual value L' for both parallel-plate and co-axial geometry which will be used for this study. The graph also
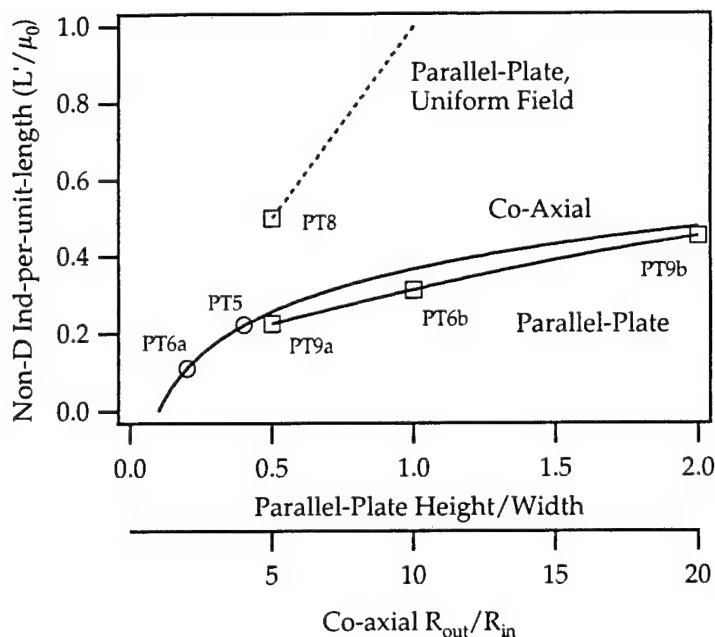
Figure 3.3: Normalized inductance gradient as a function of geometry for parallel-plate and co-axial electrodes.

provides a comparison of the L' values for all the GFPPTs tested here. The graph shows that the inductance-per-unit-length for a co-axial thruster and a parallel-plate thruster is similar if the former has a radius-ratio about ten times the height-to-width ratio of the latter. This is the case when comparing the simi-lar values of inductance-per-unit-length of PT5 with PT9a. In general, however, reasonable geometries for parallel-plate thrusters have a higher value of L' as is the case with most of the GFPPTs tested here as shown in Table 1.

3.4 Measured Performance

Performance of four different GFPPTs have been measured over various mass bits, energy levels, capacitance values, etc. to form an extensive data base that can be used to compare the performance of co-axial vs. parallel-plate electrode geometries. In these comparisons, the performance will be gauged by graphs of efficiency as a function of specific impulse. The thrust-to-power ratio is proportional to about one-fifth the ratio of efficiency to specific impulse. Many of the experimental protocols and methods for calculating performance from the measured quantities have been documented previously[5, 55] and will not be repeated here. In all the data presented here, the overall efficiency (as
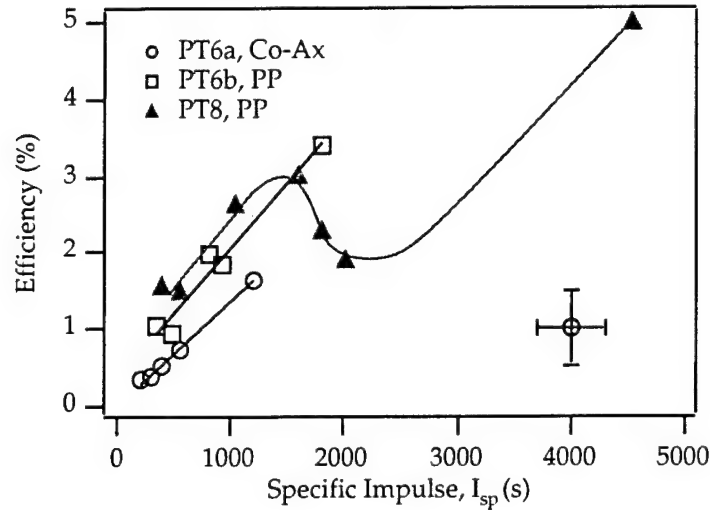
Figure 3.4: Efficiency vs. specific impulse for PT6 and PT8 with argon at various mass bits. All data shown is taken at 2 J per pulse using a 63 μF capacitor. A proportional error bar for the middle of this data set is also shown.

defined in Section 3.3) is used to compare the various GFPPT designs. Note that since the specific impulse calculation is also dependent on the propellant utilization efficiency, performance curves of overall efficiency vs. specific impulse will have the same form as those of thrust efficiency vs. exhaust velocity which are described by Eq. (3.4). Performance measurements of the quad thrusters, PT6-PT8, were conducted at NASA JPL while PT5 and PT9 were tested at EPPDyL.

3.4.1 PT6 and PT8 Performance

The performance of PT6 and PT8 was measured with both parallel-plate and co-axial electrodes using argon for propellant over many different mass bits. The discharge energy was kept constant at 2 J/pulse to form the performance database shown in Fig. 3.4.

All three thrusters can be compared at the highest mass bit values which correspond to specific impulse values between 0-1000 s. In this region, PT8 has the best efficiency and thrust-to-power ratio, however, not quite as much as expected due to the higher value of L'. PT8 has an inductance-per-unit-length about five times larger than PT6a (co-axial) but the efficiency is not even twice as large except at the lowest specific impulse values. Similarly, the performance of the parallel-plate configuration of PT6 does not show the expected factor of 1.9 improvement over the co-axial configuration. Near 1800 s, PT8 and PT6b have very similar performance even though PT8 has an L' value about

30% larger. At I_{sp} values greater than 2000 s (lowest mass bit values), PT8's performance drops and increases again in a form seen previously in ref. [5] where two modes of GFPPT operation were identified (see Section 3.4.2 for further discussion of this trend in the data).

It is suspected that wall losses and profile inefficiencies play a strong role in explaining why the performance of these thrusters did not scale with the square-root of inductance-per-unit-length as discussed in Section 3.5. Considering these performance measurements alone, however, the two parallel plate geometries did not meet up to expectations based on the increase in inductance-per-unit-length. Although the value of L' *does* seem to play a role in performance as the co-axial geometry (lowest L') had the smallest efficiency, another comparison of co-axial vs. parallel-plate geometries with similar inductance-per-unit-lengths should provide a more direct answer to this chapter's main question.

3.4.2   PT5 and PT9 Performance

The performance of PT5 has been fully documented in ref. [5] and only one set of conditions using 130 μF at 4 J/pulse will be used here to compare co-axial vs. parallel plate electrodes. The parallel-plate thruster, PT9, was designed to test the impact of inductance-per-unit-length on performance in a controlled manner. The smallest value of L' (PT9a) was made to be similar to that of PT5, about 2.8 nH/cm. The largest value of L' (PT9b) is about twice that of PT9a or PT5 and is predicted to have a higher performance by a factor of the square-root of two. Figure 3.5 shows the performance of PT5 and PT9 over a wide range of specific impulse (mass bit) values. As seen from the graph, the co-axial electrodes outperform or at least match the performance of the parallel-plate configurations even with a factor of two increase in L'. In fact, the parallel-plate thruster with the largest inductance-per-unit-length, PT9b, has the lowest value of efficiency out of all the thrusters with an $I_{sp} > 1000$ s. PT5 and PT9a have similar performance above 3000 s (mass bits ≤ 0.3 μg/pulse), however, the co-axial geometry of PT5 has much better performance than either of the parallel-plate geometries at specific impulse values below 2000 s. Again, other loss mechanisms may be playing a significant role in reducing the performance of the parallel plate thrusters as described in the next section of this chapter.

Examining the data sets further, there is a "hitch" present where the efficiency decreases and then increases again at about 1500 s for PT5 and PT8 with PT9a and PT9b having a similar yet smaller trend occurring near about 800 s. This phenomenon has yet to be fully explained, however, performance measurements from PT5 over a more wide range of capacitance values showed that this region marks the division between two modes of GFPPT operation. A possible explanation includes the transition between two types of acceleration mechanisms: electrothermal dominated acceleration at lower I_{sp} values where the efficiency is relatively constant and electromagnetically dominated acceleration at higher I_{sp} values where the efficiency varies linearly with the specific impulse. The explanation could also include a possible decrease in the current sheet's ability to sweep up the propellant effectively at higher exhaust velocities
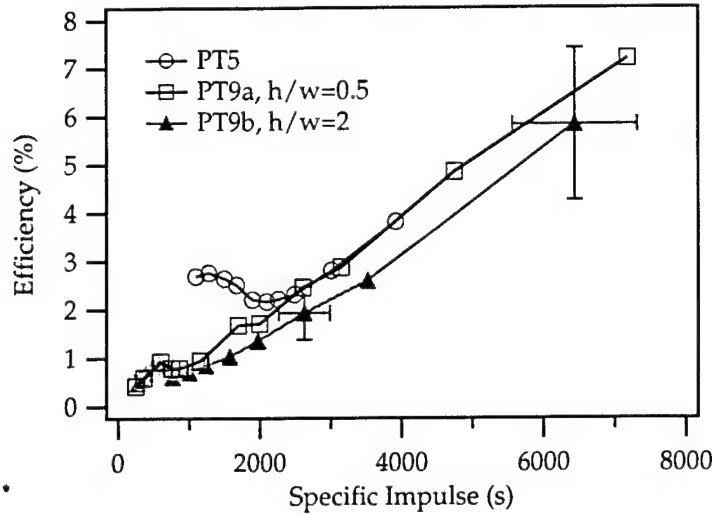
Figure 3.5: Efficiency vs. specific impulse for PT5 and PT9 with argon at various mass bits. All data shown is taken at 4 J per pulse using a 130 μF capacitor. Representative error bars of all the data sets at different specific impulse values are also shown.

(higher I_{sp}) and lower mass bits where gas dynamic pressures are low. Finally, at the highest velocities, it is very likely that the current sheet travels down the full extent of the electrodes before it can use all the energy stored in the capacitor. The full explanation could involve a combination of all these reasons and is under further investigation at EPPDyL.

3.5 Discussion

Although higher performance at similar values of inductance-per-unit-length could be considered to be the strongest argument for choosing co-axial electrodes over parallel plate electrodes, there are other factors which should be considered in this context. Among the most important of these issues are possible wall losses and non-uniform current sheet acceleration profiles present in both geometries.

3.5.1 Possible Wall Losses

Previous estimates of viscous stress in quasi-steady MPD thrusters[74, 75] have shown through order-of-magnitude arguments that it is not a significant loss mechanism at high powers. In GFPPTs, this same analysis shows this to be true near the beginning of the discharge when the current and voltage are large and the sheet velocity is relatively small. However, this is not true at later stages
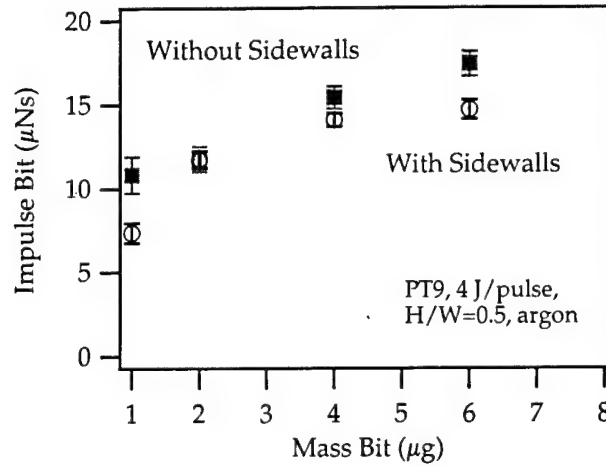
Figure 3.6: Effect of Pyrex side walls on performance as a function of mass bit for PT9 at 4J/pulse with 1" x 1/2" electrodes using argon.

when the Lorentz force has decayed and the gas velocity, temperature, and pressure are high. With longer electrodes, viscous losses could significantly influence the final velocity which could explain the discrepancies found in Section 3.4.2.

In an attempt to quantify this experimentally, PT9a was tested with and without Pyrex side walls. As shown if Fig. 3.6, the performance was *increased* when the Pyrex side walls were removed. Unfortunately in the tests without the side-walls at low mass bits, the arc was seen to periodically stretch out of the electrode volume and attach away from the electrodes. Since at low mass bits ($< \approx 1$ μg/pulse), the additional mass of erosion products from spurious arc attachments can significantly impact the performance, these data points are not shown in Fig. 3.6. In addition, it was felt that although higher performance is possible without the side walls, PT9 should use the Pyrex side walls to contain the discharge for all the data used in this chapter for comparison with other thrusters. In any case, the increase in impulse bit values at the higher mass bit conditions without side walls hints to the possible role of wall loses in limiting the performance that can be brought about by changing L'

3.5.2 Current Sheet Profile Losses

Current sheet profile losses can come in two different forms: a spatially non-uniform Lorentz Force acting on the current sheet, and a current sheet canting phenomenon seen in parallel plate thrusters that is currently under investigation at EPPDyL[52].
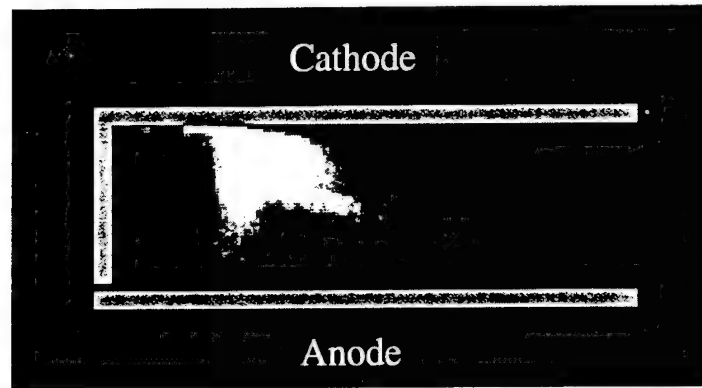
Figure 3.7: Imacon Fast Framing Picture of PT9 discharge (270 μF, 4 J/pulse, 1 μg/pulse) at 1.8 μs after initiation with a 400 ns exposure. A narrow 488 nm line filter was used to observe only argon ion emission.

Non-uniform Lorentz force. For coaxial electrode geometry, the current density and hence the magnetic field are both proportional to $1/r$ giving a lorentz force that increases rapidly at the center electrode as $1/r^2$. This non-uniformity would suggest that the current sheet runs along the center electrode very fast forming a cone-like structure which accelerates the gas in a non-axial manner. In more recent co-axial SRL-GFPPT designs an attempt is made to balance this non-uniform force by injecting more propellant near the center electrode. For parallel-plate thrusters, the Lorentz-force is expected to be more axially-directed at the center-line of the electrodes due to the finite width of the electrodes and the fringing magnetic field.

Current sheet canting. The other type of profile loss has been discovered by viewing filtered Imacon fast-framing camera pictures of parallel-plate discharges on micro-second time scales. As shown in Fig. 3.7, a picture of the current sheet shows a bifurcation and canting with the leading edge always moving along the anode first. If this emission represents the current conduction location, then the acceleration will not be directed axially and performance losses will result. It is entirely possible that this same canting is occurring in co-axial thrusters where a side-view of the discharge is difficult to obtain. If this is true, then for the co-axial SRL-GFPPT designs where the center electrode is the anode, there could be an even more elongated current sheet and higher profile losses. To measure this effect, future work at EPPDyL will include reversing the polarity of one of the co-axial thrusters to see if the two non-uniform profiles can counter-act each other. For parallel-plate thrusters, work is continuing at EPPDyL to understand and, if possible, eventually counteract this canting which could also eventually improve parallel-plate performance.

It should also be noted that parallel-plate geometries allow the application

of external magnetic fields that would augment the self-induced field and possibly increase performance as has been demonstrated in APPTs[76]. Due to the geometry of the electrodes, only a parallel-plate thruster can use this technique effectively. Future performance measurements at EPPDyL will include the effects of applied magnetic fields on parallel-plate geometries.

3.6   Summary and Conclusions

It has been shown through an analytic model of electromagnetic acceleration that two factors effect the thrust performance directly: capacitance and inductance-per-unit-length. Although the performance scaling with the square-root of capacitance has been demonstrated experimentally, raising the capacitance to an arbitrarily high level is not beneficial as we have shown that the propellant utilization efficiency decreases at higher values of capacitance. Inductance-per-unit-length then becomes the next best parameter to maximize, however, measured performance data shows that this is not necessarily the case. In fact, although L' values are typically higher in parallel plate geometries, the trends in the data show that co-axial electrodes with moderate values of L' have a higher efficiency and thrust-to-power ratio over many similar operational conditions. Although there is evidence that inductance-per-unit-length does play a role in performance, it is only apparent as long as other mechanisms such as viscous wall losses and non-uniform current sheet profiles do not dominate the performance.

Chapter 4

Effects of Ignition on Discharge Symmetry

4.1 Introduction

Both ablative pulsed plasma thrusters (APPTs) and Gas-fed pulsed plasma thrusters (GFPPTs) use high voltage "spark plug" ignitors to ionize a small fraction of propellant and begin the current sheet formation. In GFPPTs, it has been shown that the initial gas loading profile is crucial to the effectiveness of the initiation and acceleration phases of the discharge pulse in terms of both a uniform breakdown and the propellant accumulation or "sweeping" process[22, 21, 25]. Different designs of ignitors have been tested in the past by measuring the voltage and current waveforms to infer the energy efficiency[69] but few images of the initiation history of a GFPPT discharge exist in the literature.

Recently, a family of high-repetition rate co-axial geometry GFPPTs have been introduced and tested by Science Research Labs, Inc. and Princeton University[53, 44]. The high-repetition rate allows a propellant utilization of nearly 100% by stringing multiple pulses together into a tight burst. The short time between pulses, 100-300μs, however, makes tailoring the initial mass distribution between each pulse difficult. In addition, the electronics required to uniformly breakdown the gas throughout the inter-electrode volume are not trivial. Studies into the effects of propellant distribution and initiation circuitry on the current sheet formation are ongoing at Princeton with the use of a new diagnostic tool: the Imacon fast-framing camera. This tool allows the current sheet formation and propagation to be visualized at rates up to 20 MHz for a single pulse. A schematic of the entire experiment is shown in figure 2.10.

This chapter will focus on the use of the Imacon camera to visualize and record the discharge dynamics while varying the thruster and discharge ignition set-up. First, the various configurations of the SRL-GFPPTs will be described including electrode geometry, spark plug type and placement, propellant distribution, and thruster power conditioning. Next, the Imacon camera will be

115

discussed in more detail with sample data obtained from recent experiments. The effect of changing the discharge initiation circuitry and the propellant injection manifold will be discussed in terms of the formation and propagation of a symmetric and uniform current sheet. Finally, the entire set of results will be discussed and an overview of future research goals will be presented.

4.2 The Fourth and Fifth Generation SRL Gas-Fed PPTs

The SRL4-GFPPT has been introduced before in refs [53, 44], therefore, only the most important points of the thruster construction and operation will be highlighted here. A schematic of the SRL4-GFPPT is shown in figure 4.1.
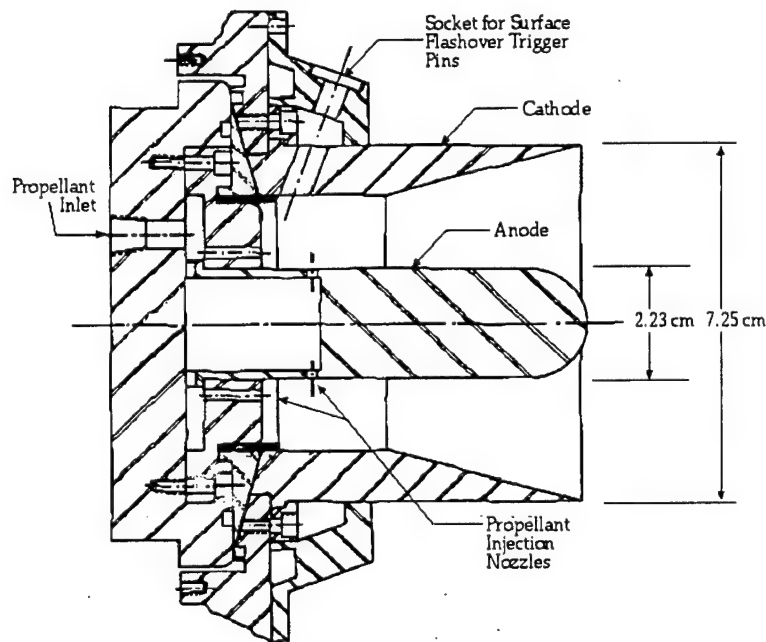

Figure 4.1: Schematic of the SRL4-GFPPT.

The fifth generation design is very similar to the previous version but with a larger outer electrode radius. The SRL5-GFPPT has gone through four iterations (labeled here simply a, b, c, and d) including changes in outer electrode design, spark plug type and placement, as well as propellant distribution. These iterations will be discussed in the following sections.

4.2.1 Outer Electrode Construction and Spark Plug Manifold

Both versions of the GFPPT have stainless steel, co-axial electrodes with a slight expansion near the exit. The outer to inner electrode radius ratio is 3.25 for the SRL4-GFPPT and a little more than 4 for the SRL5-GFPPT i' (all iterations) with both having about the same absolute inner electrode radius.

The first iteration of SRL5-GFPPT, now labeled SRL5a-GFPPT, had a solid outer electrode with eight large surface flash-over spark plugs. The ignitors were mounted evenly around the outer electrode in a propellant manifold. Similar to the design of the fourth generation thruster, the manifold provides a small amount of gas flow over the surface of each of the spark plugs before, during, and after the discharge.

The second iteration was the largest change in outer electrode design. SRL5b-GFPPT had an outer electrode constructed of 24 evenly spaced rods. mounted to the top of the spark plug manifold. These rod electrodes were used to allow visualization of the current sheet propagation from a side view of the thruster while still providing a conducting surface for the discharge current.

Iteration 5c went back to a solid outer electrode but used a different, smaller type of semi-conductor spark plug (described in the next section) that did not require direct propellant flow to work effectively. For that reason, the spark plug manifold was removed and the spark plugs were mounted directly to the outer electrode.

The SRL5d-GFPPT has the same outer electrode configuration as iteration 5c.

4.2.2 Spark Plug Type and Placement

The SRL5a and 5b-GFPPT used the same type of large surface flash-over spark plugs that were originally used in the SRL4-GFPPT. With a larger outer electrode radius, however, the SRL5a and 5b-GFPPT used eight ignitors where the SRL4-GFPPT used only four. In the third and fourth iteration of the SRL5-GFPPT, the type of spark plug was changed to the same same semi-conductor spark gap ignitor used in the LES 8/9 APPT. These ignitors require a lower break down voltage without any extra propellant mass flow. The breakdown voltage for normal operation of the smaller semi-conductor spark-gap ignitor is ≈ 1000 V which is much smaller than what was required for the original larger surface breakdown plugs, ≈ 5000 V. The SRL5c-GFPPT also went through changes in the discharge initiation circuitry to try to balance the energy distributed between each plug. All the spark plugs in each SRL-GFPPT are connected in parallel to a discharge initiation capacitor that is charged once for each pulse. More details on changes to the discharge initiation circuitry will be provided in section 4.6.

4.2.3 Propellant Distribution

In all the SRL-GFPPT designs the propellant flow is controlled by a solenoid valve and a sonic orifice connected to the main propellant line. A gas feed line connects the solenoid valve to a small reservoir behind the back-plate of the thruster. As shown in figure 4.1, the inlet to the reservoir is slightly off center to insure that all the propellant doesn't leave the reservoir through the center electrode. Both the back-plate of the thruster and the center electrode contain propellant injectors that attempt to provide a 1/r gas density profile before each pulse. After examining a series of asymmetric Imacon photos of SRL5c-GFPPT and the condition of the propellant feeding system, the off-center nature of the propellant inlet was questioned. Suspected to be a possible cause of the asymmetries, a new path for gas flow to the other side of the reservoir was constructed and tested to create the last iteration used in this chapter, the SRL5d-GFPPT.

4.2.4 Thruster Power Conditioning

All versions and iterations of the SRL-GFPPT used the same solid-state control modulator and could be fired at energy levels between 3-10 J at rates up to 4 kHz. Typically six pulses were fired per burst, however, this number can be set to higher levels depending on the desired thrust level. The discharge initiation power is produced by a separate high voltage supply. On every version of the SRL-GFPPT so far, the inner electrode is at a positive potential (anode) and the outer electrode is held at ground potential (cathode). The main discharge capacitors are mounted directly to the electrodes and the gaps between the conductors are kept at a minimum to reduce the initial inductance to 5-10 nH.

The capacitance for each of the configurations is provided here. In general, all the SRL thrusters use modular capacitor boards with typical increments of 45-90 μF. For the data presented in this chapter, the SRL4-GFPPT has a total capacitance of either 180 or 270 μF; the SRL5a and 5b-GFPPT used capacitors with a lower internal resistance value (however, a larger specific volume) that provided a total of 90 μF; the SRL5c and 5d-GFPPT returned to the original, smaller volume capacitor type with a total of 270 μF.

4.3 Imaging the Discharge Initiation and Propagation

One of the key features for understanding the dynamics and symmetry of a GFPPT discharge is visualization of the plasma itself. It has been shown in previous work[77] with co-axial, quasi-steady pulsed plasma thrusters that the luminous patterns in the arc discharge are a good indication of magnetic field and current conduction symmetry. In this section, the technique for visually capturing the development of the discharge including the ignition phase will be presented.

4.3.1 The Imacon 20 Megahertz Fast Framing Camera

The Imacon fast-framing camera allows multiple black and white (grayscale) images to be taken on one 3.25" by 4.25" polaroid photo at rates of either 2×10^7 or 5×10^5 frames per second depending on the selected oscillator module. The camera is triggered from a pulse delay generator which is in turn triggered off the high voltage leads to the spark plugs themselves. Since there is slight delay in the high voltage applied to the ignitors and the actual breakdown, the pulse delay generator can be set to activate the camera just before the discharge begins. In all references to time in this chapter, $t = 0$ occurs when the breakdown actually begins and current begins to flow.

4.3.2 Output Picture Description

The Imacon camera uses a photo multiplier tube and a cathode ray tube to project the subject image onto a phosphorus screen. This image can be viewed directly, or a polaroid camera can be set up and exposed to the phosphor image. When the camera is activated, the thruster image will jump from the bottom to top of the screen and back again after each exposure as shown in figure 4.2. Since there is a limited screen area, the number of images one photograph can
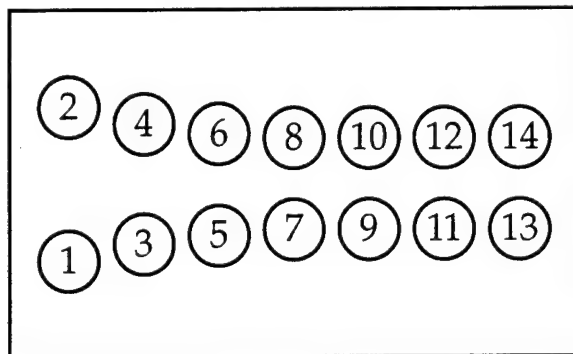

Figure 4.2: Schematic of photographic output from the Imacon fast-framing camera showing the order in which the exposures are taken.

capture is inversely related to the area and resolution of the desired image. The area of the image on the screen is controlled by the focal length of the imaging lens and a small screening card that can be placed inside the Imacon camera. The number of exposures captured on one screen can be set manually and ranges between 4 and 32. For the GFPPT experiments, the 20 MHz oscillator module was used to image approximately 16 small images of the thruster covering a total of 0.8 μs, and the 500 kHz oscillator module was used to image approximately 6 larger images of the thruster for a total of 12 μs. These two configurations along with a variable delay timing allowed all phases of the discharge to be visualized effectively.

Along with the visual output, the Imacon camera has an electrical monitor line that pulses when the camera takes a picture. In coordination with voltage and current data saved on a high sampling rate digital oscilloscope, see figure 2.10, the pictures can be placed in the correct time frame of the discharge. A drawing demonstrating this concept is shown in figure 4.3.
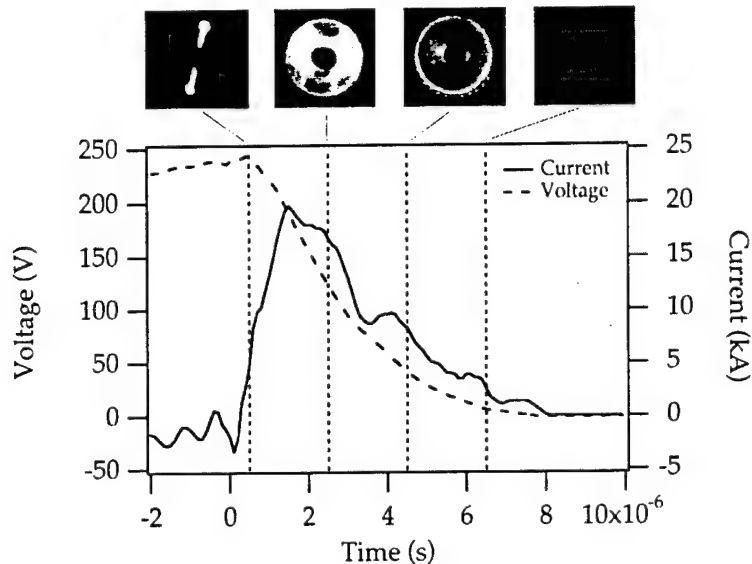

Figure 4.3: Chopped images from a typical Imacon photographic output (5×10^5 frames per second, 0.5 μs delay) corresponding to the voltage and current traces taken at the same time. Images show the initiation occurring at two spark plugs in the SRL5b-GFPPT firing at 5 J/pulse with a 0.5 μg argon mass bit.

4.4 Asymmetric Ignition and Discharge Data from the SRL4-GFPPT

Until recently, the discharge of the SRL4-GFPPT was thought to be uniform during every pulse. As shown in figure 4.4, this is not the case as one pulse displays a symmetrical break-down near all four ignitors, and the other appears to have only two ignitors working effectively. The top picture shows a uniform initiation, and the bottom picture shows a two point, asymmetric initiation. After viewing many discharges, the thruster ignition is considered sporadic. In most cases, after a large number of pulses, the same one or two spark plugs would fire reliably. Only on rare occasions did all four ignitors provide a symmetric discharge routinely.
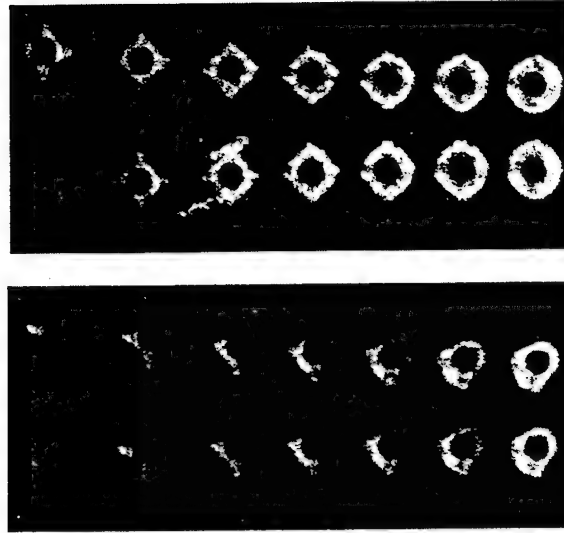
Figure 4.4: The 270 μF SRL4-GFPPT firing at 5 J/pulse with a 0.5 μg argon mass bit. Framing rate: 50 ns per image with a 0.8 μs delay on both.

As shown in the longer duration photos in figure 4.5, the top picture shows a uniform initiation while the middle picture shows a two point, asymmetric initiation, and the bottom picture shows a two point, symmetric initiation. When all four ignitors work well, the discharge seems to continue to propagate symmetrically. Even when only two oppositely oriented plugs fire, the discharge seems to recover its uniform, symmetric nature. When two adjacent plugs initiate the discharge, however, it appears that the discharge remains asymmetric for its entire lifetime.

4.5   Ignition Data from the SRL5b-GFPPT

The SRL5a and 5b-GFPPT showed even more random behavior, especially during the first few firings after the experiment had been dormant for a while. Figure 4.6 shows the best and the worst operation of the SRL5b-GFPPT. The top picture shows a uniform initiation with four and then eight ignition points, while the bottom picture shows a one point, asymmetric initiation. From these pictures and the many pulses where only one (but not always the same one) ignitor performed adequately, the conclusion was reached that the larger distance between the electrodes made obtaining a uniform discharge more difficult.

As an interesting visualization of the propagation of the current sheet, the SRL5b-GFPPT was fitted with rod outer electrodes and photographed from the side. As shown in figure 4.7, the luminous region appears to be diffuse in nature although there is clearly motion of the extent of the plasma. The rod electrodes

mounted on the spark plug manifold are visible as the discharge moves past the electrodes, and a "glow" remains. The discharge looks somewhat non-uniform and at an angle with the discharge near the center electrode further along than the rest. Knowing the length of the rode electrodes to be 5 cm, and the duration between the exposures to be 2 μs, we can calculate a rough velocity to be 25 km/s. Also, it seems as if the bulk of the discharge has left the electrodes by the fourth frame. At this point, there is still charge on the capacitor, however, and the electrodes seem to glow slightly. This glow was noticed in many pictures after the discharge seemed to have reached the extent of the electrodes.

4.6 Effect of Changes to the Discharge Initiation Circuitry and Propellant Distribution

After the large surface flash-over ignitors were found to be an unreliable method for discharge initiation, it was decided to switch to four of the smaller semi-conductor type plugs used in the LES 8/9 APPT. As mentioned previously, these ignitors do not require a propellant flow or high voltage source to work well. In fact, immediately upon use, the plugs demonstrated a repeatability that was not seen in the other type of ignitor. Although only two plugs provided an adequate discharge initiation source, it was the same two ignitors that worked every time.

In an attempt to fix this problem, a 3000 V, 2.7 μF capacitor was placed in series with the anode of each spark plug. Since the spark plugs were connected in parallel, this was postulated as a way to distribute the discharge initiation capacitor energy in a more uniform manner. Upon testing, it was seen that still only two spark plugs operated reliably. Although the spark plugs had been rotated to a new position on the outer electrode, the same ignitors did not work routinely. The spark plugs in the same sockets as the previously working ignitors, however, provided the same reliable performance.

At that point, it was decided to investigate the mass distribution inside the SRL5c-GFPPT. After examining the Imacon pictures and the condition of individual ignitors, it was determined that the reliably working spark plugs were physically aligned with the off-center propellant inlet. As an attempt to bring about symmetric discharge initiation, another propellant inlet was constructed on the opposite side of the reservoir. The effect of this modification is shown in figure 4.8. Although there is still an asymmetric discharge, now three ignitors seem to be working effectively. There is no correlation, however, yet discovered between the new inlet configuration and the ignitor that remains dormant as both the inlets to the reservoir are located 45 degrees away from any ignitor.

4.7 Summary and Comments

Images of the discharge initiation and propagation have been taken for a variety of thruster geometries and ignitor configurations. It was shown that discharge

initiation plays a key role in the symmetry of the current sheet. Lower frequency exposures show that symmetric ignitions maintain a uniform nature while asymmetric ignitions lead to non-uniform, off-center luminous patterns. Finally, the addition of capacitors in series with the ignitors and the modification of the propellant feed system in the latest iteration of the SRL5-GFPPT seemed to have a beneficial effect on the number of ignitors that work effectively.
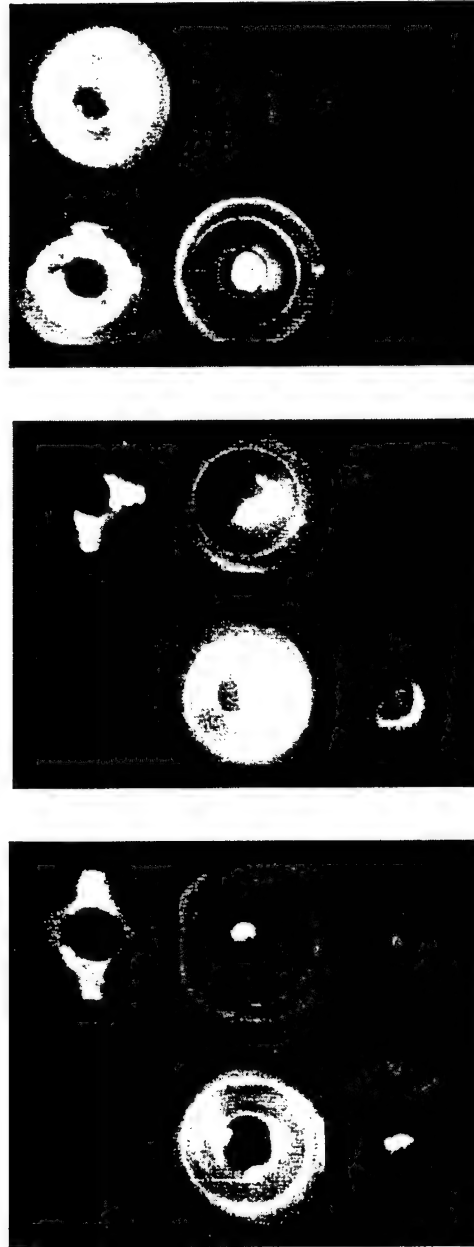
Figure 4.5: The 180 μF SRL4-GFPPT firing at 8 and 5 J/pulse with a 1.0 μg argon mass bit. The top picture shows an 8 J pulse, and the middle and bottom picture show a 5 J pulse. Framing rate: 2 μs per image with delays of 1.2 μs, -1.0 μs, and -1.1 μs for the top, middle, and bottom pictures, respectively. The delay on the middle and bottom pictures are negative because the first frame is taken before the discharge begins and is, therefore, blank.
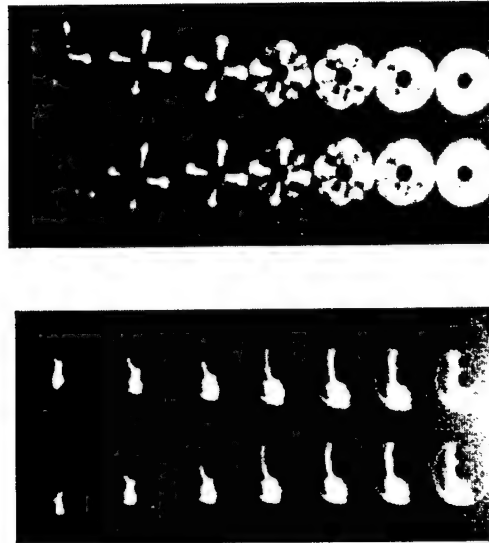
Figure 4.6: The SRL5b-GFPPT firing at 8 J/pulse with a 1.0 μg argon mass bit. Framing rate: 50 ns per image with approximately a 0.5 μs delay on both.

Figure 4.7: Side view of the SRL5b-GFPPT firing at 8 J/pulse with a 1.0 μg argon mass bit. Framing rate: 2 μs per image with approximately a -0.5μs delay (first frame blank).
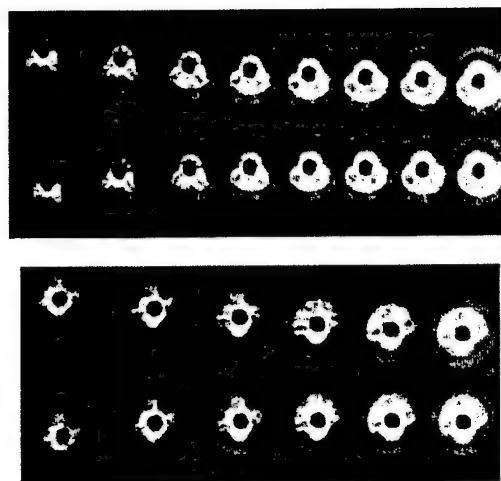
Figure 4.8: The top picture shows the SRL5c-GFPPT and the bottom picture shows the SRL5d-GFPPT with the propellant feeding system modification. Both thrusters are being fired at 5 J/pulse and with a 1.0 μg argon mass bit. Framing rate: 50 ns per image with a 0.8 μs delay on both.

Chapter 5

Performance Scaling Laws

5.1   Introduction

With the present focus on power-limited spacecraft, there is a need for an experimentally verified set of performance scaling relations for low energy GFPPTs. For the scaling laws to be useful, they should be simple and apply over a wide range of operating conditions and electrode configurations. They should also contain the main character of the acceleration physics while maintaining a good degree of accuracy so that they can be extended to low (or high) energy GFPPTs.

To accomplish this task, a number of previous attempts at deriving scaling laws were made (see Refs. [1] and [36] for example) and a number of performance studies on various thruster designs were conducted (see Refs. [20] and [29] for example). Yet, possibly because of the complex nature of the plasma acceleration in GFPPTs and the multitude of concurrent design changes at the time, the models did not accurately describe the exact performance scaling found in experimental measurements.

At Princeton's Electric Propulsion and Plasma Dynamics Lab (EPPDyL) a GFPPT has been designed in cooperation with Science Research Laboratory, Inc. (SRL) to explore performance scaling (see Refs. [53, 45, 10, 5, 57]). Using modern solid-state pulse forming technology to group series of low energy (<10 J) pulses together in bursts, the propellant mass utilization efficiency is maintained near 100% while eliminating the need for an ultra-fast valve with exceptional lifetime characteristics. The solid-state nature of the power conditioner also permits the system to be more compact and reliable than the previous single-pulse designs. In addition, the modular nature of the GFPPTs themselves has allowed testing of multiple iterations to examine the effects of changing various design parameters on performance. Simply stated, our goals concerning GFPPT performance scaling have been to:

- Derive universal scaling laws for GFPPT performance

- Experimentally verify the validity and extent of applicability of these laws

- Obtain physical insight into the basic mechanisms that impact the performance of GFPPTs

- Extend the understanding of how to build higher-performance devices and how to scale them to low (or high energies) while maintaining their high performance.

This chapter describes the final results of the performance scaling studies, including both modeling and performance measurements of two GFPPT designs. First, the analytical model will be developed and the GFPPT characteristic velocity and the performance scaling number will be defined. Next, the performance measurements from two GFPPT designs with varying geometry, capacitance, energy, and mass bit will be presented. Finally, the measurements will be presented in terms of the GFPPT characteristic velocity and the performance scaling number to check the validity of the model.

5.2 Derivation of Performance Scaling Relations

As well known in PPT research, an effective circuit model can offer much insight into the discharge dynamics. Depending on the capacitance, C, initial inductance, L_0, inductance-per-unit-length, L', total resistance (including both the hardware and the effective plasma resistance), R, discharge energy, E, and the mass loading (shown schematically in 5.1), the discharge current has a damped oscillatory response with varying character: underdamped, critically damped, or overdamped. The circuit model is usually combined with a "snowplow" model for mass accumulation and numerically integrated to provide a solution that predicts performance at one operating condition. This technique has been used by these authors [45] and others [1, 36, 29, 64] to span possible operating conditions. Discovering analytical performance scaling relations from the numerical solutions of these non-linear differential equations, however, has proven difficult. Others have assumed a fixed inductance and a constant mass [30] or a slightly increasing mass from electrode erosion [37] to decouple the equations and provide analytical solutions. The scaling relations produced by these techniques, however, only apply to a very limited case of GFPPTs where the initial inductance and mass dominate the circuit response.

For the GFPPTs designed and tested by SRL and EPPDyL, the current waveform is essentially critically damped due to the low inductance (< 10 nH) and large capacitance ($> 100\mu$F) of the energy storage bank. Current waveforms measured with higher mass bits have a slight underdamped quality while lower mass bits can be slightly overdamped. With this understanding, we will focus on a "critical resistance ratio,"

$$\psi \equiv \frac{R}{2}\sqrt{\frac{C}{L_0}}, \tag{5.1}$$

value near unity. As will be shown, this allows us to relax the assumptions of
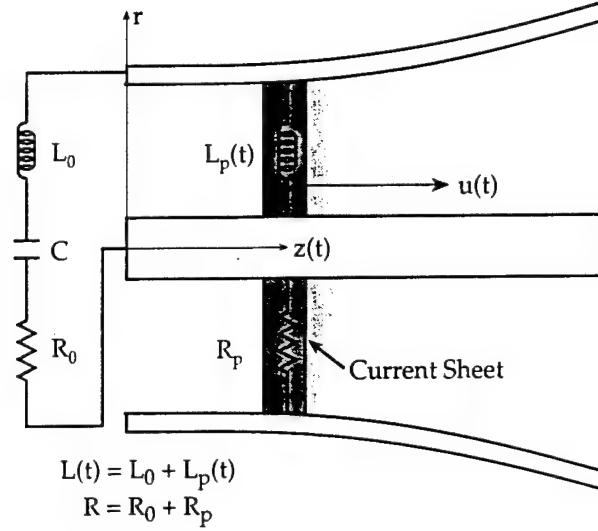
Figure 5.1: Schematic drawing of GFPPT discharge including elements used for the circuit model.

fixed inductance and mass used in Refs. [30, 37] and derive useful, analytical scaling relations for a more realistic model.

First, we expand Kirchhoff's equation for the effective discharge circuit,

$$V_0 = \frac{1}{C} \int_0^t J dt^* + (R + \dot{L})J + L\dot{J}, \qquad (5.2)$$

where V_0 is the initial voltage on the capacitor and J is the total current flowing through the circuit. Solutions to this equation yield current waveforms, $J(t)$, with a character that depends on the changing inductance due to the motion of the current sheet. The total inductance at any given time is related to the position of the current sheet,

$$L = L' z + L_0, \qquad (5.3)$$

where z is the location of the current sheet down the length of the electrodes, and the value of L' depends on the electrode geometry. The momentum equation includes the self-induced Lorentz force in the axial direction,

$$\frac{d}{dt}(mu) = \frac{1}{2}L' J^2, \qquad (5.4)$$

where m is the instantaneous amount of mass contained in the current sheet moving at a velocity u.

Next, we split the discharge into two segments: before the peak current is reached at $t = t_{peak}$, and from that time until the current reaches zero, $t = t_{final}$.

During each segment, we will assume that the current is *linearly* proportional to time. At the beginning of each segment, the values of $L(t), V(t), R$, and C will be used to determine the slope of the current waveform for the entire segment.
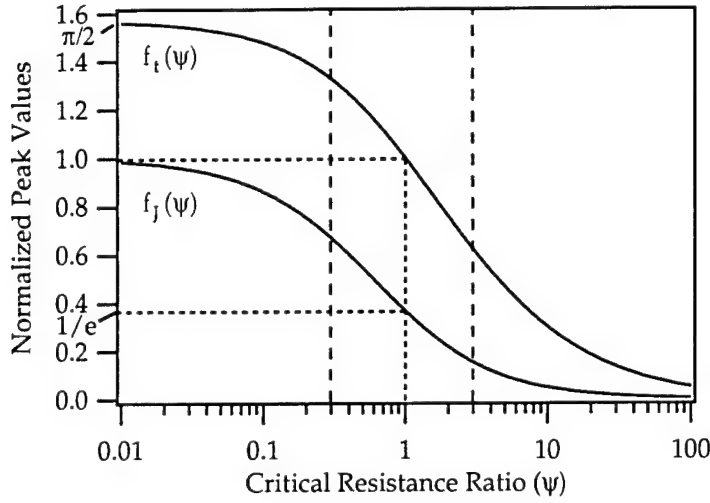

Figure 5.2: Normalized peak functions, $f_J(\psi)$ and $f_t(\psi)$, as a function of the critical resistance ratio, ψ. Values of the functions at $\psi = 1$ are shown by horizontal dashed lines. The range of ψ of interest to this study is $0.3 \leq \psi \leq 3$ as shown by the vertical dashed lines.

In the first segment, the slope of the current waveform is determined by the initial values of the inductance, L_0, and voltage, V_0, along with the fixed values of capacitance, C, and resistance, R. With these assumptions, the solution to Eqs. 5.2 and 5.4 has been given in Ref. [1] as,

$$J = \frac{V_0}{\omega L_0} e^{-(R/2L_0)t} \sin(\omega t), \tag{5.5}$$

where the natural frequency, ω,

$$\omega = \sqrt{\frac{1}{L_0 C} - \frac{R^2}{4L_0^2}} = \sqrt{\frac{1 - \psi^2}{L_0 C}}. \tag{5.6}$$

The peak current and the time at which it occurs can be found from this solution in terms of ψ,

$$J_{peak} = V_0 \sqrt{\frac{C}{L_0}} f_J(\psi), \tag{5.7}$$

$$f_J(\psi) \equiv e^{-\left(\frac{\psi}{\sqrt{1-\psi^2}} \sin^{-1}(\sqrt{1-\psi^2})\right)}, \tag{5.8}$$

$$t_{peak} = \sqrt{L_0 C}\, f_t(\psi), \tag{5.9}$$

$$f_t(\psi) \equiv \left(\frac{1}{\sqrt{1-\psi^2}} \sin^{-1}(\sqrt{1-\psi^2}) \right), \tag{5.10}$$

where $f_J(\psi)$ and $f_t(\psi)$ are designated as the "normalized peak functions". These two relations are shown as functions of ψ in Fig. 5.2 with exact values of the functions at $\psi = 1$ highlighted. The slope of the current in the first segment of the discharge is then simply J_{peak}/t_{peak},

$$J(t)|_0^{t_{peak}} = \frac{V_0}{L_0} \frac{f_J(\psi)}{f_t(\psi)}\, t. \tag{5.11}$$

In the next segment, our assumption of a close to critically damped waveform is very important in determining the correct slope of the current waveform approximation. For the critically damped case, the slope is related to the increasing inductance and exponentially decaying nature of the actual current waveform. In this case, we will assume that the final slope is related to the total change in inductance, ΔL, by a factor Λ,

$$\Lambda \equiv \frac{L_f}{L_0} = 1 + \frac{\Delta L}{L_0}, \tag{5.12}$$

where L_f is the final inductance of the effective discharge circuit when the current sheet has reached the end of the electrodes, $L_f = L' \ell_{electrodes}$. The second segment of the current waveform is then given by,

$$J(t)|_{t_{peak}}^{t_{final}} = \frac{V_0}{\Lambda} \sqrt{\frac{C}{L_0}}\, f_J(\psi) \times$$
$$\left[\Lambda + f_J(\psi) f_t(\psi) - f_J(\psi) \frac{t}{\sqrt{L_0 C}} \right]. \tag{5.13}$$

The entire model for the current is shown with a measured current waveform from PT9 in Fig. 5.3 using the measured parameters of $L_0 = 10$ nH, $C = 130\ \mu$F, and $V_0 = 242$ V. The approximate value of the inductance change, $\Lambda \approx 1.5$, is found by assuming that the current sheet reaches the end of the electrodes when the capacitor is fully drained. The model is shown to agree well with this current trace and the thruster parameters assuming $\psi \approx 1$.

As long as the effective resistance of the circuit does not change significantly during the discharge, i.e. ψ is constant, then the integral of J^2 can be evaluated in a straight-forward manner,

$$\int_0^{t_{final}} J^2 dt = \frac{2}{3} E \sqrt{\frac{C}{L_0}} \left[f_J^2(\psi) f_t(\psi) + f_J(\psi) \Lambda \right]. \tag{5.14}$$

Using Eqs. 5.8 and 5.10 to estimate the normalized peak functions for $0.3 \leq \psi \leq 3$,

$$\int_0^{t_{final}} J^2 dt = \frac{2}{3} E \sqrt{\frac{C}{L_0}} \left[\frac{\pi}{2} e^{-\sqrt{6\psi}} + \Lambda e^{-\sqrt{\psi}} \right]. \tag{5.15}$$

$$J = \frac{V_0}{\Lambda}\sqrt{\frac{C}{L_0}}f_J(\psi)\left[\Lambda + f_J(\psi)f_t(\psi) - f_J(\psi)\frac{t}{\sqrt{L_0 C}}\right]$$

$$J = \frac{V_0}{L_0}\frac{f_J(\psi)}{f_t(\psi)}t$$

Measured
Current

Current (kA)

Time (μs)

Figure 5.3: Variable element model for the current of a GFPPT discharge compared to a measured current trace from PT9: 4 J per pulse, 2.0 μg argon, 130 μF, 1" × 1" electrodes.

$f_J(\psi)$

$\exp(-\psi^{1/2})$

$\pi/2\ \exp(-(6\psi)^{1/2})$

$f_J^2(\psi)\ f_t(\psi)$

Normalized Peak Values

Critical Resistance Ratio (ψ)

Figure 5.4: Approximations (dashed lines) to the normalized peak functions $f_J(\psi)$ and $f_J^2(\psi)$ (solid lines).

Theses approximations are shown in Fig. 5.4 to be in good order of magnitude agreement with the actual values of the normalized peak functions over the intended range of ψ, especially near $\psi = 1$. Now using this approximation to determine the impulse, we integrate the momentum equation (Eq. 5.4) to get the impulse bit, I_{bit},

$$I_{bit} = \int_0^{t_{final}} \left[\frac{d}{dt}(mu) \right] dt, \tag{5.16}$$

$$= \frac{1}{2} L' \int_0^{t_{final}} J^2 dt, \tag{5.17}$$

$$= \frac{1}{3} EL' \sqrt{\frac{C}{L_0}} \left[\frac{\pi}{2} e^{-\sqrt{6\psi}} + \Lambda e^{-\sqrt{\psi}} \right]. \tag{5.18}$$
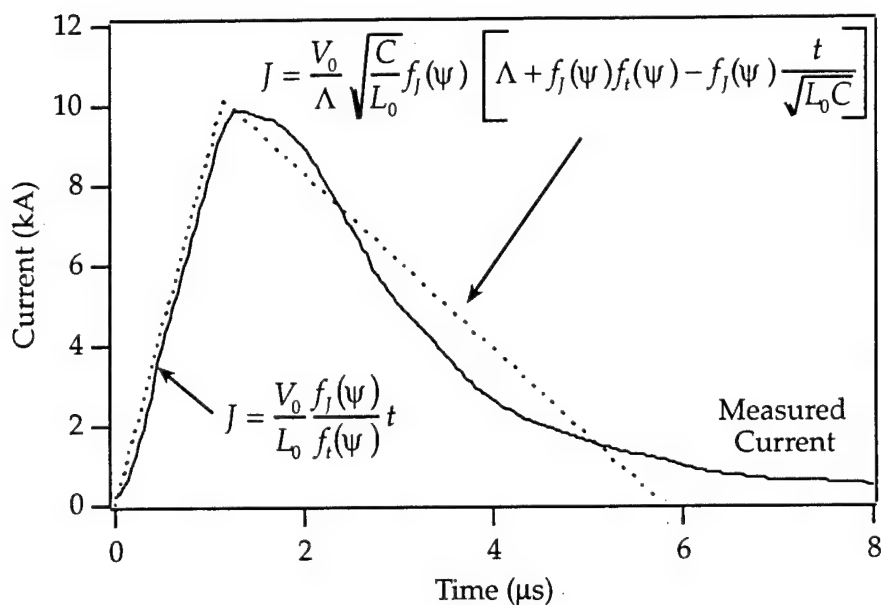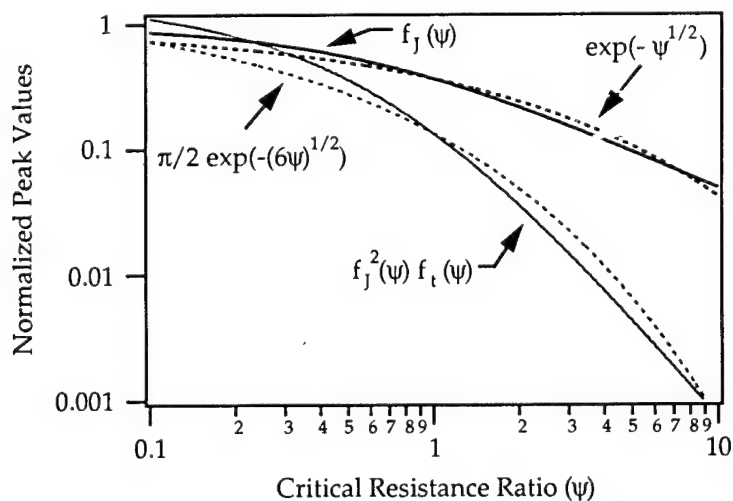
Note that the *impulse* does not depend on how the propellant was accumulated. We have made no assumption of a constant mass in exchange for knowing only the exit conditions of the discharge. The trajectory of the current sheet during the discharge cannot be found without knowing the mass distribution. Although the mass distribution does not determine the impulse, it does determine the amount of *energy* required to accelerate the entire mass down the length of the electrodes to the exit velocity. This, in turn, effects the efficiency.

There is still one unknown in Eq. 5.18: Λ. To determine Λ, we add another constraint that the integral of the current over the discharge time simply equal the initial charge on the capacitor, CV_0. This implies that the capacitor voltage at the end of the discharge is zero and that current no longer flows after t_{final}. Once again, we use Eqs. 5.11 and 5.13 to model the discharge current waveform and we find that,

$$\Lambda = 1 - f_t(\psi) f_J(\psi). \tag{5.19}$$

Using this relation, we can simplify the expression for the impulse bit,

$$I_{bit} = \frac{1}{3} EL' \sqrt{\frac{C}{L_0}} \, e^{-\sqrt{\psi}}. \tag{5.20}$$

Defining the exhaust velocity as,

$$u_e \equiv \frac{I_{bit}}{m_{bit}}, \tag{5.21}$$

The thruster efficiency, η_t, is then,

$$\eta_t \equiv \frac{I_{bit}^2}{2m_{bit}E}, \tag{5.22}$$

$$= \frac{1}{6} L' \sqrt{\frac{C}{L_0}} \, u_e \, e^{-\sqrt{\psi}}, \tag{5.23}$$

$$= \frac{u_e}{U} e^{-\sqrt{\psi}}, \tag{5.24}$$

$$\propto \chi, \tag{5.25}$$

where we have introduced the GFPPT characteristic velocity, U, as,

$$U \equiv \frac{6}{L'}\sqrt{\frac{L_0}{C}}, \tag{5.26}$$

and the GFPPT performance scaling number, χ, as

$$\chi \equiv \frac{u_e}{U}. \tag{5.27}$$

Note that if the total resistance in the circuit is zero ($\psi = 0$), then the maximum efficiency is reached when $u_e = U$ and $\chi = 1$. In this respect, the GFPPT characteristic velocity is the maximum obtainable exhaust velocity if there are no resistive losses in the complete discharge circuit. If $\psi > 0$, then the maximum exhaust velocity can be larger than U and χ can be greater than unity. The GFPPT characteristic velocity is only a function of the driving circuit and the electrode geometry making it *uniquely determined for each GFPPT design*.

The performance scaling number is a non-dimensional parameter that can be used to display performance measurements and check the validity of Eq. 5.25. Similarly, the non-dimensional impulse-to-energy ratio, $(I/E)^*$,

$$(I/E)^* = \frac{I_{bit}}{E}U, \tag{5.28}$$

is a useful non-dimensional parameter to compare thruster designs. Both the performance scaling number and the non-dimensional impulse-to-energy ratio will be used in the following section to examine performance scaling trends.

5.3   Measured Performance of GFPPTs

In order to determine if the performance scaling relations developed in the previous section are valid, two GFPPT designs were tested over a wide range of operational conditions. The two thrusters, PT5 and PT9, were developed specifically to observe the performance scaling trends using various mass bit, energy, capacitance, and inductance-per-unit-length values. PT5 was designed with a modular energy storage bank and coaxial electrodes to measure the effects of changing the capacitance and energy while keeping the inductance-per-unit-length constant. PT9 was designed with modular parallel-plate electrodes to measure the effects of changing the inductance-per-unit-length while keeping the capacitance and energy constant. Both designs were tested over an order of magnitude of argon propellant mass bit values.

The performance measurement techniques and the thrusters themselves have been described in Refs. [5, 57]. The performance of PT5 has been described in detail in Ref. [5] and a short summary will be provided in this section. The performance of PT9 with and without sidewalls will also be presented. Finally, the GFPPT characteristic velocity for each thruster design will be evaluated to normalize the performance data.
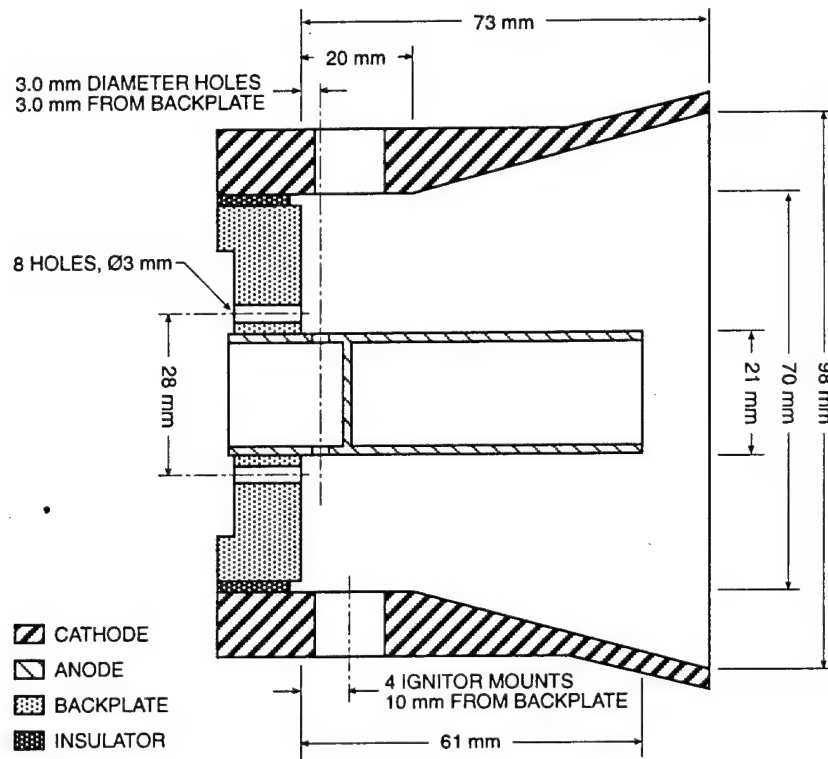
Figure 5.5: Schematic of PT5.

5.3.1 Performance of PT5

The coaxial electrode set of PT5 is shown in Fig. 5.5. PT5 was designed with a modular energy storage device using either a 130 or 270 μF capacitor bank to determine the effects of capacitance and energy on performance. As described in Ref. [5], PT5 showed two modes of operation depending on the mass bit. Figure 5.6 shows impulse bit measurements over a wide range of mass bit, capacitance, and energy levels. The cut-off between Mode I and Mode II operation is near 0.5 μg per pulse and slightly decreases with decreasing capacitance. Mode I operation occurs for mass bit values above the cut-off and is characterized by an impulse bit and an impulse-to-energy ratio that increase with increasing mass bit. This leads to a relatively constant thruster efficiency in this mode of operation. In Mode II operation, the impulse bit and impulse-to-energy ratio are largely independent of the mass bit leading to an efficiency that varies linearly with exhaust velocity as expected by the model developed in the previous section. Possible explanations for Mode I operation are given in the appendix.
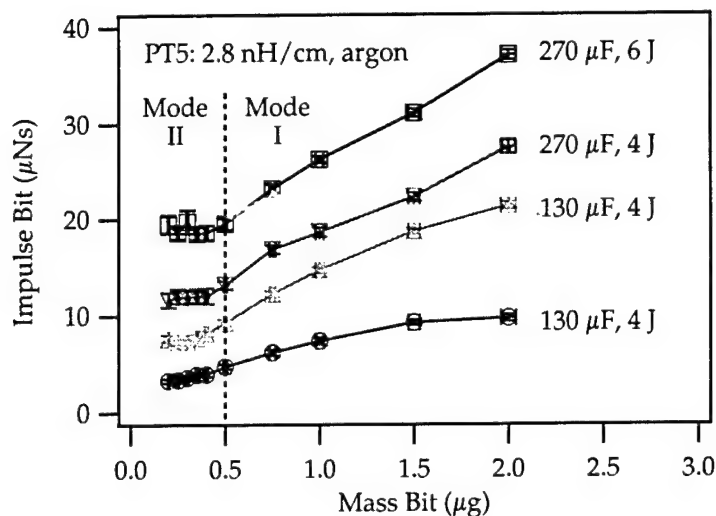
Figure 5.6: Measured impulse bit of PT5 with argon propellant at two capacitance and two energy values. Mode I and Mode II are also separated by the vertical dashed line and described in Section 5.3.1.

5.3.2 Performance of PT9

PT9 uses variable width (1" and 1/2") parallel-plates at two separation distances, (1" and 1/2") to vary the inductance-per-unit-length as shown in Fig. 5.7 and discussed in more detail in Ref. [57]. Three configurations were tested (a,b, and c) to measure the effect of increasing the inductance-per-unit-length while keeping the capacitance and energy constant near 130 μF and 4 J, respectively. The smallest value of inductance-per-unit-length (configuration a) was designed to be similar to the L' value of PT5.

Wall Losses in PT9

In Ref. [57] Pyrex sidewalls where used with PT9 to contain the propellant injected prior to the discharge. Figure 5.8 shows the change in the measured impulse bit from removing the sidewalls. These measurements suggest that two trends are competing depending on the mass bit and molecular weight of the propellant. It appears for both argon and helium that as the mass bit and pressure increase, the sidewalls may actually help to focus the exhaust stream. This is more the case for helium which has a larger thermal velocity for the same plenum temperature. In fact, since the pulse rate was kept constant in tests with both propellants, the propellant utilization efficiency may be much lower with helium, especially without sidewalls. In that case, a significant amount of helium may escape out of the electrode volume and not be accelerated by the discharge. With sidewalls, the performance with helium is better than the

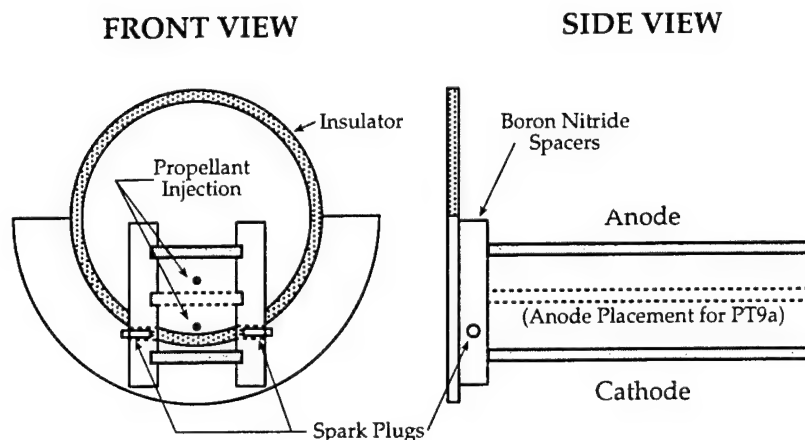**FRONT VIEW**   **SIDE VIEW**

Figure 5.7: Schematic drawing of PT9b with 1" x 1" electrodes as well as the anode placement for PT9a. PT9c uses 1/2" wide electrodes with the same vertical 1" placement as PT9b.

performance with argon by a slightly smaller factor than one would expect for a molecular phenomenon. In that case, the "drag" of ions hitting the side-walls, recombining, and slowing to a thermal velocity determined by the surface temperature (much less than sheet speed) would be expected to scale with the *square root* of the atomic mass ratio, about 3.2. The discrepancy (the performance improvement was measured to be nearly a factor of 2.5) could be caused by the lower propellant utilization expected with helium.

Ion diffusion to the walls has been suspected before as a significant loss mechanism in magnetic shock tubes [79] and plasma guns [80]. In addition, if the current is carried at all by the ions in these discharges, then the cathode surface could also be retarding the bulk motion of the current sheet. Regardless of the physical nature of the "drag", the negative effect of having any extra surface area exposed to the discharge is extremely apparent. For that reason, it was decided that the performance of PT9 was best measured again *without* sidewalls.

Performance of PT9 Without Sidewalls

The performance of PT9 over a wide range of mass bit values and three values of inductance-per-unit-length are shown in Fig. 5.9. In all these measurements, a 130 μF capacitor bank was used to keep the charging time requirements to a minimum with as little propellant escaping beyond the electrode volume as possible. The capacitors were charged up to approximately 250 V for each of six pulses in a burst. The maximum performance level measured with PT9 is with the highest inductance-per-unit-length configuration, 25% at 8,000 s I_{sp} with a 15 % efficiency measured near 5,000 s.
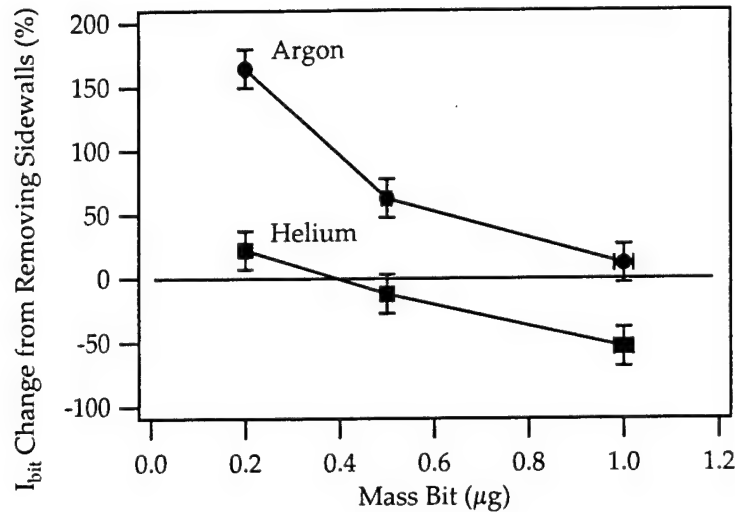
Figure 5.8: The percentage change in the measured impulse bit from removing pyrex sidewalls using both argon and helium propellants with PT9.

Note that there is no transition between two modes of operation expect, perhaps, near 0.5 μg per pulse in the lowest L' value of 2.8 nH/cm. In general, the efficiency varies linearly with the exhaust velocity as predicted by the model described in the previous section. The impulse-to-energy ratio increases close to linearly with increasing inductance-per-unit-length. Both of these trends will be discussed in more detail in the following section.

5.3.3   GFPPT Characteristic Velocity Values

The main design parameters for GFPPT hardware are the capacitance, initial inductance, and inductance-per-unit-length. These three parameters can be condensed into a single one that can effectively be used to predict performance: the GFPPT characteristic velocity, U, defined in Eq. 5.26. This characteristic parameter is derived from easily measurable quantities which are listed in Table 5.1 at the end of this chapter. Note that larger values of U correspond to small capacitance and inductance-per-unit-length values.

5.4   Comparison of Scaling Relations with Measurements

Three scaling trends have been predicted by the model developed in Section 5.2:

1. The impulse bit should scale linearly with the integral of the current squared.
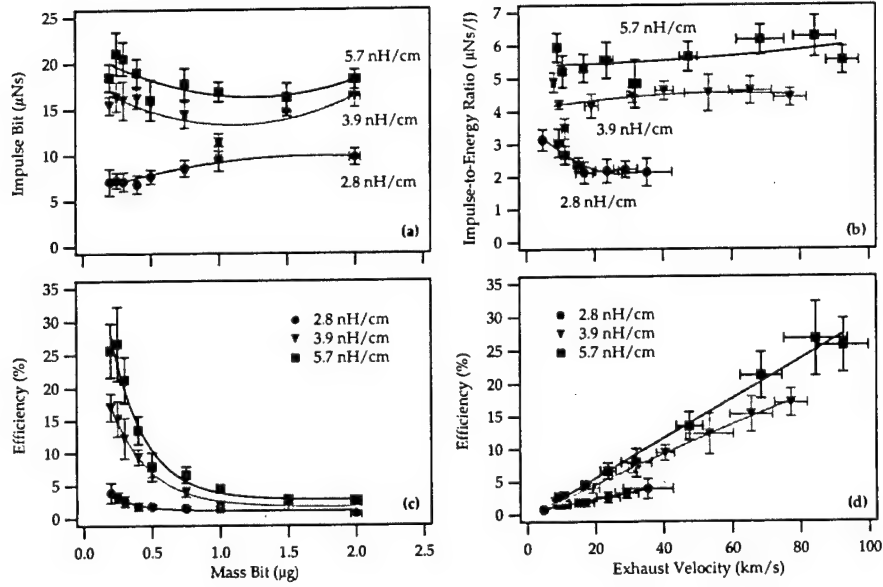
Figure 5.9: Measured performance of PT9 with argon, a 130 μF capacitor bank, approximately 4 J/pulse and the inductance-per-unit-length as a parameter. Graphs (a) and (c) show the impulse bit and thruster efficiency as a function of mass bit. Graphs (b) and (d) show the impulse-to-energy and thruster efficiency as a function of exhaust velocity.

Thruster		Geometry	Cap. (μF)	$L^{'}$ (nH/cm)	Energy (J)	U (km/s)
PT5	(a)	Coaxial	130	~ 2.8	2	190
	(b)	Coaxial	130	~ 2.8	4	190
	(c)	Coaxial	270	~ 2.8	4	130
	(d)	Coaxial	270	~ 2.8	6	130
PT9	(a)	P-Plate	130	2.8	4	190
	(b)	P-Plate	130	3.9	4	135
	(c)	P-Plate	130	5.7	4	92

Table 5.1: Thruster test configurations using argon propellant between 0.2-2.0 μg per pulse. Because PT5 has slightly flared electrodes the inductance-per-unit-length value, $L^{'}$, shown here is the average value. The inductance-per-unit-length values for PT9 are found using a conformal mapping technique of the electrode geometry as described in [57].
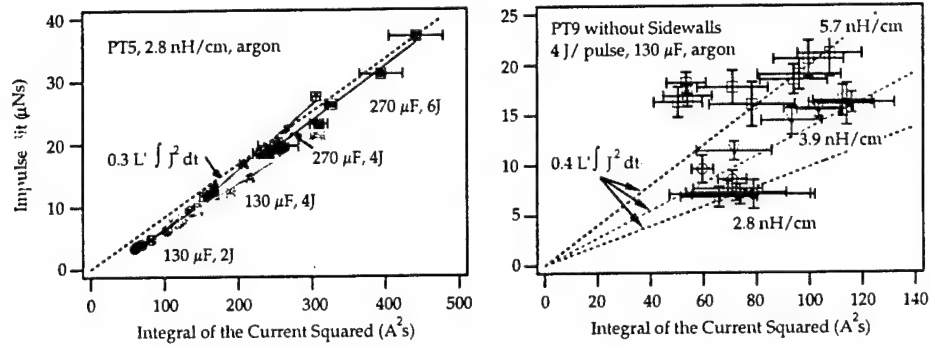
Figure 5.10: Impulse bit as a function of the integral of the current squared for both PT5 (left panel) and PT9 (right panel) over a wide range of operational conditions.

2. The impulse-to-energy ratio should be relatively constant over both mass bit and exhaust velocity.

3. The thruster efficiency should be linearly proportional to the non-dimensional exhaust velocity.

We will now examine these three predictions one at a time.

5.4.1 Impulse Bit Scaling with $\int J^2 dt$

Figure 5.10 shows the measured impulse bit as a function of the integral of $J^2(t)$ for both PT5 and PT9. With the open electrode design of PT9, deriving the current from the voltage waveform was difficult due to EMI effects. Consequently, the errors are large for that measurement as reflected by the error bars in Fig. 5.10. Still, both thrusters show a linear trend as expected. Also note that for PT5 the integral of the current squared and the measured impulse bit both increase by as much as a factor of two for each curve. The integral of J^2 stays relatively fixed for PT9 although the impulse bit increases with increasing inductance-per-unit-length. For PT5, the inductance-per-unit-length does not change and the slope of a line going through the data in each case is very similar as expected.

From Eq. 5.17 the impulse bit should be proportional to $L'/2 \int J^2 dt$. The slopes of the lines that agree with the measurements, however, are slightly smaller than predicted. This could be due to a number of loss mechanisms that are not accounted for by the model. These potential losses include energy going into unrecoverable plasma internal modes, profile losses from canted current sheets, and the conduction of ions to the cathode creating wall losses as described in Section 5.3.2. Again, although proportionally the impulse bit
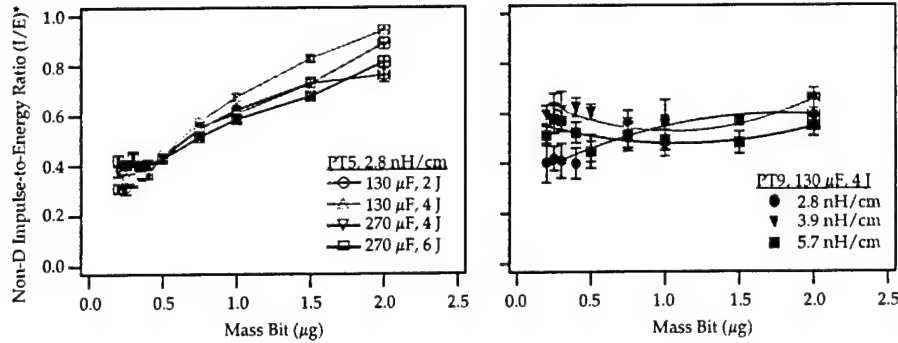
Figure 5.11: Impulse bit and non-dimensional impulse-to-energy ratio as a function of mass bit for both PT5 (left panel) and PT9 (right panel).

values are lower than expected, they do scale linearly with the integral of the current squared.

5.4.2 Energy-to-Impulse Ratio Scaling with Mass Bit

Graphs of the impulse-to-energy ratio as a function of mass bit for each thruster have already been shown in Fig. 5.6 and Fig. 5.9. Normalizing the impulse bit by the discharge energy and the GFPPT characteristic velocity, U, yields the non-dimensional impulse-to-energy ratio, $(I/E)^*$, as defined in Eq. 5.28. Using $(I/E)^*$ causes all the curves with varying capacitance, inductance-per-unit-length, and energy to collapse onto a single curve. In general, the trend of the impulse bit scaling with the energy level, the square root of the capacitance, and the inductance-per-unit-length is present throughout the data from both thrusters. At mass bit values below 0.5 μg, Both thrusters share a similar value of $(I/E)^*$ between 0.4 and 0.6, but PT5 has a larger value than PT9 at higher mass bits in Mode I operation. This trend will be examined in more detail in the appendix, however, for now it is important to notice that although there is an increase in $(I/E)^*$, it is similar for all four curves related to PT5.

For PT9, the three curves of $(I/E)^*$ are more similar at higher mass bits. The 1" x 1", 3.9 nH/cm configuration of PT9b seems to have the highest value at the lower mass bits. This could be due to it having slightly more propellant to accelerate compared to the 1/2" wide case of PT9c where more propellant might have escaped before the discharge was initiated. Compared to the 1/2" gap of PT9a, PT9b has a better electrode surface to volume ratio with a 1" gap, possibly reducing the amount of wall losses. Still, compared to the separated curves of the measured impulse bit in Fig. 5.9, the curves of $(I/E)^*$ in 5.11 are very similar.
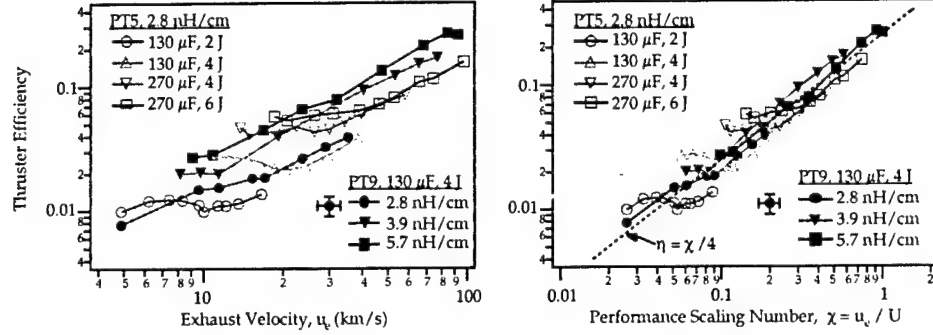
Figure 5.12: Thruster efficiency as a function of exhaust velocity and the performance scaling parameter, $\chi = u_e/U$, with a sample error bar shown near the legends. Using the performance scaling number allows almost all the data to fall close to one line, $\eta_t = \chi/4$.

5.4.3 Efficiency Scaling with χ

Perhaps the most important prediction for the performance scaling of GFPPTs is that the efficiency is expected to scale linearly with the exhaust velocity. This trend was predicted by the model developed in Section 5.2, Eq. 5.24. Except for the Mode I operation (high mass bit, low exhaust velocity) in PT5, this is generally true from measured performance, as shown in Fig. 5.12. These graphs show the combined measurements for all seven configurations of the two GFPPT designs. In the left panel, the curves are spread out depending on capacitance, inductance-per-unit-length, and energy as the thruster efficiency is plotted versus the measured exhaust velocity. In the right panel, the thruster efficiency is plotted versus the performance scaling number, χ. Much of the data can be seen to collapse within 10% of a *single line*, $\eta_t = \chi/4$. This upholds the validity of the scaling model derived in Section 5.2 over a wide range of measured parameters. For the low-energy GFPPTs tested here, the efficiency is almost always related to the performance scaling number.

The linear coefficient of the line fit to the performance data, 1/4, corresponds to a critical resistance ratio of about 2 (see Eq. 5.25) which falls within the bounds of the model applicability. The largest deviations from this linear trend are at high mass bit values in PT5 Mode I operation and some slight deviations in PT9 at higher mass bit values. In the appendix we present four potential explanations for these deviations and argue that the plasma resistance could be decreasing at the higher mass bits. Smaller values of the effective plasma resistance reduce ψ and, hence, are likely to increase η_t.

5.5 Summary and Conclusions

An analytical model was used to derive performance scaling relations for GF-PPTs. A central parameter to these relations is the GFPPT performance scaling number, defined as the ratio of the exhaust velocity to the GFPPT characteristic velocity. The relations were tested with an experimental data base over a range of 70 different operational conditions. The following conclusions can be drawn from this entire study:

- The thrust efficiency is directly proportional to the GFPPT performance scaling number for the conditions tested here,

$$\eta_t \propto \chi = \frac{u_e}{U} = \frac{1}{6}L' \sqrt{\frac{C}{L_0}}\, u_e. \tag{5.29}$$

- For the low-energy GFPPTs studied here, the effective plasma resistance seems to be significant and plays an important role in determining performance.

- Wall losses were found to be important in the parallel-plate geometry and significantly higher performance has been measured without sidewalls.

- All measured performance data (η, u_e, and I_{bit}/E) can be made to collapse onto single, universal curves when non-dimensionalized according to the predicted scaling laws.

Although these scaling laws were tested over a wide range of parameters, it remains interesting to explore their validity at higher discharge energies and with different propellant types. Another remaining question is the explicit relation between the operating conditions and the plasma resistance which impacts the model through the parameter ψ. As research continues and with the use of the scaling relations derived here, GFPPTs have the potential to be useful for many spacecraft.

5.6 APPENDIX: Possible Explanations for Mode I

As seen in almost all the comparisons between measurements and models, the largest discrepancies occur for PT5 in Mode I operation. In this mode, the efficiency does not decrease monotonically with exhaust velocity and the impulse-to-energy ratio increases with increasing mass bit. So far, four different explanations for the higher than predicted performance have been proposed: electrothermal energy recovery, finite electrode length effects, increased profile or sweeping efficiency, or a decrease in the effective plasma resistance at higher mass bit values. The real explanation could be a combination of these ideas which we will now explore one at a time.

5.6.1 Electrothermal Energy Recovery

At the higher mass bit values of Mode I, the number density and pressure are higher and the mean free path is correspondingly lower compared to Mode II operation. If any electrothermal energy is to be recovered at all, it would be at Mode I conditions. The scaling relations suggested for a thruster where electrothermal acceleration is dominant, however, are quite different (see Ref. [54] for example). In this case, the impulse bit is expected to scale with the *square root* of the discharge energy to mass bit ratio and not depend directly on capacitance or inductance change. This is a result of the energy deposited in the plasma being proportional to the integral of RJ^2. The *efficiency* of a pure electrothermal accelerator is expected to be constant over wide range of energy, exhaust velocity, and mass bit values. While the efficiency for PT5 is indeed independent of mass bit and exhaust velocity at high mass bit values (i.e. Mode I), it does show a dependence on energy.

Another contrary piece of information for this explanation is the relation between the impulse bit and integral of the current squared, as shown in Fig. 5.10. For an electrothermal thruster, the exhaust velocity and hence the impulse bit should scale as the square root of the integral of the current squared. Clearly this is not the case with the measured trends having more of a linear character as would be expected from an electromagnetic acceleration. In addition, even at mass bit values that clearly fall into Mode I operation, the impulse-to-energy ratio was found to be *constant* over a wide range of energy values as described in Ref. [5]. This is characteristic of an electromagnetic accelerator, not an electrothermal one. Therefore, although some electrothermal energy may very well be recovered in these discharges, the amount is believed to be minor and not enough to explain Mode I operation.

5.6.2 Finite Electrode Length Effects

In Mode I operation, the discharge may not reach the end of the electrodes by the time the capacitor is fully drained. If there is a uniform propellant distribution before the pulse, then the current sheet would run into a large

amount of unaccelerated propellant after the Lorentz force has stopped. This would impose a serious amount of drag on the sheet, however, the impulse bit would not be affected. With the amount of mass increasing at the same rate as the velocity is decreasing, the impulse bit is constant, however, the efficiency steadily *decreases*. Unfortunately this description is in opposition to the observed trend.

Instead, if there is an exponential propellant distribution, then the efficiency would be highest when the greatest amount of energy in the capacitor is transferred to the discharge. For the smaller mass bits, the current sheet may run to the end of the electrodes well before the capacitor is fully drained, reducing the efficiency. We would expect that as the velocity continues to increase and the electrode length is fixed, the efficiency would decrease as duration the current sheet is in contact with the electrodes decreases. Once again, this explanation does not match exactly with the observed performance trends.

5.6.3 Increased Sweeping and/or Profile Efficiency

Since these quantities have not been measured directly, it is difficult to determine if an increase in one or the other is indeed the cause for the higher than expected performance. In previous studies of current sheet structure in argon discharges, it has been noticed that the sweeping efficiency (the effectiveness of the current sheet to pick up propellant as it moves down the electrodes) increases with increasing current rise rates [1, 40]. An empirical rule of thumb is that 10^{12} A/s-cm over the span of the current sheet is required for 100% sweeping efficiency. Most of the low-energy GFPPT discharges presented here fall *just below* this 10^{12} A/s-cm cut-off. As seen in Fig. 5.10 the current does indeed increase as the mass bit value increases which could imply that the sweeping efficiency is improving. Still, as shown in Section 5.2, the *impulse* should not depend on how the mass was swept up. In other words, although the thrust efficiency should be sensitive to the sweeping efficiency, the impulse-to-energy ratio should not. In addition, both Ref. [40] and Ref. [63] showed that the sweeping efficiency *decreased* for higher mass bit values.

As far as the possibility of a profile efficiency increase in Mode I operation, once again the literature points towards the opposite of the trends we observe with mass bit and pressure. Using an inverse z-pinch device, Johansson found that the tilting of the current sheet (which causes profile losses) *increased* for higher mass bit values [63]. Although the profile efficiency should effect both the thruster efficiency and the impulse-to-energy ratio, the existing models appear to predict the opposite trend. In addition, the GFPPTs presented in this chapter have much shorter electrodes compared to any accelerator where significant tilting and profile losses have been found to occur.

5.6.4 Decrease in Effective Plasma Resistance

Another possibility is based on the potentially changing value of ψ with the mass bit (which is related to the initial propellant density). As apparent in

all the comparisons between predicted and measured performance, as the mass bit increases, the measured performance moves closer and closer to values that are predicted by smaller critical resistance ratios. As the initial inductance and capacitance are fixed, this would imply that the effective resistance in the circuit (capacitor internal impedance plus plasma resistance) is decreasing as the mass bit (and density) is increasing. Once again we turn to Fig. 5.10 to see that the current levels also increase at higher mass bit values. In fact, the mass bit cut-off between a relatively constant integral of J^2 and where the integral values begin to increase agrees well with the transition point found in Fig. 5.6. As expected, and found in previous experiments [79, 31], as both the energy and current increase, the effective plasma resistance drops. A decreasing value of ψ for the observed increasing performance of PT5 in Mode I operation is the most consistent explanation with all the observed trends presented here and in the literature.

Chapter 6

Final Conclusions

This chapter comprises our final conclusions derived from our three-year study. First, we describe the need for the development of GFPPT performance scaling relations and outline the goals of this research work. Next, we summarize our findings, and, finally, suggest future GFPPT design considerations and research topics.

6.1 Determining Experimentally Verified Performance Scaling Relations

To design and optimize a GFPPT for a particular mission or maneuver, its efficiency, exhaust velocity (specific impulse), and impulse-to-energy ratio must be predictable over a wide range of operating conditions. This implies that the influence of the mass bit, discharge voltage, capacitance, energy, initial inductance, and electrode geometry on performance is known with some certainty. The difficulty of developing such performance scaling relations is due to the complex nature of the GFPPT discharge dynamics, the large number of variable parameters that could influence the performance, and the lack of a previously measured performance database that spans over a wide range of operating conditions. To be of any benefit, a set of performance scaling relations must be developed from a model that is based on the fundamental acceleration processes and subsequently verified empirically. Completing this task is the main topic of this dissertation work.

6.2 Research Goals and Activities

The goal of this research is two-fold: 1) to derive useful performance scaling laws for low-energy GFPPTs, and 2) to experimentally verify them with performance measurements over a wide range of operational conditions. In order to derive

a complete set of performance scaling relations, a series of theoretical models have been developed with the following qualities:

1. Consecutive models were developed with increasing complexity so that the results of the most intricate model can be understood in terms of the more elementary relations.

2. The dynamics of the discharge have been modeled in detail while the more complex plasma physics including the conductivity, radiation, and internal mode losses have been condensed into a single effective resistance term.

3. The number of free parameters has been reduced to a minimum by a non-dimensional approach to the problem.

4. The non-dimensional model has been explored over a wide range of input parameters to identify global scaling trends.

To test the validity of the models, the performance of two specially designed GFPPTs has been measured in carefully controlled experiments. The performance measurements and GFPPTs have been designed so that:

1. Contamination from background gases in the vacuum facility does not affect the measured performance of the GFPPTs.

2. The discharge initiation is symmetric and nearly uniform for each test.

3. PT5 and PT9 test the effects of changing capacitance and inductance-per-unit-length, respectively.

4. Each time a single operational condition (C, L', m_{bit}, V_0, etc.) is changed, the others remain fixed so that the experiment is controlled.

5. The performance of each operational condition is measured at least twenty times to insure accuracy.

The results from the models and the performance measurements will now be summarized in the next section.

6.3   Summary of Findings

In this section we summarize the results of this dissertation work by dividing them into three categories: 1) predictions from models, 2) performance measurements from PT5 and PT9, and 3) a comparison of the models and the measurements.

6.3.1 Derivation of Scaling Relations

Three models with increasing complexity were developed to provide performance scaling relations. The first model used an effective circuit relation with fixed elements to show that the highest energy transfer efficiency comes from using a nearly-critically damped current waveform. This was explored further in the second model where the inductance and mass were allowed to vary in a prescribed manner throughout the pulse with $0.3 \leq \psi \leq 3$. The results from the second analytical model are as follows:

- The efficiency is expected to scale linearly with the exhaust velocity and the GFPPT characteristic velocity, $\mathcal{U}$,

$$\eta_t = \frac{\bar{u}_e}{\mathcal{U}} e^{-\sqrt{\psi}}, \tag{6.1}$$

where,

$$\mathcal{U} \equiv \frac{3}{L'} \sqrt{\frac{L_0}{C}}, \qquad \psi \equiv \frac{R}{2} \sqrt{\frac{C}{L_0}}. \tag{6.2}$$

- The exhaust velocity is expected to scale with a set of parameters that depends on the mass distribution. These parameters are also found in the non-dimensional model as the dynamic impedance parameter, α. For a slug mass distribution, the expected scaling is,

$$\bar{u}_e = \frac{2}{\mathcal{U}} \frac{E}{m_{bit}} e^{-\sqrt{\psi}} = 2\mathcal{U}\alpha_{slug} \, e^{-\sqrt{\psi}}, \tag{6.3}$$

and for a uniform mass distribution, the expected scaling is,

$$\bar{u}_e = \sqrt{\frac{4EL'}{3m'L_0}} \, e^{-\sqrt{\psi}} = 2\mathcal{U}\sqrt{\frac{\alpha}{3}} \, e^{-\sqrt{\psi}}, \tag{6.4}$$

where,

$$\alpha_{slug} \equiv \frac{L'^2 V_0^2 C^2}{18L_0 m_{bit}}, \qquad \alpha \equiv \frac{L'^3 V_0^2 C^2}{18L_0^2 m'}. \tag{6.5}$$

The third model used a non-dimensional approach to reduce the number of free parameters by half. Furthermore, as compared to the previous model, no assumptions where made about the current waveform type or the inductance profile, an exponential mass distribution was used to simulate the conditions more accurately, and the electrodes were allowed to have a flared geometry. The consequent set of coupled, non-linear differential equations was solved numerically and yielded the following results (taken from Section **??**):

- Small values of ψ have the highest values of efficiency and the non-dimensional impulse-to-energy ratio, $(I/E)^*$.

- As in the variable element model, for $\alpha < 10$, the efficiency is linearly *proportional* to the non-dimensional exhaust velocity, $(\bar{u}_e)^* = 3\bar{u}_e/\mathcal{U}$, which is not a strong function of ψ or the electrode length.

- For $\psi < 0.3$, there is an optimum efficiency between $1 \leq \alpha \leq 10$.

- Using a finite electrode length changes the exact value of the efficiency, but the scaling relations are generally intact.

- Using a flared outer electrode has mixed, and only slight benefits, depending on α.

6.3.2 Performance Measurements

The performance of PT5 with variable capacitance and PT9 with variable inductance-per-unit-length was measured over a wide range of argon mass bits. For PT5, four cases with different capacitance and energy per pulse were examined: a) 130 μF, 2 J, b) 130 μF, 4 J, c) 270 μF, 4 J, and d) 270 μF, 6 J. The inductance-per-unit-length, L', for PT5 was kept constant at 2.8 nH/cm. For PT9, three cases with different values of L' were evaluated: a) 2.8 nH/cm, b) 3.9 nH/cm, and c) 5.7 nH/cm. The capacitance and energy per pulse for PT9 were fixed at 130 μF and 4 J. In all seven cases, 10 mass bit values between $0.2 - 2.0 \mu$g were used to span over a large range of exhaust velocity values.

For PT5, two modes of operation were identified. Mode II operation occurs at the lowest values of mass bit and highest values of exhaust velocity. In this mode, the efficiency scaled linearly with exhaust velocity, as expected. Mode I operation occurs at the highest values of mass bit and the lowest values of exhaust velocity. In this mode, the efficiency remained *constant* with exhaust velocity, providing *better* than expected performance. The increase in performance is suspected to be caused by a decrease in the effective plasma resistance, and consequently a smaller ψ value. The transition point between the modes is determined by the current level in the discharge. In Mode II, the current level remained relatively fixed and was determined solely by the energy per pulse. In Mode I, the current increased with increasing mass bit. In both modes, the performance increased with the square-root of capacitance, and the impulse-to-energy ratio remained nearly constant over different energy levels.

For PT9, a large increase in performance was observed when the insulating sidewalls were removed. With the sidewalls in place, the performance did not depend on the inductance-per-unit-length. Without the sidewalls, the performance scaled linearly with the inductance-per-unit-length as expected. The two modes of operation that occurred in PT5 were not observed in PT9. PT9c, which had 1/2" wide electrodes separated by a 1" gap and an $L' = 5.7$ nH/cm, had the best performance with an efficiency of 25% at an exhaust velocity of 85 km/s (8700 s I_{sp}) and an impulse-to-energy ratio of 6 μNs/J.

6.3.3 Comparison of Measurements and Models

The following trends were noticed when the performance measurements were compared to the theoretical models:
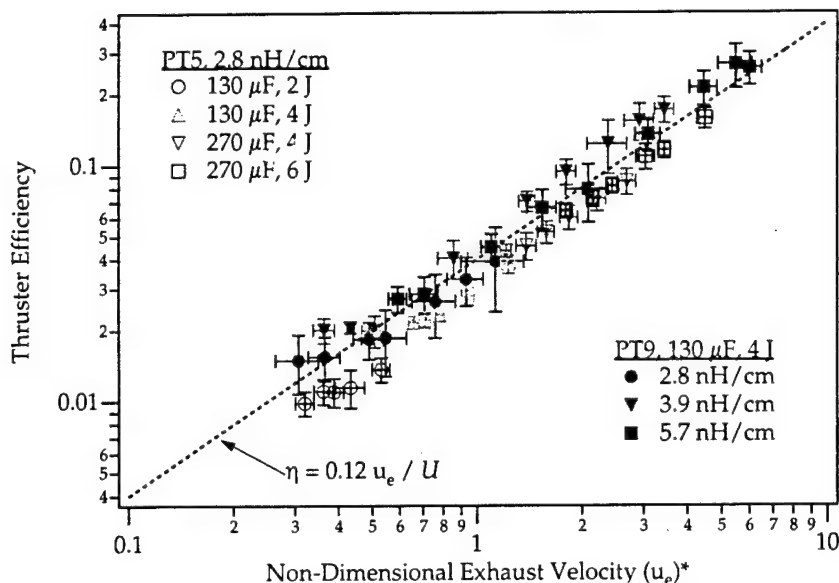
Figure 6.1: Plot of measured thruster efficiency versus measured non-dimensional exhaust velocity for both PT5 (Mode II operation only) and PT9. Almost all the data points fall within the error bars of a linear relationship, $\eta = 0.12\bar{u}_e/\mathcal{U}$.

1. The thruster efficiency is indeed proportional to the exhaust velocity and the PPT characteristic velocity for both PT9 and PT5 in Mode II operation (See Fig. (6.1)).

2. The thruster efficiency also increases gradually with α. The measured performance trends for PT9 and PT5 in Mode II operation match the predicted trends for $2 \leq \psi \leq 4$ (See Fig. (6.2)).

3. The exhaust velocity is proportional to the dynamic impedance parameter, α^n, where $0.5 \leq n \leq 1$, depending on the mass distribution prior to the discharge and the dynamic efficiency.

4. The non-dimensional impulse-to-energy ratio, $(I/E)^*$, is relatively constant (near 0.1) for α values of practical interest (between 1-10) and for a fixed value of the critical resistance ratio, ψ.

5. For the low-energy SRL-EPPDyL GFPPTs studied here, the effective plasma resistance plays an important role in determining performance. Values of $\psi \approx 2 - 4$ provide predictions from the non-dimensional model that match measured performance trends within a factor of two.
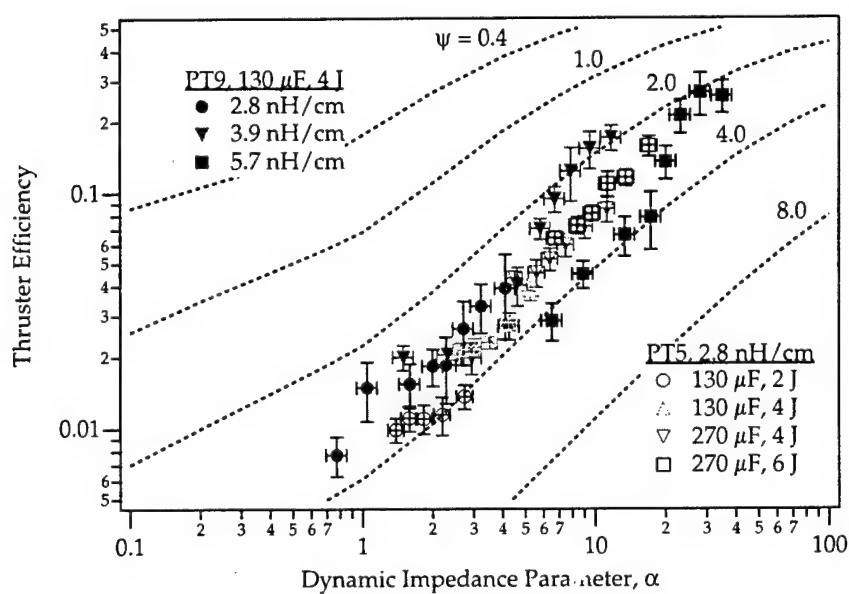
Figure 6.2: Plot of measured thruster efficiency versus measured dynamic impedance parameter for both PT5 (Mode II operation only) and PT9. Almost all the data points fall within the error bars of $2 \leq \psi \leq 4$.

Although there is generally good agreement between the models and the performance measurements over certain ranges of operation, the critical resistance ratio, ψ, remains difficult to determine from a measurement of the internal impedance of the capacitor bank alone. As discussed further in the last section of this chapter on the future directions of GFPPT research, understanding the effective resistance of the plasma is paramount to determining and reducing ψ which should improve performance.

6.4 The Next Generation GFPPT Design

The performance scaling relations found in this dissertation suggest that a GFPPT should be designed with the largest inductance-per-unit-length and capacitance possible. Both of these parameters, however, cannot extend beyond some reasonable limits whereby other effects such as a reduced propellant utilization efficiency, profile losses, or increased power conditioner mass, for example, start to have a greater influence. We will now examine the maximum limits of the inductance-per-unit-length and capacitance in the next two sections.

6.4.1 Parallel-Plate vs. Coaxial Electrodes

As shown in Fig. (??), for coaxial electrodes to have a value of $L^{'}$ equal to that of a parallel-plate electrode set, its inner-to-outer radius ratio must be approximately ten times larger than the corresponding height-to-width ratio. For example, to have $L^{'} = 5.7$ nH/cm, as in the PT9c configuration, a coaxial electrode set would have to have a radius ratio of 18. Unless the inner electrode is very slim, the outer electrode, in many cases, would have to be quite large and possibly massive. The radius of the inner electrode also has a lower limit due to the probability that large current densities can cause significant erosion. Initiating the discharge uniformly with a large outer electrode could also be a problem. Finally, because the Lorentz force is proportional to $1/r^2$ in a coaxial thruster, a slim inner electrode could cause a significant non-uniform acceleration that would tilt the current sheet. Although other effects such as canting (see Ref. [52]) can also influence the current sheet profile, a slim inner electrode could lead to large profile losses.

A coaxial set of electrodes has the advantage that all the propellant injected before the discharge is contained. This is not the case, however, for a parallel-plate set of electrodes. As the height-to-width ratio increases, more and more of the propellant escapes the discharge volume before the pulse. Although side-walls can contain the propellant, they have been shown to significantly reduce the performance. If the electrodes are made wide enough to capture all the propellant, the distance between them could make uniform discharge initiation difficult. Furthermore, the profile of the current sheet in parallel-plate thrusters has been shown, in many cases, to be non-planar. The cause of the canting is currently under investigation, but the impact on performance is obviously detrimental. Finally, the open nature of the parallel-plate design allows the

plasma to escape outside the intended discharge volume. Extreme care must be taken to insulate nearby electrically conducting surfaces to prevent the arc from attaching to undesirable locations.

For many of the reasons mentioned above, we believe that a *coaxial* set of electrodes could be the most desirable from a system point of view. First, coaxial electrodes contain the discharge and magnetic fields, and, although a uniform initiation may be difficult to accomplish, it is not impossible. Second, the profile losses from a non-uniform Lorentz force may be combated by the canting effects that have been noticed in GFPPTs. If the inner electrode is designed to be the cathode, it could be made quite slim (to the limit where current density and erosion are still tolerable) with the overall profile losses not being as important as the performance gain from a higher inductance-per-unit-length. Obviously, more experiments testing various inner electrode radii in coaxial electrodes need to be conducted. In any case, we believe this is the direction for future GFPPT designs.

6.4.2   The Optimal Value of Capacitance

Besides the performance scaling, the value of capacitance mainly effects the mass of the thruster and power conditioning hardware. This is because larger capacitance values lead to larger charging currents unless the charging time is increased. Such larger values of charging current require a more massive power processing modulator. Conversely, longer charging times allow more propellant to potentially escape the discharge volume before the pulse, thus reducing the propellant utilization efficiency. For this reason, larger values of capacitance dictate longer (and potentially wider electrodes for parallel-plate thrusters), more massive electrodes. Although the axial extent of the propellant column before the discharge also depends on the molecular weight and the plenum temperature, long electrodes may also be required because the duration of the discharge increases with increasing capacitance. Finally, the capacitance level also effects the critical resistance ratio. Depending of the effective plasma resistance, the capacitance level should not be increased beyond the point where ψ becomes much greater than unity.

The relationship between the capacitance and the mass of the power processing hardware needs to be investigated further before the optimal capacitance level can be determined explicitly. Still, the benefit of a higher capacitance has been shown both theoretically and experimentally. With that in mind, the highest capacitance value should be used while keeping the propellant utilization efficiency as close to 100% as possible. For the GFPPTs studied in this dissertation with argon propellant, the maximum capacitance is close to 270 μF.

6.4.3 Additional Design Guidelines

In Section **??**, we found that the optimal exhaust velocity is often close in value to the PEP velocity, $\tilde{V}$, a solely technology dependent parameter,

$$\bar{u}_{eopt} \quad \approx \quad \tilde{V} = \sqrt{\frac{2\eta_t N_{ptot}}{\alpha_e}} \propto \sqrt{\frac{2N_{ptot}\bar{u}_e}{\alpha_e \mathcal{U}}}, \tag{6.6}$$

$$\bar{u}_{eopt} \quad \propto \quad \frac{N_{ptot}}{\alpha_e} L' \sqrt{\frac{C}{L_0}}. \tag{6.7}$$

This final relationship should be expected since the payload mass fraction increases with greater performance if the efficiency is linearly proportional to the exhaust velocity. In other words, a larger optimal exhaust velocity leads to more payload mass. For typical values of N_{ptot}, α_e, etc., the optimal exhaust velocity is between 10 and 100 km/s.

It is interesting to note that the lifetime of the device and the specific mass of the capacitors play as important of a role as the GFPPT Characteristic Velocity, $\mathcal{U}$, in determining the optimal mass of the propulsion device. This, along with other trends found in the data, suggest other important guidelines for designing GFPPTs:

- Any change in a GFPPT design which results in higher performance should also be judged on its effect on the lifetime of the thruster.

- The fixed masses: electrodes, packaging, etc. should be kept as small as possible, especially for high exhaust velocity values where the propellant mass will be a small fraction of the spacecraft.

- Care must be taken to minimize the surface area of the insulators and electrodes that is exposed to the discharge for the smallest wall losses.

- Discharge initiation plays a critical role in determining the performance and lifetime of these devices. New low-mass discharge initiation schemes that provide a reliable, uniform, and symmetric breakdown need to be investigated for future use by GFPPTs.

6.5 Future Directions in GFPPT Research

Perhaps the largest remaining question to be answered about GFPPT performance scaling is how the thruster performs at higher energy levels and with different propellant types. The effect of these parameters on the value of the critical resistance ratio, ψ, and the corresponding values of the performance will be important to study in future work on GFPPTs. In general, understanding how the effective plasma resistance and ψ scale with mass bit, energy, current level, and geometry is important, and will involve detailed studies of the plasma physics involved in the discharge.

Two other important research areas involving GFPPTs are currently being studied at EPPDyL. They include investigating the scaling of the profile and

sweeping efficiencies in parallel-plate thrusters using various propellants [52], and investigating a new photoelectrically-assisted discharge initiation scheme that could provide a more uniform, symmetric breakdown with less erosion.

Chapter 7

Administrative Matters

7.1 PI Annual Data

Not included in the electronic version. Submitted on hardcopy.

7.2   Technology Transfer Data Sheet

Not included in the electronic version. Submitted on hardcopy.

Bibliography

[1] R.G. Jahn. *Physics of Electric Propulsion*. McGraw-Hill, 1969.

[2] S. Domitz, H.G. Kosmahl, P. Ramins, and N.J. Stevens. Survey of electromagnetic accelerators. Technical Report TN D-3332, NASA, 1965.

[3] O.K. Mawardi, editor. *Proceedings of an International Symposium on Plasma Guns, Physics of Fluids Supplement (Part II, Vol. 7(11))*, November 1964.

[4] W.J. Guman and W. Truglio. Surface effects in a pulsed plasma accelerator. *AIAA Journal*, 2(7):1342–1343, July 1964.

[5] J.K. Ziemer, E.Y. Choueiri, and D. Birx. Is the gas-fed PPT an electromagnetic accelerator? an investigation using measured performance. In 35th *Joint Propulsion Conference*, Los Angeles, California, June 20-24 1999. AIAA 99-2289.

[6] J. Marshal. Performance of a hydromagnetic plasma gun. *The Physics of Fluids*, 3(1):134–135, January-February 1960.

[7] L.C. Burkhardt and R.H. Lovberg. Current sheet in a coaxial plasma gun. *The Physics of Fluids*, 5(3):341–347, March 1962.

[8] T.J. Gooding, B.R. Hayworth, and R.H. Lovberg. Instabilities in a coaxial plasma gun. *AIAA Journal*, 1(6):1289–1292, June 1963.

[9] R.H. Lovberg. Inference of plasma parameters from measurement of E and B fields in a coaxial accelerator. In *Proceedings of an International Symposium on Plasma Guns, Physics of Fluids Supplement (Part II, Vol. 7(11))*, pages S57–S61, November 1964.

[10] J.K. Ziemer, T.E. Markusic, E.Y. Choueiri, and D. Birx. Effects of ignition on discharge symmetry in gas-fed pulsed plasma thrusters. In 34th *Joint Propulsion Conference*, Cleveland, Ohio, July 13-15 1998. AIAA 98-3803.

[11] A.V. Larson, T.J. Gooding, B.R. Hayworth, and D.E.T.F. Ashby. An energy inventory in a coaxial plasma accelerator driven by a pulse line energy source. *AIAA Journal*, 3(5):977–979, May 1965.

[12] D.E.T.F. Ashby, T.J. Gooding, B.R. Hayworth, and A.V. Larson. Exhaust measurements on the plasma from a pulsed coaxial gun. *AIAA Journal*, 3(6):1140–1142, June 1965.

[13] D.E.T.F. Ashby. Energy loss in pulsed coaxial plasma guns. *AIAA Journal*, 3(6):1045–1047, June 1965.

[14] R.H. Lovberg. The measurement of plasma density in a rail accelerator by means of schlieren photography. *IEEE Transactions on Nuclear Science*, pages 187–198, January 1964.

[15] R.H. Lovberg. Schlieren photography of a coaxial accelerator discharge. *The Physics of Fluids*, 8(1):177–185, January 1965.

[16] R.H. Lovberg. Investigation of current-sheet microstructure. *AIAA Journal*, 4(7):1215–1222, July 1966.

[17] A.V. Larson, L. Liebing, and R. Dethlefsen. Experimental and evaluation studies of a coaxial plasma gun accelerator. Technical Report CR-54710, NASA, 1966.

[18] D.E.T.F. Ashby, L. Liebing, A.V. Larson, and T.J. Gooding. Quasi-steady-state pulsed plasma thrusters. *AIAA Journal*, 4(5):831–835, May 1966.

[19] P. Gloersen, B. Gorowitz, and J.H. Rowe. Some characteristics of a two-stage repetitively fired coaxial gun. *IEEE Transactions on Nuclear Science*, pages 249–265, January 1964.

[20] P. Gloersen, B. Gorowitz, and J.T. Kenney. Energy efficiency trends in a coaxial gun plasma engine system. *AIAA Journal*, 4(3):436–441, March 1966.

[21] B. Gorowitz, T.W. Karras, and P. Gloersen. Performance of an electrically triggered repetitively pulsed coaxial plasma engine. *AIAA Journal*, 4(6):1027–1031, June 1966.

[22] T.W. Karras, B. Gorowitz, and P. Gloersen. Neutral mass density measurements in a repetitively pulsed coaxial plasma accelerator. *AIAA Journal*, 4(8):1366–1370, August 1966.

[23] B. Gorowitz, P. Gloersen, and T.W. Karras. Steady state operation of a two-stage pulsed coaxial plasma engine. In 5th *Electric Propulsion Conference*, San Diego, California, March 7-9 1966. AIAA 66-240.

[24] B. Gorowitz, P. Gloersen, and T.W. Karras. A 20 kW solar powered pulsed plasma engine system concept. In 3rd *Aerospace Sciences Meeting*, New York, New York, January 24-26 1966. AIAA 66-114.

[25] P. Gloersen. Current status of pulsed plasma engine development. In 2nd *Joint Propulsion Conference*, Colorado Springs, Colorado, June 13-17 1966. AIAA 66-566.

[26] T.W. Karras and P. Gloersen. Consequences of the functional dependence of performance on various factors in a systems weight analysis of a pulsed plasma transfer. In 8th *Aerospace Sciences Meeting*, New York, New York, January 19-21 1970. AIAA 70-168.

[27] T.W. Karras, B. Gorowitz, and P. Gloersen. Experimentally measured velocity distribution in the plasma stream of a pulsed coaxial accelerator. *AIAA Journal*, 4(8):1366–1370, August 1966.

[28] P.J. Hart. Plasma acceleration with coaxial electrodes. *The Physics of Fluids*, 5(1):38–47, January 1962.

[29] P.J. Hart. Modified snowplow model for coaxial plasma accelerators. *Journal of Applied Physics*, 35(12):3425–3431, December 1964.

[30] P.M. Mostov, J.L. Neuringer, and D.S. Rigney. Electromagnetic acceleration of a plasma slug. *The Physics of Fluids*, 4(9):1097–1104, September 1961.

[31] L. Aronowitz and D.P. Duclos. Characteristics of the pinch discharge in a pulsed plasma accelerator. In E. Stuhlinger, editor, *Electric Propulsion Development*, volume 9 of *Progress in Astronautics and Rocketry*. Academic Press, 1963.

[32] D.P. Duclos, L. Aronowitz, F.P. Fessenden, and P.B. Carstensen. Diagnostic studies of a pinch plasma accelerator. *AIAA Journal*, 1(11):2505–2513, November 1963.

[33] L. Aronowitz. Delays in initiation of discharges in pulsed plasma accelerators. *AIAA Journal*, 2(11):2019–2020, November 1964.

[34] W.J. Guman. Switch-triggered pulsed plasma accelerator thrust measurements. *AIAA Journal*, 3(6):1158–1159, June 1965.

[35] C.J. Michels and P. Ramins. Performance of coaxial plasma gun with various propellants. In *Proceedings of an International Symposium on Plasma Guns, Physics of Fluids Supplement (Part II, Vol. 7(11))*, pages S71–S74, November 1964.

[36] C.J. Michels, J.E. Heighway, and A.E. Johansen. Analytical and experimental performance of capacitor powered coaxial plasma guns. *AIAA Journal*, 4(5):823–830, May 1966.

[37] D.J. Vargo. Electromagnetic acceleration of a variable-mass plasma. Technical Report TN D-2164, NASA, 1964.

[38] C.J. Michels. Some transient electrical characteristics of the exhaust of a self-crowbarred coaxial plasma gun. Technical Report TN D-2571, NASA, 1964.

[39] R.G. Jahn and W. von Jaskowsky. Structure of a large-radius pinch discharge. *AIAA Journal*, 1(8):1809–1814, August 1963.

[40] R.G. Jahn and W. von Jaskowsky. Current distributions in large-radius pinch discharges. *AIAA Journal*, 2(10):1749–1753, October 1964.

[41] M. Rosenbluth. Infinite conductivity theory of the pinch. Technical Report LA-1850, Los Alamos, 1954.

[42] N.A. Black and R.G. Jahn. Dynamic efficiency of pulsed plasma accelerators. *AIAA Journal*, 3(6):1209–1210, June 1965.

[43] R.G. Jahn, W. von Jaskowsky, and R.L. Burton. Ejection of a pinched plasma from an axial orifice. *AIAA Journal*, 3(10):1862–1866, October 1965.

[44] J.K. Ziemer, E.Y. Choueiri, and D. Birx. Trends in performance improvements of a gas-fed pulsed plasma thruster. In 25th *International Electric Propulsion Conference*, Cleveland, Ohio, August 24-28 1997. IEPC 97-040.

[45] J.K. Ziemer and E.Y. Choueiri. Dimensionless performance model for gas-fed pulsed plasma thrusters. In 34th *Joint Propulsion Conference*, Cleveland, Ohio, July 13-15 1998. AIAA 98-3661.

[46] R.L. Burton. *Structure of the Current Sheet in a Pinch Discharge*. PhD thesis, Princeton University, 1966.

[47] W.R. Ellis. *An Investigation of Current Sheet Structure in a Cylindrical Z-pinch*. PhD thesis, Princeton University, 1967.

[48] T.M. York. *Pressure Distribution in the Current Sheet Structure of a Dynamic Pinch Discharge*. PhD thesis, Princeton University, 1968.

[49] R.L. Burton and R.G. Jahn. Acceleration of a plasma by a propagating current sheet. *The Physics of Fluids*, 11(6):1231–1237, June 1968.

[50] W.R. Ellis and R.G. Jahn. Ion density and current distributions in a propagating current sheet, determined by microwave reflection technique. *Journal of Plasma Physics*, 3(2):189–213, February 1969.

[51] T.M. York and R.G. Jahn. Pressure distribution in the structure of a propagating current sheet. *The Physics of Fluids*, 13(5):1303–1309, May 1970.

[52] T.E. Markusic and E.Y. Choueiri. Visualization of current sheet canting in a pulsed plasma accelerator. In 26th *International Electric Propulsion Conference*, Kitakyushu, JAPAN, October 17-21 1999. IEPC 99-206.

[53] J.K. Ziemer, E.A. Cubbin, E.Y. Choueiri, and D. Birx. Performance characterization of a high efficiency gas-fed pulsed plasma thruster. In 33rd *Joint Propulsion Conference*, Seattle, Washington, July 6-9 1997. AIAA 97-2925.

[54] W.J. Guman. Solid propellant pulsed plasma micro-thruster studies. In 6th *Aerospace Sciences Meeting*, New York, New York, January 22-24 1968. AIAA 68-85.

[55] J.K. Ziemer and E.Y. Choueiri. Performance and erosion measurements of gas-fed pulsed plasma thrusters at NASA jet propulsion laboratory. Technical Report EPPDyL-JPL99a, Princeton University, March 1999.

[56] J. Blandino, D. Birx, J.K. Ziemer, and E.Y. Choueiri. Performance and erosion measurements of the pt8 gas-fed pulsed plasma thruster. Technical Report EPPDyL-JPL99b, NASA Jet Propulsion Laboratory, August 1999.

[57] J.K. Ziemer, E.Y. Choueiri, and D. Birx. Comparing the performance of co-axial and parallel-plate gas-fed PPTs. In 26th *International Electric Propulsion Conference*, Kitakyushu, JAPAN, October 17-21 1999. IEPC 99-209.

[58] J.C. Keck. Current distribution in a magnetic annular shock tube. *The Physics of Fluids*, 5:630–632, 1962.

[59] F.J. Fishman and H. Petschek. Flow model for large radius-ratio magnetic annular shock-tube operation. *The Physics of Fluids*, 5:632–633, 1962.

[60] L. Liebing. Motion and structure of a plasma produced in a rail spark gap. *The Physics of Fluids*, 6:1035–1036, 1963.

[61] J.R. MacLelland, A.S.V. MacKenzie, and J. Irving. Schlieren photography of rail-tube plasmas. *The Physics of Fluids*, 9:1613–1615, 1966.

[62] W.H. Bostick. Hall currents and vortices in the coaxial plasma accelerator. *The Physics of Fluids*, 6(11):1598–1603, November 1963.

[63] R.B. Johansson. Current sheet tilt in a radial magnetic shock tube. *The Physics of Fluids*, 8(5):866–871, May 1965.

[64] M. Andrenucci, M. Caprili, and R. Lazzeretti. Theoretical performance of pulsed coaxial plasma guns. Technical report, Universita di Pisa, 1972.

[65] D. Keefer and R. Rhodes. Electromagnetic acceleration in pulsed plasma thrusters. In 25th *International Electric Propulsion Conference*, Cleveland, Ohio, August 24-28 1997. IEPC 97-035.

[66] R.M. Patrick. High-speed shock waves in a magnetic annular shock tube. *The Physics of Fluids*, 2(6):589–598, November-December 1959.

[67] N.H. Kemp and H.E. Petschek. Theory of the flow in the magnetic annular shock tube. *The Physics of Fluids*, 2(6):599–608, November-December 1959.

[68] P.G. Mikellides, P.J. Turchi, et al. Theoretical studies of a pulsed plasma microthruster. In 25th *International Electric Propulsion Conference*, Cleveland, Ohio, August 24-28 1997. IEPC 97-037.

[69] M.E. Brady and G. Aston. Pulsed plasma thruster ignitor plug ignition characteristics. *Journal of Spacecraft and Rockets*, 20(5):450–451, 1983.

[70] E.A. Cubbin, J.K. Ziemer, E.Y. Choueiri, and R.G. Jahn. Laser interferometric measurements of impulsive thrust. *Review of Scientific Instruments*, 68(6):2339–2346, 1997.

[71] T.W. Haag. PPT thrust stand. In 31st *Joint Propulsion Conference*, San Diego, California, July 1995. AIAA 95-2917.

[72] E. Antonsen, R.L. Burton, and F. Rysanek. Energy measurements in a co-axial electromagnetic pulsed plasma thruster. In 35th *Joint Propulsion Conference*, Los Angeles, California, June 20-24 1999. AIAA 99-2292.

[73] I. Kohlberg and W.O. Coburn. A solution for three dimensional rail gun current distribution and electromagnetic fields of a rail launcher. *IEEE Transactions on Magnetics*, 31(1):628–633, 1995.

[74] M.S. Di Capua. *Energy Deposition in Parallel-Plate Plasma Accelerators*. PhD thesis, Princeton University, 1971.

[75] J.S. Cory. *Mass, Momentum and Energy Flow from an MPD Accelerator*. PhD thesis, Princeton University, 1971.

[76] H. Takegahara, T. Ohtsuka, and I. Kimura. Effect of applied magnetic fields on a solid-propellant pulsed plasma thruster. In *International Electric Propulsion Conference*, Tokyo, Japan, 1984. IEPC 84-50.

[77] W.A. Hoskins. Asymmetric discharge patterns in the MPD thruster. Master's thesis, Princeton University, 1990.

[78] J.J. Blandino and R.J. Cassady. Propulsion requirements and options for the new millennium interferometer (DS-3) mission. In 34th *Joint Propulsion Conference*, Cleveland, OH, July 13-15 1998. AIAA 98-3331.

[79] J. Keck. Current speed in a magnetic annular shock tube. In *Proceedings of an International Symposium on Plasma Guns, Physics of Fluids Supplement (Part II, Vol. 7(11))*, pages S16–S27, November 1964.

[80] k. Thom, J. Norwood, and N. Jalufka. Velocity limitation of a coaxial plasma gun. In *Proceedings of an International Symposium on Plasma Guns, Physics of Fluids Supplement (Part II, Vol. 7(11))*, pages S67–S70, November 1964.